



## City Research Online

### City, University of London Institutional Repository

---

**Citation:** Yiannakas, M. C. (2004). Magnetic Resonance Imaging (MRI) and its value in the investigation of trabecular bone. (Unpublished Doctoral thesis, City, University of London)

This is the accepted version of the paper.

This version of the publication may differ from the final published version.

---

**Permanent repository link:** <https://openaccess.city.ac.uk/id/eprint/30971/>

**Link to published version:**

**Copyright:** City Research Online aims to make research outputs of City, University of London available to a wider audience. Copyright and Moral Rights remain with the author(s) and/or copyright holders. URLs from City Research Online may be freely distributed and linked to.

**Reuse:** Copies of full items can be used for personal research or study, educational, or not-for-profit purposes without prior permission or charge. Provided that the authors, title and full bibliographic details are credited, a hyperlink and/or URL is given for the original metadata page and the content is not changed in any way.

City University  
London

**Magnetic Resonance Imaging (MRI) and its Value  
in the Investigation of Trabecular Bone**

By:  
Marios C. Yiannakas

**PhD Thesis**

**Submitted for Doctor of Philosophy Degree**

June 2004

Department of Radiography Rutland Place Charterhouse Square London EC1M 6PA

---

## Table of Contents

<b>List of figures.....</b>	<b>V</b>
<b>List of Tables .....</b>	<b>VIII</b>
<b>Acknowledgements.....</b>	<b>IX</b>
<b>Abstract.....</b>	<b>XI</b>
<b><u>Chapter 1: "Introduction"</u> .....</b>	<b>1</b>
<b>1.1 Structure and function of bone tissue .....</b>	<b>2</b>
1.1.1 Bone cells.....	3
1.1.2 Compact bone .....	3
1.1.3 Trabecular bone .....	5
1.1.4 Bone Marrow .....	7
<b>1.2 Osteoporosis.....</b>	<b>7</b>
1.2.1 Risk factors .....	9
1.2.2 Treatment options .....	10
<b>1.3 Diagnostic imaging techniques.....</b>	<b>13</b>
1.3.1 Radiographic absorptiometry (RA).....	14
1.3.2 Single-photon absorptiometry and single x-ray absorptiometry (SPA/SXA) ..	15
1.3.3 Dual-photon absorptiometry and dual x-ray absorptiometry (DPA/DXA) ...	16
1.3.4 Quantitative and peripheral quantitative computed tomography (QCT/pQCT) .....	17
1.3.5 Quantitative ultrasound (QUS) .....	19
1.3.6 Work in progress and current advances in diagnostic imaging .....	20
<b>1.4 Outline and aims .....</b>	<b>21</b>

---

**Chapter 2: "Basic Principles of Magnetic Resonance Imaging (MRI)". 24**

<b>2.1 The development of MRI</b> .....	<b>24</b>
<b>2.2 Simple spin physics</b> .....	<b>25</b>
<b>2.3 Production of the net magnetisation</b> .....	<b>27</b>
2.3.1 The rotating frame of reference .....	31
2.3.2 <i>RF</i> pulses and the free induction decay (FID) .....	32
<b>2.4 Relaxation mechanisms</b> .....	<b>33</b>
2.4.1 Spin-Lattice Relaxation and its time constant <i>T1</i> .....	34
2.4.2 Spin-Spin Relaxation and its time constant <i>T2</i> .....	35
<b>2.5 Principles of Magnetic Resonance Imaging</b> .....	<b>38</b>
2.5.1 Slice selection .....	38
2.5.2 Readout or frequency encoding .....	39
2.5.3 Phase encoding.....	40
2.5.4 From raw data to image data.....	41
<b>2.6 Pulse sequences</b> .....	<b>42</b>
2.6.1 The Spin-Echo (SE) MR pulse sequence.....	43
2.6.2 The Gradient-echo (GE) MR pulse sequence .....	44
<b>2.7 Safety issues in MRI</b> .....	<b>46</b>
2.7.1 Static field effects .....	46
2.7.2 <i>RF</i> effects .....	47
2.7.3 Gradient effects.....	47

**Chapter 3: "Investigation Of The Physical and Biomechanical Properties Of Bone And The Preparation Of The MRI Experimental Set-up" ..... 48**

<b>3.1 Preparation of the trabecular bone samples</b> .....	<b>49</b>
<b>3.2 Bone mineral density (BMD) measurements</b> .....	<b>52</b>
3.2.1 Method .....	53
3.2.2 Reproducibility assessment.....	53
<b>3.3 Dual Energy X-ray Absorptiometry (DEXA) experimental measurements</b> .....	<b>54</b>
3.3.1 Method .....	54
3.3.2 Reproducibility assessment.....	55
<b>3.4 Mechanical testing</b> .....	<b>56</b>
3.4.1 Method .....	56
3.4.2 Reproducibility assessment.....	59
<b>3.5 The relationships between the physical and biomechanical properties of bone</b>	<b>59</b>
3.5.1 DEXA (BMD) Vs calculated BMD .....	60
3.5.2 Young's Modulus (YM) Vs BMD .....	61
<b>3.6 Preparation of the MRI experimental set-up</b> .....	<b>62</b>

---

<b><i>Chapter 4: "Quantitative Magnetic Resonance (QMR) and its value in the investigation of Trabecular Bone"</i></b> .....	<b>69</b>
4.1 Theory .....	70
4.2 A review of the studies with the use of Quantitative Magnetic Resonance .....	76
4.3 Pilot studies – technical considerations.....	79
4.3.1 Imaging parameters.....	79
4.3.2 Data analysis .....	81
4.3.3 Reproducibility assessment.....	81
4.3.4 Effects of angle .....	83
4.4 Method .....	85
4.5 Results .....	86
4.5.1 QMR and BMD.....	86
4.5.2 QMR and YM .....	89
4.6 Discussion.....	90
4.6.1 QMR and BMD.....	91
4.6.2. QMR and YM .....	92
4.6.3 Translation of QMR to in-vivo situations.....	92
4.7 Conclusion .....	94
<b><i>Chapter 5: "Magnetic Resonance Microscopy (MRM) and its value in the investigation of Trabecular Bone"</i></b> .....	<b>95</b>
5.1 Theory .....	95
5.1.1. Magnetic field strength .....	96
5.1.2 Hardware.....	97
5.1.3 Imaging parameters.....	97
5.1.4 Pulse sequences.....	98
5.1.5 Image analysis.....	99
5.2 A review of the studies with the use of Magnetic Resonance Microscopy .....	104
5.3 Pilot studies – technical considerations.....	108
5.3.1 Technique optimization .....	108
5.3.2 Image processing .....	110
5.3.3 Reproducibility assessment.....	113
5.4 Method .....	113
5.5 Results .....	114
5.6 Discussion.....	118
5.6.1 MRM and the estimation of common trabecular bone histomorphometry measures.....	118
5.6.2 MRM in the assessment of bone strength .....	119
5.7 Conclusion .....	120

---

<b><u>Chapter 6: "Sub-Pixel Enhancement of Non-uniform Tissue (SPENT) and its value in the investigation of Trabecular Bone"</u></b> .....	<b>122</b>
<b>6.1 Theory</b> .....	<b>122</b>
6.1.1 Acquisition of SPENT – method 1 .....	124
6.1.2 Acquisition of SPENT – method 2 .....	125
6.1.3 Acquisition of SPENT – method 3 .....	126
<b>6.2 Pilot studies</b> .....	<b>127</b>
<b>6.3 Method</b> .....	<b>130</b>
6.3.1 Image analysis.....	131
<b>6.4 Results</b> .....	<b>132</b>
6.4.1 SPENT and BMD .....	133
6.4.2 SPENT and YM .....	137
<b>6.5 Discussion</b> .....	<b>138</b>
6.5.1 SPENT and BMD .....	139
6.5.2 SPENT and YM .....	140
6.5.3 Translation of the results into in-vivo situations.....	140
<b>6.6 Conclusion</b> .....	<b>141</b>
<b><u>Chapter 7: "Thesis Summary and Future Work"</u></b> .....	<b>142</b>
<b>7.1 QMR in the investigation of trabecular bone</b> .....	<b>142</b>
7.1.1 QMR in the investigation of BMD .....	142
7.1.2 QMR in the investigation of fracture prevalence.....	143
7.1.3 Future work .....	143
<b>7.2 MRM in the investigation of trabecular bone</b> .....	<b>144</b>
7.2.1 MRM in the investigation of BMD.....	145
7.2.2 MRM in the investigation of fracture prevalence .....	146
7.2.3 Future work .....	146
<b>7.3 SPENT in the investigation of trabecular bone</b> .....	<b>147</b>
7.3.1 SPENT in the investigation of BMD .....	147
7.3.2 SPENT in the investigation of fracture prevalence.....	147
7.3.3 Future work .....	147
<b>References</b> .....	<b>149</b>
<b>Bibliography</b> .....	<b>165</b>

---

## List of Figures

<b>Figure 1.1</b> Microscopic structure of bone .....	4
<b>Figure 1.2</b> Trabecular bone .....	5
<b>Figure 1.3</b> Normal resorption of bone.....	6
<b>Figure 1.4</b> Structural changes of trabecular bone due to osteoporosis.....	7
<b>Figure 1.5</b> Fracture of the neck of femur .....	8
<b>Figure 2.1</b> A rotating nucleus.....	25
<b>Figure 2.2</b> Random orientation of protons within a volume of tissue.....	27
<b>Figure 2.3</b> The Zeeman diagram .....	28
<b>Figure 2.4</b> Net magnetisation .....	29
<b>Figure 2.5</b> Precession of a proton .....	30
<b>Figure 2.6</b> The net magnetization during the RF pulse.....	31
<b>Figure 2.7</b> The rotating frame of reference .....	31
<b>Figure 2.8</b> The effect of 90 and 180 degree RF pulses on the net magnetization .....	32
<b>Figure 2.9</b> The precession of the net magnetization and the FID.....	33
<b>Figure 2.10</b> The return of the longitudinal magnetization (T1) .....	34
<b>Figure 2.11</b> Loss of transverse magnetization (T2).....	35
<b>Figure 2.12</b> Reversal of proton dephasing due to T2* with a 180 RF pulse.....	37
<b>Figure 2.13</b> The effect on the signal from a series of RF pulses. T2 and T2* .....	37
<b>Figure 2.14</b> The principle of slice selection .....	39
<b>Figure 2.15</b> Frequency encoding .....	40
<b>Figure 2.16</b> Phase encoding .....	41
<b>Figure 2.17</b> General SE pulse sequence diagram.....	43
<b>Figure 2.18</b> General GE pulse sequence diagram .....	45
<b>Figure 3.1</b> Trabecular stress groups in the head of femur.....	49
<b>Figure 3.2</b> Location where the bone cubes are cut .....	50
<b>Figure 3.3</b> DEXA scanning principle.....	55
<b>Figure 3.4</b> A typical load-displacement curve .....	56
<b>Figure 3.5</b> A three dimensional model of the trabecular bone cube .....	57
<b>Figure 3.6</b> Demonstration of strain .....	58
<b>Figure 3.7</b> A typical stress-strain curve.....	58
<b>Figure 3.8</b> Relationship between DEXA (BMD) and physical BMD.....	60
<b>Figure 3.9</b> Relationship between YM and BMD (gold standard) .....	61
<b>Figure 3.10</b> Two bone samples with identical BMD .....	62

---

<b>Figure 3.11</b> SNR calculation method .....	64
<b>Figure 3.12</b> Effects of inaccurate sample positioning .....	65
<b>Figure 3.13</b> The syringe used for the experiments .....	66
<b>Figure 3.14</b> The sample positioning device .....	67
<b>Figure 3.15</b> The complete experimental device .....	67
<b>Figure 4.1</b> Susceptibility variations within a sample .....	70
<b>Figure 4.2</b> Effect of magnetic field inhomogeneity on T2* .....	71
<b>Figure 4.3</b> Signal intensity versus TE for the determination of T2* .....	72
<b>Figure 4.4</b> The PRIME sequence .....	73
<b>Figure 4.5</b> Asymmetric SE pulse sequence .....	74
<b>Figure 4.6</b> Sample holder which allowed rotation of samples in various degrees .....	84
<b>Figure 4.7</b> Effects of angle on T2* .....	84
<b>Figure 4.8</b> R2' versus physical BMD .....	86
<b>Figure 4.9</b> R2* versus physical BMD .....	88
<b>Figure 4.10</b> R2 versus physical BMD .....	88
<b>Figure 4.11</b> R2' versus YM .....	89
<b>Figure 4.12</b> R2 versus YM .....	90
<b>Figure 5.1</b> High resolution image of a trabecular bone sample .....	96
<b>Figure 5.2</b> High resolution image with the corresponding image histogram .....	100
<b>Figure 5.3</b> Binarization of a high resolution image by thresholding .....	100
<b>Figure 5.4</b> The effect of PV on the intensity histogram .....	101
<b>Figure 5.5</b> Trabecular boundary identification .....	102
<b>Figure 5.6</b> Method for calculating the mean trabecular separation .....	103
<b>Figure 5.7</b> Schematic axial and oblique views of a phantom .....	109
<b>Figure 5.8</b> A high resolution image of a bone sample and the image histogram .....	111
<b>Figure 5.9</b> Identification of the threshold value from the image histogram .....	112
<b>Figure 5.10</b> BVF versus BMD .....	114
<b>Figure 5.11</b> BVF versus YM .....	115
<b>Figure 5.12</b> Mean Tb.Th versus YM .....	116
<b>Figure 5.13</b> Mean Tb.S versus YM .....	116
<b>Figure 6.1</b> SPENT in the x and y directions .....	123
<b>Figure 6.2</b> The pulse sequence diagram of SPENT .....	124
<b>Figure 6.3</b> Extraction of SPENT images from a standard high resolution image .....	125
<b>Figure 6.4</b> Extraction of SPENT images from a 3D data-set .....	126
<b>Figure 6.5</b> SPENT images of a phantom at different resolutions .....	128
<b>Figure 6.6</b> Proton density and combined SPENT images of a phantom .....	129
<b>Figure 6.7</b> Proton density image and SPENT images in different directions .....	130
<b>Figure 6.8</b> SPENT image processing .....	131
<b>Figure 6.9</b> Individual NSPENT versus BMD (96x96) .....	133
<b>Figure 6.10</b> xyz-NSPENT versus BMD (96x96) .....	134

---

---

<b>Figure 6.11</b> Individual NSPENT versus BMD (128x128).....	134
<b>Figure 6.12</b> NSPENT versus YM .....	137
<b>Figure 6.13</b> BMD versus YM.....	138

---

**List of Tables**

**Table 5.1** Results from the multiple regression analysis on 30 samples.....117

**Table 6.1** NSPENT signal versus BMD at different resolutions.....135

---

## **Acknowledgements**

I would like, first of all, to express my sincere thanks and gratitude to my supervisor Dr. Mic Farquharson for believing in me and offering me the opportunity to carry out this project. For his patience, understanding and support (both personally and academically) over the last 4 years, I will always be grateful.

During my 4 years in the Radiation Physics Laboratory at City University, I have also enjoyed working with fellow research students Allan Allday, Tina Geraki, Tarjani Patel and, more recently, Elaine Ryan. They have all been understanding and supportive and I will never forget their assistance and their good humour. I would like to take the opportunity to wish them all the best for the future. Before leaving from City University it would be a great omission not to mention Roger Hicks and Jennifer Edie of the Department of Radiography for their support and understanding, both for my MSc and PhD studies. I would also like to express my sincere thanks to Tom Rose for allowing the mechanical tests to be performed at City University.

At University College London (UCL), I was fortunate to work with very distinguished scientists in the field of MRI. The support and expert guidance of Prof. Roger Ordidge has played a vital role in the successful conduction of this project. I will always be grateful to him for allowing me to make use of the research facilities at UCL and also for giving me the opportunity to learn from his expert team (Dr John Thornton, Dr Andrew Priest and Dr Alan Bainbridge) in the Bloomsbury Laboratory. Of particular importance to me, however, has been the opportunity that I had to meet and work with David Carmichael who has recently completed successfully his PhD at UCL. His assistance, advice and willingness to share time with me have been invaluable. David has patiently taught me a lot of the complexities of MRI physics, has introduced me to computer

---

programming and image processing and has contributed a great deal to this project. His exceptional personality and good humour will never be forgotten. I must also thank Stewart Morrison and Denzil Booth from the Medical Physics workshop at UCL who have helped me make all sorts of devices and MRI phantoms.

I would also like to express my special thanks to the staff of the Orthopaedic Departments of St. Mary's hospital (Paddington, London) and Whipps Cross hospital (London) for appreciating the importance of this research work by allowing the collection of the bone samples used in this project. Also, special thanks to Dr. Ian Cullum of Middlesex hospital (London) for authorizing the conduction of the DEXA experiments.

Last but not least, I would like to express my sincere thanks to my family for their moral and financial support during my long studies in the UK and also to Yvonne for being there for me at all times. For these reasons, I would like to dedicate my work to them.

-----

"I grant powers to the University Librarian to allow this thesis to be copied in whole or in part without reference to me. This permission covers only single copies made for study purposes, subject to normal conditions of acknowledgement."

---

## **Abstract**

Osteoporosis is the commonest metabolic bone disease affecting a great number of people around the world. In osteoporosis, there is an increased porosity of bone as a consequence of the reduction of bone mineral density (BMD), which results in an increased risk of atraumatic fractures because the bones are no longer able to support normal stresses. Trabecular regions of bone have a far greater surface area for a given bone mineral density and can therefore be much more affected than cortical bone. Currently, in the clinical setting, BMD is typically measured using Dual-Energy X-ray Absorbtiometry (DEXA). However, DEXA is limited by its accuracy and imparts a dose of radiation as well. In addition, studies in the past have shown that BMD alone is not an ideal measure of fracture prevalence and the trabecular architecture should be considered as equally important when investigating fracture risk.

The main aim of this project is to investigate the value of Magnetic Resonance Imaging (MRI) as a new and safe technique in the characterization of trabecular bone that will indicate if MRI can be employed for the investigation of bone disorders like osteoporosis. Quantitative Magnetic resonance (QMR) and Magnetic Resonance Microscopy (MRM) techniques are investigated as a continuation of previous investigations. In addition, a novel MRI technique called Sub-Pixel Enhancement of Non-uniform Tissue (SPENT) is also presented that has not previously been investigated with respect to bone imaging. All of the MRI techniques in this study are investigated in-vitro with the use of 30 bone samples. The bone samples are 15mm sided cubes cut from a predetermined location from within the head of femur, cleaned and immersed in water for the MRI experiments. The MRI derived data are then compared with the gold standard properties of these samples identified from physical calculations (i.e. BMD calculation) and mechanical testing (i.e. to determine the Young's modulus of elasticity, which is a recognized strength indicator) in order to provide an understanding of the potential value of these MRI techniques to provide information relating to Bone Mineral Density (BMD) and fracture prevalence.

## **Chapter 1: "Introduction"**

*"Increased human life span has led to a rapid increase in the elderly population and a concomitant rise in the prevalence of osteoporosis" (Wehrli et al, 2000, p.527)*

The term "osteoporosis" is a term used widely in everyday life. It is often associated with old age and therefore assumed to impose no major threat to various age groups. However, when considering the average human life span, the situation becomes more critical. Statistics reveal that 33% of all women and 20% of all men in the world will sustain a fracture related to osteoporosis during their otherwise healthy lifetime (Cummings & Melton, 2002). The fractures can be related to incidents of minor trauma or even atraumatic in advanced cases, which means that the skeleton cannot support its own body weight. Common atraumatic fractures include the spine (compression or stress fractures) and the hip. Minor trauma related fractures include the extremities, the most common being the wrist. The onset of osteoporosis seems to be associated with middle-aged groups and advances towards the last quarter of life.

Studies have shown that the detection of osteoporosis in the early stages results in the most effective treatment. Many treatment options are available at the present time and continuing efforts are resulting in more effective treatments becoming available. However, inaccurate assessment of the condition (i.e. lack of diagnostic accuracy) can result in more (or the wrong) medication being administered (with possible adverse effects to other body organs) or less medication allowing for the progression of the disease towards more advanced levels.

Although the onset of osteoporosis can be reduced with more effective public awareness of the risk factors involved, the most important parameters related to the disease are inherent to the normal biological progression of the body itself.

---

In this chapter, a more detailed description of osteoporosis is presented followed by the current diagnostic modalities available for the detection of the condition. However, in order to appreciate the biological changes pertinent to osteoporosis (that the diagnostic modalities strive to detect), the normal anatomy and structure of bone is initially presented. The chapter closes with the aims and objectives of this project drawn in the light of the background information provided in this chapter.

### ***1.1 Structure and function of bone tissue***

Bone, or osseous tissue, is one of the most specialised forms of connective tissue that constitutes the skeleton in various shapes. The principal functions of the skeleton are mechanical support, maintenance of calcium homeostasis and hematopoiesis in the bone marrow. The mature cells of bone, osteocytes, are embedded in a unique matrix material containing both organic collagen material and inorganic salts.

The inorganic (bone mineral) portion makes up about 60-70% of the total matrix material and is responsible for the hardness of bone and much of its rigidity (Williams, 1989). The mineral portion of mature bones is composed largely of crystals made of a substance generally referred to as hydroxyapatite, but with an important carbonate content and a lower calcium to phosphate ratio than pure hydroxyapatite (Williams, 1989). Under the microscope, bone crystals are seen packed closely together with narrow gaps between them containing water and organic macromolecules. The number and size of the crystals increases in mature bone with time and the water content decreases.

The organic matrix of bone, which makes up 30-40% of the total matrix material, is a composite of collagen (90%) and an amorphous mixture of protein and polysaccharides (i.e. osteocalcin, sialoprotein, proteoglycans and osteonectin) called ground substance (10%). Although there are ten genetically different types of collagen with specific tissue distributions and properties suited to their functions, normal adult bone collagen is deposited in layers of parallel fibers of uniform diameter (Francis, 1990). The unique arrangement of collagen in bone not only adds to overall strength but also gives bone

---

some degree of plastic-like resilience so that applied stress (within limits) does not result in frequent crush or fracture injuries (Thibodeau & Patton, 1993).

#### 1.1.1 Bone cells

Despite their relatively small number in a large organic and inorganic tissue, bone cells dictate the structure of the skeleton. The three major cell types in bone are osteoblasts, osteocytes and osteoclasts (Francis, 1990). Osteoblasts, derived from fibroblastic stem cells, are responsible for the synthesis of the bone matrix. They mature into osteocytes which lie in concentric layers within mineralized bone and serve to control local mineralization and mineral exchange between bone and plasma. Osteoclasts are multinucleate cells, derived from the monocyte-macrophage series which resorb calcified bone or cartilage. (Francis, 1990).

On examining a section of any bone, it is seen to be composed of two kinds of tissue. One of these is dense in texture and is termed compact or cortical bone (80% of the skeleton), and the other consists of slender fibers and lamellae, which join to form a sponge-like structure called trabecular or spongy bone (20% of the skeleton). Cortical bone is the compact layer which predominates in the shafts of long bones whereas trabecular bone forms the interior meshwork of bones, particularly the vertebrae, pelvis and the ends of long bones. These two types of bone tissue will be described in detail in following sections with particular attention to trabecular bone since this type of bone tissue is more likely to be affected by osteoporosis.

#### 1.1.2 Compact bone

As mentioned above, adult bone consists almost entirely of a mineralized matrix with collagen fibres arranged in layers, embedded in which are the osteocytes. While the mechanical properties of bone are dependent on the general composition of its matrix, the manner in which the different components are arranged is also of great importance in its strength and resilience. In the most immature state of developing bone tissue (woven bone), collagen fibres and the bone crystals within them are arranged in an irregular manner, whereas in the adult osseous skeleton, they form many cylinder-shaped

structural units called osteons or Haversian systems (see figure 1.1). Many of these units cemented together form the substance of compact bone. Haversian systems usually lie parallel to each other but they frequently spiral, branch or intercommunicate and some end blindly (Williams, 1989).

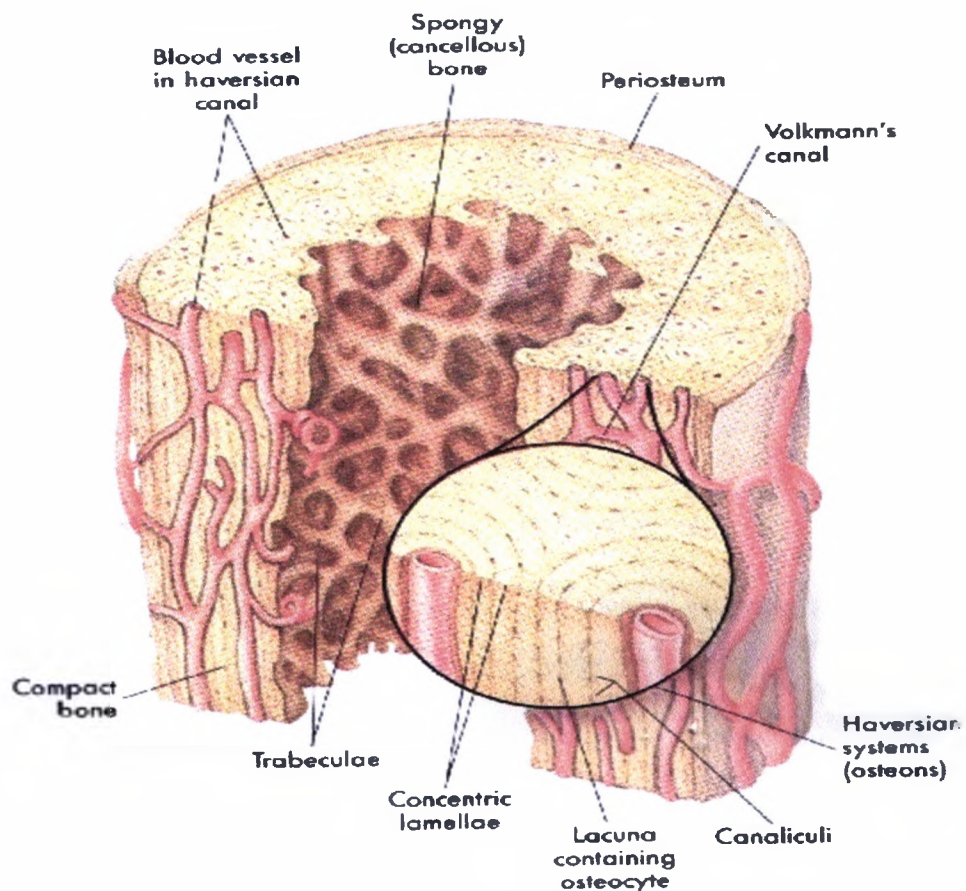


**Figure 1.1.** Microscopic structure of bone (Thibodeau & Patton, 1993).

Four types of structure make up each osteon, or Haversian system: 1) the lamellae, which are concentric cylinder-shaped layers of calcified matrix, 2) the lacunae, which are small spaces containing tissue fluid in which bone cells lie imprisoned between the hard layers of the lamellae, 3) the canaliculi, which are very small canals radiating in all directions from the lacunae and connecting them to each other and into the Haversian canal and 4) the Haversian canals which extend lengthwise through the center of each Haversian system and are interconnected by transverse perforating canals (Volkmann's canals).

---

The periosteum adheres to the surface of each bone on which strong tendons or ligaments are attached. It also serves as a base for the blood vessels prior to their distribution in the bones. Bones are generally richly supplied with blood, via periosteal vessels that enter close to the articular surfaces and nutrient arteries passing obliquely through the cortex before dividing into longitudinally directed branches in the Haversian canals.

### 1.1.3 Trabecular bone

Cancellous or trabecular bone differs in microscopic structure from compact bone. There are no Haversian systems in cancellous bone. Instead, it consists of needle like bony spicules called trabeculae (see figure 1.2).

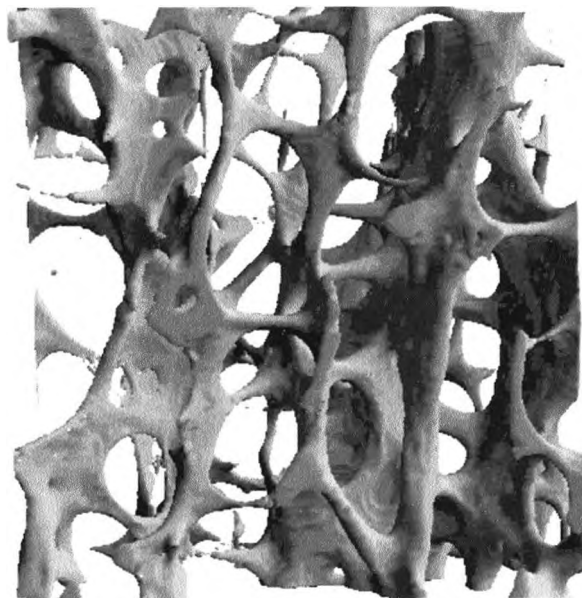


**Figure 1.2.** Trabecular bone (picture taken from the Berkeley Orthopaedic Biomechanics Laboratory, in the Department of Mechanical Engineering at <http://biomech2.me.berkeley.edu/>).

Bone cells are found within the trabeculae. Nutrients are delivered to the cells and waste products are removed by diffusion through tiny canaliculi that extend to the surface of the very thin spicules. The placement of trabeculae in the cancellous bone is not as random as it might appear. Rather, the bony spicules are arranged along lines of stress, and their orientation will therefore differ between individual bones according to the nature and magnitude of the applied load (Thibodeau & Patton, 1993). For example, the shafts of

---

long bones, such as the radius and ulna, are at least 90% cortical bone whereas vertebrae and the ends of long bones are mostly composed of trabecular bone (Schlenker & Von Seggen, 1976).

This natural arrangement of trabecular bone is vital in the general strength of the skeleton throughout life. However, trabecular bone, with its greater surface area, is metabolically more responsive to influences which alter mineral homeostasis. Mineral homeostasis refers to a remodeling cycle which involves the normal production and resorption of bone in the adult skeleton.

At the beginning of each normal remodeling cycle, osteoclasts appear on a previously inactive surface and, over a period of 2 weeks, construct a tunnel in cortical bone or a lacuna on the surface of trabecular bone (see figure 1.3). The osteoclasts are replaced by osteoblasts, which fill in the resorption cavity over a period of 3-4 months to create a new structural unit of bone (Francis, 1990). In young healthy adults the two actions are tightly coupled and bone mass is maintained. However, in advanced disruption of the mineral homeostasis (i.e. osteoporosis) there is a relative or absolute increase in resorption over formation, which compromises the strength of individual bones and, consequently, the entire skeleton (i.e. occurrence of fractures).

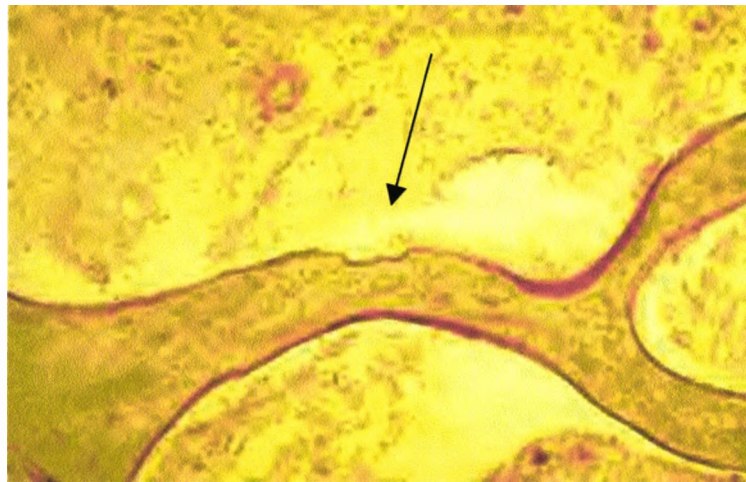


**Figure 1.3.** Normal resorption of bone shown on a single trabeculum (picture taken from the Virtual Histology Laboratory at <http://dahweb.engr.ucdavis.edu/dahweb/126site/strut.htm>).

---

#### 1.1.4 Bone marrow

Bone marrow is a specialised type of soft, diffuse connective tissue called myeloid tissue. It serves as the site for production of blood cells and is found in the medullary cavities of long bones and in the spaces of trabecular bone. On gross examination, the bone marrow may be either red owing to the hemoglobin of the erythrocytes and indicating active hematopoietic marrow, or yellow due to the presence of carotenoid derivatives dissolved in fat droplets from adipocytes (Piney, 1922). In an infant's or child's body, virtually all of the bones contain red marrow. It is named for its function in the production of red blood cells and contains 60% haematopoietic cells and 40% fat cells. In adults, approximately half of the medullary cavity, mainly in the appendicular skeleton, is occupied by yellow marrow. Its chemical composition is about 80% fat, 15% water and 5% protein (Vande Berg et al, 1998).

#### *1.2 Osteoporosis*

Osteoporosis is the commonest metabolic bone disease. It is already an important public health concern in all developed countries and is becoming one in most developing countries (Majumdar & Genant, 1995a). In osteoporosis the skeletal system loses bone volume and mineral content. Within affected bones, trabeculae are lost, and the bones develop spaces and canals (see figure 1.4).

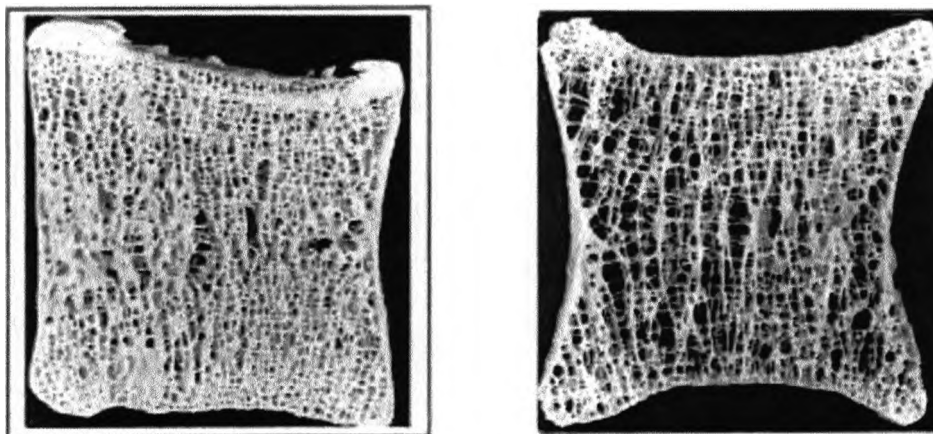


**Figure 1.4.** Structural changes of trabecular bone due to osteoporosis demonstrated in a sagittal view of a human vertebra. The vertebra on the left is from a healthy individual and on the right from an individual with osteoporosis (picture taken from [http://www.chrislangton.co.uk/clip/html/Aspects%20of%20Osteoporosis/skeleton\\_\\_\\_bone.html](http://www.chrislangton.co.uk/clip/html/Aspects%20of%20Osteoporosis/skeleton___bone.html))

---

Since trabecular regions of bone have a far greater surface area for a given bone mineral density when compared to that of cortical bone this leads to a more active remodelling metabolism, which can be 3 to 4 times more than cortical bone (Pacifci and Avioli, 1993). The effect of this bone loss results in an increased risk of atraumatic fractures because the bone is no longer able to support normal stresses.

Due to the association of osteoporosis with age, the number of incidences is set to rise as the average age of the world's population increases. While there are genetic factors that can cause the early onset of osteoporosis, it is a universal problem from middle age onwards. The main danger to people with osteoporosis is a bone fracture that can result in an increased chance of disability and morbidity. Hip fractures are the most important type of osteoporotic fractures, both in terms of direct health costs and social effects on the patient (see figure 1.5).



**Figure 1.5.** X-ray demonstrating a fracture of the neck of femur due to osteoporosis (picture taken from <http://www.radiographersreporting.com>).

---

Falling is one of the main factors responsible for hip fractures in old people. The prevalence of falls increases with advancing age in both sexes but is generally higher in women than men (Prudham & Evans, 1981). One study calculated that 67% of accidental deaths in females aged over 65 years were as a result of falling and a fractured femur is associated with 33% mortality within one year (Swift, 2001). A number of risk factors for falls have been identified in the elderly, the most common of which are muscle weakness, history of falls, gait and balance deficit, visual impairment, arthritis, depression and generally the age of 80 and above (Francis, 2001).

The cost of treating hip fractures alone has been estimated by the Department of Health at 750 million pounds in the UK annually. The Department of Health report also predicts that the ageing population of the UK will cause a doubling in the number of osteoporotic fractures over the next 50 years if changes are not made to present practice.

#### 1.2.1 Risk factors

Factors that increase the risk of osteoporosis include hormone deficiency, race and genetic influences, lack of physical exercise and nutrition. In females, declining levels of the hormone estrogen contribute to the development of osteoporosis and estrogen replacement therapy may be required in many cases in order to prevent further development of the disorder (Francis, 1990). In men, testosterone deficiency is similarly associated with bone loss and can be reversed with testosterone replacement. Menopausal status in women, however, is probably the most important risk factor for osteoporosis. Women with an early menopause or having bilateral oophorectomy have lower bone mineral density at all sites and increased risk of subsequent fracture. The earlier the menopause, the greatest the risk appears to be.

Racial factors also influence bone mineral density. For example, black women, whether in Africa or in the USA, appear to have greater bone density than whites of the same age and sustain fewer related fractures (Cohn et al, 1977). People of Asian origin often have lower bone densities than whites and, consequently, higher fracture rates.

---

Bone is also responsive to physical strain. Changes in the forces applied to bone produce effects in bone. For example, immobilization can induce marked degrees of bone loss. On the other hand, athletes tend to have greater bone mineral density, although this effect is often site specific. For example, tennis players may have increased bone density in their dominant hand and weightlifters may have greater femoral bone density than other athletes (Francis, 1990).

Additional factors that increase the risk of osteoporosis include nutrition, alcohol consumption, smoking and the intake of certain medications. The low intake of dietary calcium is often related to osteoporosis. In addition, the high intake of sodium has been shown to increase renal calcium excretion, which has led to the suggestion that low intake of dietary sodium combined with an appropriate intake of calcium may diminish the age-related bone loss (Francis, 1990). Certain types of medications used for the treatment of conditions other than osteoporosis (i.e. corticosteroids) have also been shown to decrease calcium absorption in the intestines with a concomitant urinary calcium excretion.

#### 1.2.2 Treatment options

While public awareness of the risk factors presented in the previous section is the best measure towards the prevention of osteoporosis, the condition may still develop in a large percentage of the population and effective therapeutic measures have to be considered at the earliest possible stage in order to allow for a most effective treatment. A number of therapeutic agents have actions on bone and are used in the treatment of osteoporosis. They may be classified into agents which predominantly reduce bone resorption and therefore reduce or prevent further bone loss, and those which stimulate bone formation thereby increasing bone mineral density (BMD).

The hormone Oestrogen has a profound antiresorptive action on bone cells, and its reduction at the time of menopause is an important cause of bone loss (Francis, 1990). However, being an antiresorptive agent, it is incapable of repairing significant loss once it has occurred. On the other hand, since it appears likely that fracture risk will increase as

---

bone mass reduces, any therapy that reduces further bone loss will decrease the risk of subsequent fractures. Studies of the effects of oestrogen upon bone have demonstrated a dose-response effect (Horsman et al, 1983), suggesting that when adequate doses are administered, a more effective treatment can be achieved. However, studies have shown that these adequate doses of oestrogen are also associated with a variety of complications ranging from minor side-effects like nausea, fluid retention, headaches and increased blood pressure, to a more serious thromboembolic disease and even cancer (Hunt et al, 1987).

The association of oestrogen replacement therapy (ERT) and breast cancer is an area that has created a lot of confusion and media attention over the last 10 years. While ERT was thought to be the most effective treatment option and used for many years, a recent large-scale UK study has put an end to its routine administration. The "Million Women Study" was published in the August 9, 2003 issue of the *Lancet* (Beral, 2003). Led by Valerie Beral and colleagues of the Cancer Research UK Epidemiology Unit in Oxford, the study reviewed medical data from over one million women aged 50 to 64 who enrolled in the study between 1996 and 2001. Results showed that current and recent use of hormone replacement therapy (HRT) increased the risk of breast cancer. Specifically, women who used prolonged HRT treatment were found to be more affected than women who received short-term treatment. In addition, women with family history of breast cancer were more likely to be affected by HRT. While HRT is undoubtedly the most effective way to treat the bothersome symptoms of menopause, clinicians and patients can now better weigh the true benefits and risks of HRT.

As a result of the controversy over the use of HRT in the treatment of osteoporosis, other drug groups have recently been introduced. Bisphosphonates are a class of chemicals that strongly inhibit osteoclast-mediated bone resorption without significantly affecting bone formation (Fleisch, 1997). Alendronate and risendronate are the most commonly used bisphosphonates on the market and have been thoroughly tested in a great number of clinical trials (Watts, 2001). The osteogenic action of bisphosphonates and their relative lack of unwanted activity outside the skeleton have led to an increased use of these agents

---

in treating osteoporosis. Studies looking into the effectiveness of bisphosphonates have shown a 65% reduction in the risk of vertebral fractures within one year (Harris et al, 1999) and a 70% reduction in 3 years (Heaney et al, 2002). Bisphosphonates have also been shown to reduce the risk of fractures at sites other than the vertebrae but to a lesser extent (ibid.). Significant side effect from the use of bisphosphonates have not been reported yet and some clinicians now even advice the administration of these agents to women that do not suffer from osteoporosis but fall within the concerned age groups (McClung et al, 1998).

The use of calcium supplements (or a combination of vitamin D and calcium supplements) seems to be the choice for many individuals in the age groups concerned. The rationale for their use is that the majority of individuals take insufficient calcium in their diet to offset the obligatory loss of calcium in the digestive juices and urine, and that calcium is drained from the skeleton to maintain normal homeostasis (Francis, 1990). However, studies have shown that calcium supplements may prevent some bone resorption in cortical bone but not in trabecular bone (Riis et al, 1987). By considering the importance of trabecular bone with respect to overall strength of the skeleton, there can be little justification for the intake of these supplements despite their general availability. Calcium supplementation is, therefore, no substitute for oestrogen or progestogen therapy but may be useful, however, in patients who are unable or unwilling to take hormone replacement therapy because of age, contraindications or side-effects (Francis, 1990).

Several compounds that increase bone mass have recently been investigated. However, at present, much less is known about these agents than the use of the antiresorptive agents described above. The use of testosterone in both male and female patients is currently being investigated. Preliminary studies have shown that testosterone appears to increase bone mass by stimulating bone formation in men (Francis et al, 1987). The same effect has been observed in women, but in both cases, considerable attention is required to avoid unacceptable side-effects. For this reason studies at the present time involve the administration of gradually increasing doses of testosterone in both sexes for the

---

establishment of their long-term safety. Apart from testosterone, anabolic steroids have also been used for the treatment of osteoporosis. However, there are considerable doubts about their long-term safety particularly in women since, the androgenic side-effects observed so far are of less importance when used in men.

Perhaps the most powerful and effective drug currently available (in the class of drugs that can increase bone mass) is parathyroid hormone (PTH). Unlike therapy with antiresorptive agents (oestrogen, bisphosphonates) that all function by decreasing bone resorption, PTH stimulates new bone formation and can increase bone mass. Studies have shown that daily injections of PTH for a period of around 20 months can increase BMD in the lumbar spine by 13.7%, reduce the risk of spinal fractures by 69% and non-spinal fractures by 40% (Neer et al, 2001). However, the long term effect of PTH therapy on BMD and fracture risk remains to be determined, as well as its potential use in combination with the antiresorptive agents described above.

### ***1.3 Diagnostic imaging techniques***

In the past decade, efforts from both clinicians and researchers to act purposefully for the effective interception of osteoporosis have resulted in the development of many methods for assessing the skeleton non-invasively. Based on a recognised need for the detection of osteoporosis at its earliest possible stage, considerable progress has been made in the field and there are many techniques that have recently entered the diagnostic arena for the evaluation of patients with suspected osteoporosis. However, these techniques vary in precision, accuracy and discrimination and differ substantially in fundamental methodology and general availability.

For the sake of clarity, 'precision' is defined in this section as the quality of any diagnostic imaging technique of being reproducible in performance. Apart from diagnosing a certain disease, the importance of reproducibility is great in terms of monitoring therapeutic response and disease progression as well since, any deviation in the performance of an imaging technique (i.e. in repeated experiments), may act in favor or against the chosen therapeutic measure and eventually the patient management.

---

'Accuracy' is defined here as the quality of any diagnostic imaging technique to provide information equal to the true value.

In 1994, an expert panel of the World Health Organization (WHO) proposed criteria for the diagnosis of osteoporosis in women (Kanis et al, 1994). The diagnosis is based on the relative BMD of an individual as compared to a healthy younger population (female 25 years of age) with normal bone mass. BMD values which fall well below the average for the 25 year old female (stated statistically as 2.5 standard deviations below the average or T-score  $< -2.5$ ) are diagnosed as osteoporotic. If a patient has a BMD value less than the normal 25 year old female, but not 2.5 standard deviations below the average (T-score  $> -2.5$  and  $< -1$ ), the bone is said to be osteopenic (osteopenic means decreased bone mineral density, but not as severe as osteoporosis).

Radiographic absorptiometry (RA), single-photon absorptiometry and single x-ray absorptiometry (SPA/SXA), dual-photon absorptiometry and dual x-ray absorptiometry (DPA/DXA), quantitative and peripheral quantitative computed tomography (QCT/pQCT) and quantitative ultrasound (QUS) are the most common modalities found in the clinical setting. A detailed review of these techniques is beyond the scope of this study. However, a brief overview of each will provide the reader with a foundation enabling an appreciation of the value of each of these techniques in the clinical setting.

### 1.3.1 Radiographic absorptiometry (RA)

RA (also known as photodensitometry) was one of the first quantitative techniques used to assess bone mass. In RA, hand radiographs are taken with aluminium wedges placed on the films and analysed using an optical densitometer. Usually, the middle phalanges or metacarpals are studied and the bone mineral density (BMD) is calibrated relative to that of the aluminium wedge and is expressed in arbitrary units (Genant et al, 1996). Although RA is an inexpensive and readily accessible technique, it was characterised by high precision errors of about 9-10% (Morgan et al, 1967). However, recently, the introduction of computer-assisted methods have greatly reduced operator errors and improved precision in the range of 1-2% (Genant et al, 1996).

---

One of the most important disadvantages of this technique is the fact that it does not provide information regarding trabecular architecture separately from cortical bone and therefore little information with respect to fracture prevalence. In addition, the results from the use of the technique to the peripheral sites of the skeleton cannot be extrapolated confidently to predict the status of more important sites (e.g. the spine and the hips). RA is used in approximately 500 centers worldwide but its use is becoming less common due to the introduction of more accurate techniques (Genant et al, 1996).

### 1.3.2 Single-photon absorptiometry and single x-ray absorptiometry (SPA/SXA)

SPA has been in use for more than 40 years for the assessment of BMD at peripheral sites (e.g. distal or ultradistal radius and calcaneus) but recently, the technique has been superseded by SXA. Both techniques have their rationale in the transmission of a highly collimated photon beam through a sample and measuring the attenuation at the measurement site in order to make a quantitative assessment of BMD (Genant et al, 1996). However, the use of an x-ray tube with SXA rather than a radionuclide source (usually <sup>125</sup>I) with SPA, has imparted better precision and improved spatial resolution to these systems and has reduced examination times (Kelly et al, 1994). The main advantages of these techniques are the reduced examination times, high availability and portability.

The main disadvantage of these techniques is the fact that it can only be used at peripheral sites and it involves a considerable amount of ionizing radiation. In addition, separate measurement of trabecular and cortical bone is not possible which means that it can provide little information regarding fracture prevalence. The precision of SPA has been shown to be approximately 2% for the distal radius (Nelson et al, 1992). The recent replacement of the radionuclide source with an x-ray tube in SXA has improved the errors of the technique to 0.8-1.2% (Gluer et al, 1992). Worldwide there are over 2000 SPA/SXA systems in use (Genant et al, 1996) although the numbers of these are reducing in response to the technological advances in the field.

---

### 1.3.3 Dual-photon absorptiometry and dual x-ray absorptiometry (DPA/DXA)

As previously described, single energy measurements (i.e. with the use of SPA and SXA) are not possible at sites with variable soft tissue thickness and composition (i.e. the axial skeleton, hip, or whole body) and examinations are restricted to peripheral sites. This was the main reason for the development of dual-photon absorptiometry (DPA) techniques which were introduced to correct for unknown path length in the body (Genant et al, 1996). The technique that uses a radionuclide source (typically  $^{153}\text{Gd}$  at two effective energy levels of 44keV and 100keV), was used for the assessment of BMD in a variety of sites in the skeleton.

Dual x-ray absorptiometry (DXA), introduced commercially as the direct successor to DPA, uses the same principles as DPA with the only difference being the replacement of the radionuclide source with an x-ray tube (Genant et al, 1996). The advantage of this is reduced examination times due to an increase in photon flux from the x-ray tube and greater accuracy and precision caused by higher resolution and removal of errors due to source decay correction (Genant et al, 1996). Depending on the manufacturer, two distinct energy level beams are either generated by an x-ray generator with alternate pulses at 70kVp and 140kVp, or filtered from an x-ray spectrum (Guglielmi et al, 1995). In recent days, DXA is more commonly refer to as DEXA scanning (i.e. Dual Energy X-ray Absorptiometry) and remains the method of choice for the investigation of osteoporosis.

Anatomical sites for DEXA measurement include the lumbar spine, the proximal femur, and the whole body, but peripheral sites can also be scanned. Examination times were initially in the region of 6-15 minutes but were reduced to 2 minutes or less with the introduction of higher powered generators and the use of a fan beam instead of a pencil beam (Mazess et al, 1992). Studies looking into the precision of the technique in vivo are numerous.

The precision of the technique in the examination of the lumbar spine has been shown to be in the region of 0.5-1.5% with an accuracy error of 5-10% (Genant et al, 1996). The

---

routine examination of the lumbar spine involves postero-anterior measurements with the patient lying supine. However, because of the presence of osteophytes, aortic calcifications, degenerative facet hypertrophy and intervertebral disc space narrowing in degenerative disc disease, the BMD may be increased artificially in the postero-anterior measurement of the lumbar spine (Wehrli et al, 1995). This is an important drawback of the technique particularly in the elderly population who are more likely to suffer from one or more of the above conditions. While investigators suggested that a lateral measurement of the spine alleviates the problems described above (Uebelhart et al, 1990) others have come to realise that the reproducibility of the lateral measurements is much lower due to errors arising from the large path length of soft tissue that the x-ray beam passes through in the lateral decubitus position of the body (Rupich et al, 1990).

DEXA has also been employed for measurements of the appendicular skeleton. Most standard DEXA densitometers allow for highly precise measurements of the radius, calcaneus and the forearm with reported precision errors of 0.8-1.3%, and accuracy errors of 4-8% (Nutti et al, 1991). However, measurements of the spine and the femur have been the most preferred sites for BMD measurements since most of the osteoporosis related atraumatic fractures occur in these locations rather than the extremities.

During recent years, DEXA has become the standard against which all other techniques are compared for the measurement of BMD in risk assessment. DEXA is relatively inexpensive technique and involves very low doses of radiation. On the other hand, it is a projection technique that provides integral BMD (expressed in grams per square centimeter) and thus cannot be used to distinguish between trabecular and cortical bone. The worldwide distribution of DEXA systems is over 6000 (Genant et al, 1996).

#### 1.3.4 Quantitative and peripheral quantitative computed tomography (QCT/pQCT)

Generally, spinal QCT measurements are performed on standard clinical CT scanners by employing an external bone mineral reference phantom to calibrate the CT measurements to bone-equivalent values. In addition, special software allows for selective measurement of trabecular bone only by placing regions of interest automatically within the vertebral

---

bodies. The software locates the vertebral body, maps its outer edges and employs anatomic landmarks such as the spinous process and spinal canal to calculate sizes and locations of the regions of interest. Since the metabolic rate of trabecular bone is substantially greater than that of cortical bone, the ability of QCT to selectively measure trabecular bone gives it comparatively good sensitivity for measurement of bone loss (Genant et al, 1996).

QCT can be performed in single-energy (SEQCT) or dual-energy (DEQCT) modes which differ in accuracy, precision and radiation dose (Genant & Boyd, 1977). Although dual-energy approaches have been shown to provide higher precision (Goodsitt et al, 1987), the associated high radiation dose required make this technique currently unsuitable for use in the clinical setting and therefore, the technique is only employed for research studies in-vitro.

In-vivo studies that have been carried out using QCT have demonstrated the ability of the technique to provide better sensitivity than projectional methods such as DXA or DPA (Genant et al, 1996). In addition, the recent development of three-dimensional (volumetric) computed-tomography (vQCT) techniques, have been shown to further improve spinal measurements as well as to enable the QCT assessment to other skeletal sites like the proximal femur.

As well as trabecular BMD, the two main factors that affect bone strength are the trabecular network architecture and the thickness of the cortical shell. Newer CT developments are trying to address these issues (Guglielmi et al, 1995). The development of high resolution, thin slice computed tomography enables the clear display of structural information. However, the obtainment of high resolution images involves higher radiation dose and the results vary substantially according to which image processing technique is used (Genant et al, 1996).

The QCT technique has been shown to offer precision and accuracy errors of approximately 1-4% and 4-15%, respectively (Guglielmi et al, 1995). These errors have

---

been assigned partly to the image processing techniques used but mainly to the plethora of calibration phantoms available for use with the QCT technique. The results from different types of calibration phantoms may not be interchangeable and in longitudinal studies it is essential that the same reference phantom is used.

Although QCT techniques have been extensively used for the assessment of the spine, peripheral quantitative computed tomography (pQCT) has also been employed for the measurement of BMD of the peripheral skeleton (usually the radius). However, pQCT requires the use of special purpose scanners and clinical applications are currently limited. Ease of use and the ability to assess separately cortical and trabecular bone, make the method an interesting alternative to SPA or SXA, and there are more than 1000 systems currently in use (Genant et al, 1996).

In a number of studies, pQCT measurements of BMD at the radius were found to be successful in distinguishing between osteoporotic and non-osteoporotic patients, and in monitoring subjects during clinical studies (Grampp et al, 1999). In addition, modern pQCT scanners also offer the opportunity to use multi-slice data acquisition, covering a larger volume of bone as compared with the most commonly used single-slice technique (Kaisel & Ruegsegger, 1991). The measurement of several slices is potentially more accurate for the detection of individual changes in the distal radius, and may therefore more accurately reflect bone status (Grampp et al, 1999).

#### 1.3.5 Quantitative ultrasound (QUS)

The use of QUS for the assessment of skeletal status has recently been given considerable attention by many clinicians and investigators mainly because of its low cost, portability, ease of use, and freedom from ionising radiation (Genant et al, 1996).

Ultrasound properties can be measured by reflection or transmission (Antich et al, 1991). Current commercial systems rely on sonic transmission using two ultrasound transducers (a transmitter and a receiver) positioned on each side of the tissue to be measured. These devices measure ultrasound parameters primarily in trabecular bone at the calcaneus and

---

patella, cortical bone at the tibia, and integral bone at the phalanges (Genant et al, 1996). The parameters measured include ultrasound transmission velocity (UTV), which is quoted in meters per second and/or the frequency dependency of the attenuation of the ultrasound signal, called broad-band ultrasound attenuation (BUA) which is reported in units of decibels per megahertz.

Studies carried out have shown that the parameters measured with ultrasound are influenced not only by bone density but also bone structure and composition and it is generally believed that both BUA and UTV are determined by bone density and bone microarchitecture (Genant et al, 1996). Studies have also shown that the accuracy of measurements is difficult to assess because the complex structure of bone and its inhomogeneity result in variable conduction paths and transit times and make determination of true velocity (in the case of UTV measurements) ambiguous (Gluer et al, 1994). On the other hand, BUA measurements have been shown to be influenced by connectivity and trabecular separation despite the significantly high correlations found between BUA and BMD (Gluer et al, 1992). The precision error for UTV measurements is about 0.3-1.5% and for the BUA 0.9-6.3% (Genant et al, 1996).

The promise of QUS may lie in the apparent dependence of the ultrasound parameters on bone structure. It has been shown that the strength of bone relates to both BMD and structure of bone. Therefore, if ultrasound is shown to reflect structural characteristics of bone, it may provide important information to augment that obtained by current x-ray based measures (DXA and QCT) of bone density.

#### 1.3.6 Work in progress and current advances in diagnostic imaging

As seen in previous sections there are a variety of imaging techniques currently available for the investigation of osteoporosis in the clinical setting. However, these techniques are mainly x-ray based (apart from QUS which has not yet been used routinely in the clinical setting) and vary in precision, accuracy and discrimination and differ substantially in fundamental methodology and general availability. Although these current techniques provide invaluable information at the present time, the introduction of new techniques

---

that offer at least equivalent information (with at least equivalent examination times) and without the unwanted effects of ionising radiations, should be strongly encouraged and supported.

With this in mind, several investigators have recently explored the possibility of using Magnetic Resonance Imaging (MRI) in the investigation of trabecular bone and preliminary findings have been promising. Since its introduction in the early 1970s, MRI has revolutionised medical imaging. Although direct MR measurements of mineralised elements in skeletal imaging has been relatively unsuccessful, trabecular bone investigations have been shown to be possible by assessing the surrounding bone marrow. Preliminary studies in-vitro have provided data to appreciate the potential of the technique to provide information relating to both BMD and trabecular architecture.

Studies have recently employed Quantitative Magnetic Resonance (QMR) methods and Magnetic Resonance Microscopy (MRM) to study trabecular bone. QMR refers to the investigation of the relaxation properties of bone marrow in an effort to extract information regarding BMD and trabecular architecture. MRM involves the acquisition of high resolution images for the extraction of similar information directly from the images. Although preliminary findings have shown promising results, more studies in this field with the use of larger sample populations are needed to further investigate the potential of these methods.

#### ***1.4 Outline and Aims***

The main aim of this project is to investigate the value of MRI in the characterization of trabecular bone that will indicate if MRI can be employed for the investigation of bone disorders like osteoporosis. QMR and MRM techniques are investigated as a continuation of previous investigations. In addition, a novel MRI technique called Sub-Pixel Enhancement of Non-uniform Tissue (SPENT) is also presented that has not previously been investigated with respect to bone imaging. All of the MRI techniques in this study are investigated in-vitro with the use of a large number of bone samples. The MRI derived data are then compared with properties of these samples (i.e. gold standard)

---

identified from physical calculations (i.e. BMD calculation) and mechanical testing (i.e. to determine the Young's modulus of elasticity, which is a recognized strength indicator).

In chapter 2, an outline of the MRI basic principles is given. While the vast amount of theoretical principles relating to MRI have been reduced pertinent to the use of the modality in the investigation of bone tissue, an overview of the basic general principles is deemed necessary. Therefore, the aim of this chapter is to introduce and summarise the basic theory of MRI that will be used throughout the thesis.

In chapter 3, the BMD and biomechanical properties of the trabecular bone samples employed in this study are investigated in order to determine the gold standard values that the MRI derived data can be compared with. In addition, the preparation of the MRI experimental set-up is also presented in this chapter since it is strongly related to the reliability, accuracy and reproducibility of the MRI techniques.

In chapter 4, QMR investigations are presented and compared with the findings of other investigators in the field in an effort to obtain a better understanding of the value of the technique that will eventually confirm or reject its acclaimed potential. A set of 30 bone samples are investigated and the results are presented and discussed with respect to the ability of the technique to provide information relating to BMD and/or trabecular architecture and, eventually, bone strength. In addition, the findings are compared with respect to the information that can be obtainable with existing imaging modalities currently available in the clinical setting.

In chapter 5, MRM in-vitro investigations with the use of 30 bone samples are presented. The results are also related to the gold standard BMD and biomechanical properties of bone in an effort to assess the potential of this technique. In addition, the results from these investigations are compared with the results of other investigators in order to confirm or reject its acclaimed potential.

---

In chapter 6, a new method called SPENT is described, which is used to investigate the homogeneity of tissue. The resulting images have bright pixels in regions where the underlying magnetisation is non-uniform, and dark pixels in regions where the underlying magnetisation is uniform. This contrast, sensitive to sub-pixel structure is achieved through the application of an extra linear magnetic field gradient during a two dimensional fourier transform (i.e. 2DFT) pulse sequence, or, through filtering the acquired (time domain) signal. The aim of this chapter is to investigate the contrast produced in SPENT images and evaluate its potential for obtaining structural information not normally available from an object.

In Chapter 7, an integration of the findings is presented along with a summary of the thesis and its main conclusions are given with particular reference to the future development of the work presented here.

## **Chapter 2: “Basic Principles of Magnetic Resonance Imaging (MRI)”**

*“Since its introduction in the 70’s MRI has revolutionized medical imaging in general and has evolved into an indispensable component in the armament of imaging procedures” (Brown & Semelka, 1999, p. xi).*

In this chapter an outline of Magnetic Resonance Imaging principles are given. This subject matter is well established and has been summarised by, amongst others, Brown & Semelka (1999), McRobbie et al (2003), Rinck (2001), Hashemi & Bradley (1997), Haacke et al (1999), Cady (1990) and Gadian (1995).

### ***2.1 The development of MRI***

In 1946, Bloch (Bloch et al, 1946) and Purcell (Parcell et al, 1946), independently of each other, described a physico-chemical phenomenon that was based upon the magnetic properties of certain nuclei in the periodic system. These investigators found that when these nuclei were placed in a magnetic field, they absorbed energy in the radiofrequency range and re-emitted this energy during the transition to their original state. Because the strength of the magnetic field and the radiofrequency had to match each other, the phenomenon was called Nuclear Magnetic Resonance (NMR). These investigators received the Nobel Prize for Physics in 1952.

Over 25 years later, Lauterbur first used the principles of NMR to take an image (Lauterbur, 1973). Smaller magnetic fields with linear gradients were used to encode spins with a variation in frequency and phase that depended linearly on position. With the introduction of NMR to clinical imaging the word ‘nuclear’ was dropped by marketing groups and radiologists because it sounded like ‘nuclear warfare’ or ‘nuclear power plant’, with which NMR has nothing in common (Rinck, 2001). MRI was born thereafter and quickly progressed with the first in-vivo human image produced by a group in

---

Nottingham in 1976 led by Mansfield (Mansfield & Maudsley, 1976). Both Lauterbur and Mansfield received the Nobel Prize in 2003 for their contribution to the development of MRI.

Today, MRI influences decisions in most areas of medicine, from neurology to orthopaedics, from paediatrics to oncology. Because of its high soft tissue contrast, its lack of side effects and its three-dimensional capabilities, coupled with its increasing availability, more and more patients are now referred for MRI examinations.

## ***2.2 Simple spin physics***

Atoms consist of three fundamental particles: protons, which possess a positive charge, neutrons, which have no charge, and electrons, which have a negative charge. The nucleus of an atom consists of all the protons and neutrons while the electrons are located in shells or orbitals surrounding the nucleus. The characteristic properties of atoms depend on the number of each of these particles. The properties most commonly used are the atomic number, which is the number of protons in the nucleus and the atomic weight, which is the sum of the number of protons and neutrons. Atoms of the same atomic number but different atomic weights are called isotopes.

One of the properties of the nucleus is spin or intrinsic spin angular momentum, which refers to a constant rotation of the nucleus around an axis (the rotation is perpendicular to the axis) at a constant rate (see figure 2.1).

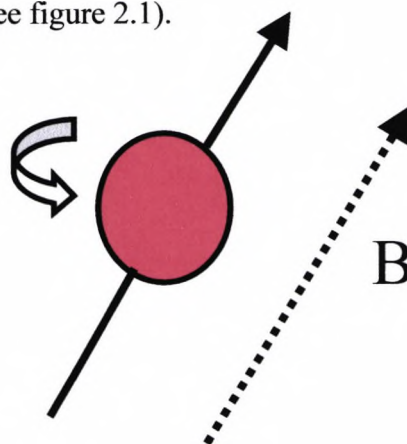


**Figure 2.1.** A rotating nucleus with a positive charge produces a magnetic field (B) oriented parallel to the axis of rotation.

---

The value of the nuclear spin ( $I$ ) depends on the precise atomic composition and is quantized to three groups of values: Firstly, nuclei with even numbers of atomic weight and atomic number and have  $I=0$ , no energy level splitting and no NMR signal. Secondly, atomic nuclei with even atomic weight and odd atomic number have  $I$ =integer and give short lived, more complex NMR signals. Lastly, nuclei with an odd atomic weight have  $I=1/2$ . Although most of the elements in the periodic table have at least one naturally occurring isotope and can be examined using MRI, only Hydrogen ( $^1\text{H}$ ) has been used routinely for medical imaging. Apart from being present in water, which constitutes 70% of the human body, hydrogen is present in body fat and other chemical compounds inside the human body. While recent advances have been made in imaging other nuclei (Foster & Hutchison, 1987), it is exclusively  $^1\text{H}$  MRI that is described here.

The hydrogen atom, with its one proton and  $I=1/2$ , has associated energy levels based on the spin quantum number  $I$ . Since the number of energy states of a nucleus is determined by the formula (Hashemi & Bradley, 1997):

$$\text{Number of energy states} = 2 I + 1, \quad (\text{eq. 2.1})$$

for a  $^1\text{H}$  with spin  $I=1/2$ , equation 2.1 gives,

$$\text{number of energy states} = 2 (1/2) + 1 = 2 \quad (\text{eq. 2.2})$$

Therefore, the hydrogen proton has two energy states denoted as  $-1/2$  and  $+1/2$ . This means that some hydrogen protons spin the opposite way and have a magnetic field in the opposite direction usually termed as 'parallel' or 'anti-parallel' states. If there were an even number of protons in the nucleus, then every proton would be paired (i.e. for every parallel proton there would be a paired anti-parallel proton) canceling each other out resulting in a net magnetic field of zero. When there is an odd number of protons, then there always exists one proton that is unpaired.

### 2.3. Production of the Net Magnetization

By considering an arbitrary volume of tissue containing protons located outside a magnetic field, each proton has a spin vector of equal magnitude and the spin vectors for the entire collection of protons are randomly oriented (see figure 2.2). The sum of all vectors produces a zero value, which means that no net magnetization is observed in the tissue.

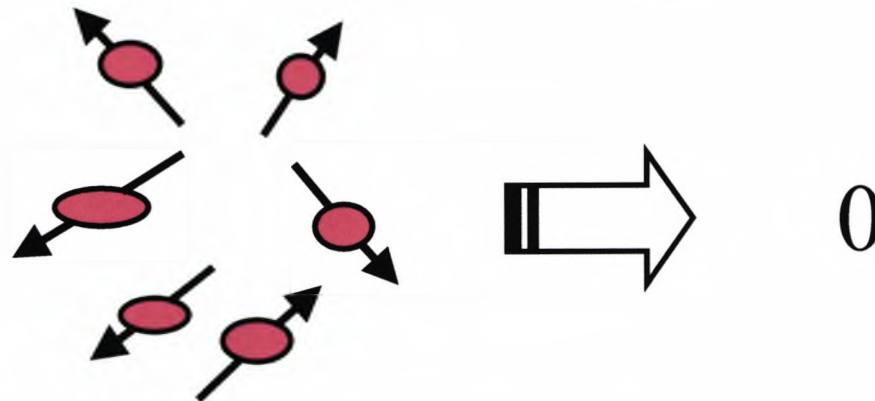


**Figure 2.2.** Random orientation of protons within a volume of tissue. The vector sum of these spin vectors is zero (Brown & Semelka, 1999, p. 4).

If the tissue is placed inside a magnetic field  $B_0$ , the protons will tend to align either parallel or anti-parallel to the direction of the main magnetic field containing different energy levels. The orientation of the protons parallel to  $B_0$  is of lower energy and its configuration contains more protons than the higher energy, anti-parallel orientation. This behavior is known as the Zeeman interaction and refers to a nonzero interaction or coupling between the protons and  $B_0$ . This coupling causes a difference in energy ( $\Delta E$ ) between the parallel and anti-parallel protons which is proportional to  $B_0$  (see figure 2.3).

The exact number of protons in each energy state is governed by a distribution known as the Boltzmann distribution and is determined from the equation:

$$N_{UPPER} / N_{LOWER} = e^{-\Delta E / kT} \quad (eq. 2.3)$$

where  $N_{UPPER}$  and  $N_{LOWER}$  are the number of protons in the upper and lower energy levels respectively,  $k$  is the Boltzmann constant ( $1.381 \times 10^{-23} \text{ J K}^{-1}$ ) and  $T$  the absolute temperature. By considering equation 2.3 it becomes clear that at equilibrium, the larger

the energy difference  $\Delta E$  becomes, the larger will be the population difference between the protons at the two energy levels. The energy difference between the two energy levels in the magnetic resonance experiment is proportional to the magnetic field strength. Thus, if the field strength  $B_0$  is increased, the energy difference is increased and hence the net magnetization is increased. This explains the increase in signal-to-noise ratio with increasing magnetic field strength.

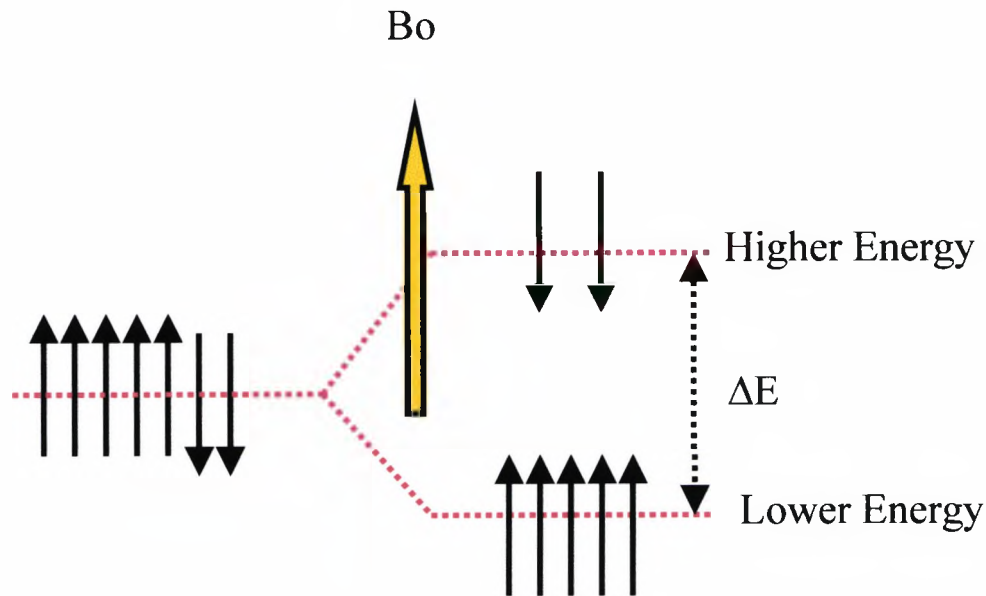


**Figure 2.3.** The Zeeman diagram.

The unequal number of protons in the two energy levels means that the vector sum of the protons will be non-zero and will point parallel to the direction of  $B_0$  since most of the protons are found in the lower energy state. This vector sum refers to the Net Magnetization ( $M$ ), which is the physical entity in MRI that is manipulated using radiofrequency ( $RF$ ) pulses and gradients in the magnetic field to produce an image.

In order to appreciate the behavior of the individual protons in the lower energy state that make up  $M$ , a microscopic and macroscopic description with the use of a Cartesian coordinate system is probably the best method. Figure 2.4 below demonstrates the

microscopic and macroscopic collection of protons in the presence of an external magnetic field.

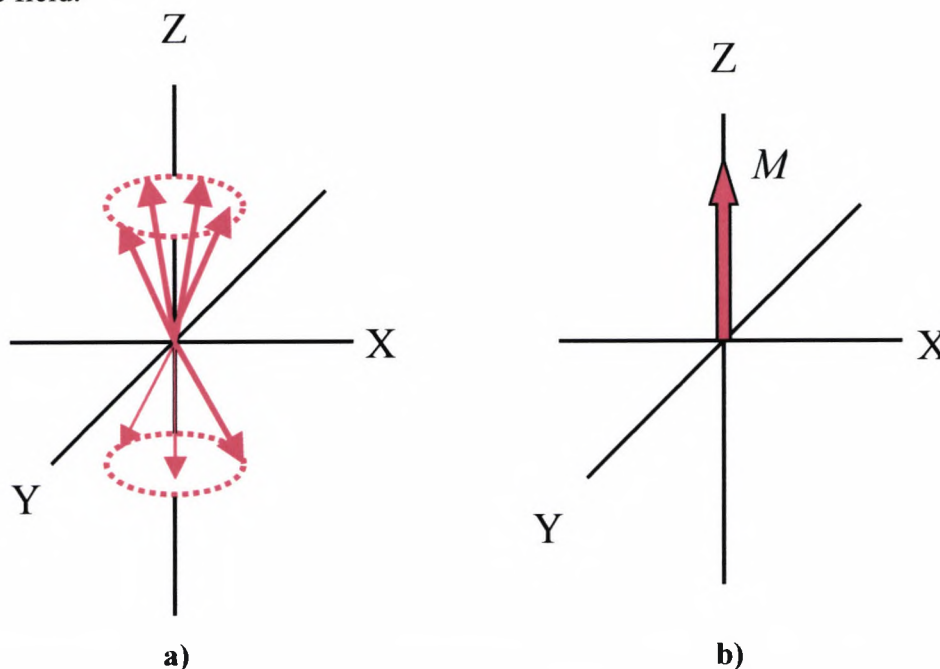


**Figure 2.4.** The representation of the net magnetization ( $M$ ) with the use of a Cartesian co-ordinate system. a) indicates the collection of protons in the two energy states and b) the corresponding net magnetization which is the sum of the vectors.

As previously mentioned, in order to obtain a good understanding of the behavior of protons when placed in an external magnetic field, a microscopic and macroscopic description is used. This is usually referred to as quantum and classical mechanics, respectively, and a brief definition of these terms is necessary for the sake of clarity. Quantum mechanics (QM) is a branch of physics which explains the behavior of very small particles such as protons and electrons, which sometimes act like particles and sometimes like waves. On the other hand, classical mechanics (CM) describe normal sized bodies and large numbers of small particles such that their quantum mechanical behavior is averaged out. Although the CM description is usually used (and will be used throughout in this chapter), in order to better understand how the protons behave when placed in an external magnetic field, QM will be briefly employed.

Despite their intrinsic spin angular momentum described earlier, in the presence of a magnetic field the protons appear to rotate, or precess, about the  $z$  axis of the main field

at a specific frequency called the Larmor frequency,  $\omega$ . In order to demonstrate this behavior, an individual proton from the lower energy state is considered in figure 2.5.

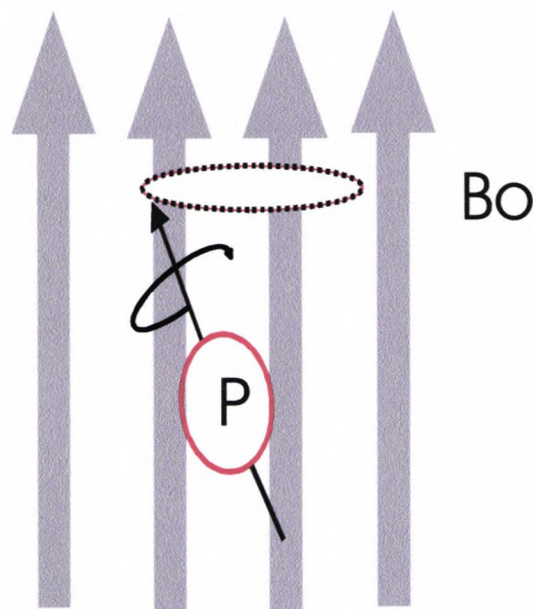


**Fig. 2.5** Precession of a proton (P) in the presence of an external magnetic field ( $B_0$ ).

The exact frequency of precession by such a nucleus can be calculated using the Larmor equation:

$$\omega = \gamma B_0 \quad (\text{eq. 2.4})$$

where,  $\omega$  is the frequency of precession (MHz),  $\gamma$  is the gyromagnetic ratio (MHz/T), and  $B_0$  is the strength of the external magnetic field (T). Equation 2.4 shows that there is a strictly linear relationship between the frequency of precession,  $\omega$ , and the strength of the external magnetic field,  $B_0$ .

If a Radio Frequency (RF) wave is transmitted at precisely the Larmor frequency and with an orientation perpendicular to  $M$ , the interaction between the protons and the RF pulse results in a rotation of  $M$  into the  $xy$  plane. Due to the existing precession of the net magnetization when parallel to  $B_0$ , the RF wave will tip  $M$  away from the  $z$  axis down

towards the  $xy$  plane in a 'spiral' fashion, but it will continue precessing about the  $xy$  plane (see figure 2.6).

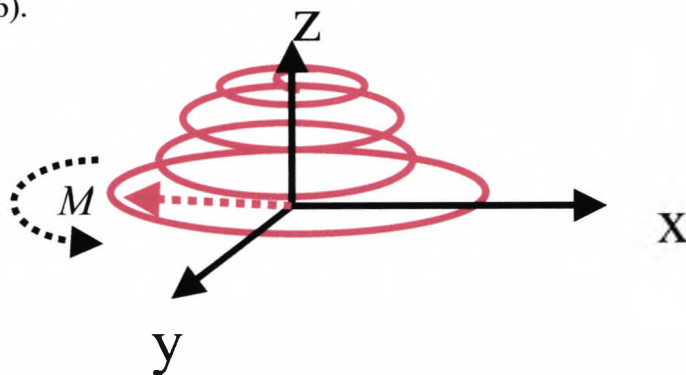


**Figure 2.6.** During the  $RF$  pulse  $M$  spirals away from the  $z$  axis down towards the transverse plane.

### 2.3.1 The rotating frame of reference

Before any attempt to further describe the effect of the  $RF$  pulse on a spin system, the rotating frame of reference has to be employed for more simplicity. Because the spins rotate around their own axis and precess around the axis of the magnetic field  $B_0$  at the Larmor frequency, the  $RF$  pulse will add another movement making the description very difficult.

For this reason the rotating frame of reference is often used which is taken to be rotating at the Larmor frequency and prevents complication from periodic motion. In this way, the 'spiral' Larmor precession frequency is removed and the flip of the net magnetisation can be demonstrated as a slow precession of the net magnetisation from the  $z$  axis into the  $xy$  plane as if it was moving in a simple arc (see figure 2.7).

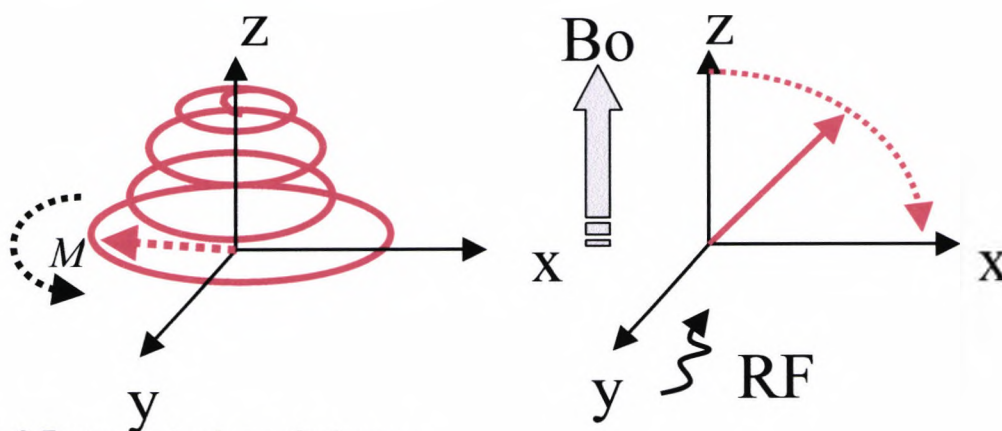


**Figure 2.7.** The rotating frame of reference.

### 2.3.2 RF pulses and the Free Induction Decay (FID)

If the RF energy is applied for a time such that the new orientation of the net magnetisation is at a 90-degree angle to the main magnetic field, the RF pulse or energy transmission is termed a 90-degree pulse. Similarly, if the orientation of the net magnetisation after the cessation of the RF pulse is anti-parallel to the main field, the RF pulse is termed a 180-degree pulse (see figure 2.8).

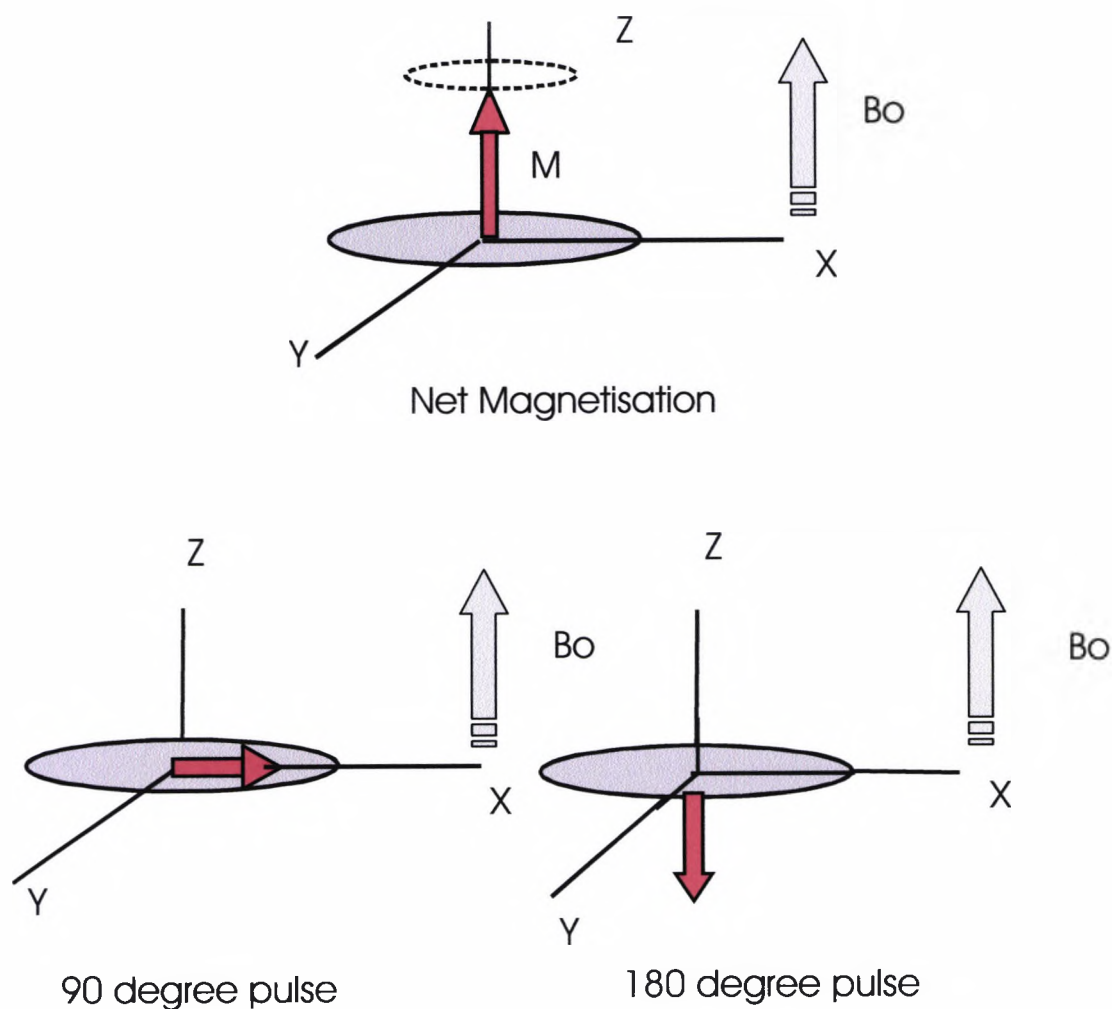


**Fig. 2.8.** The effect of 90 and 180 degree RF pulses on the net magnetisation  $M$ .

After the RF energy transmission ceases, the protons tend to relax and reorient themselves (i.e. back to the z axis). During this process they emit RF waves (i.e. free

induction decay, FID), and revert to their equilibrium position at characteristic rates termed relaxation rates. Figure 2.9 demonstrates the FID signal.

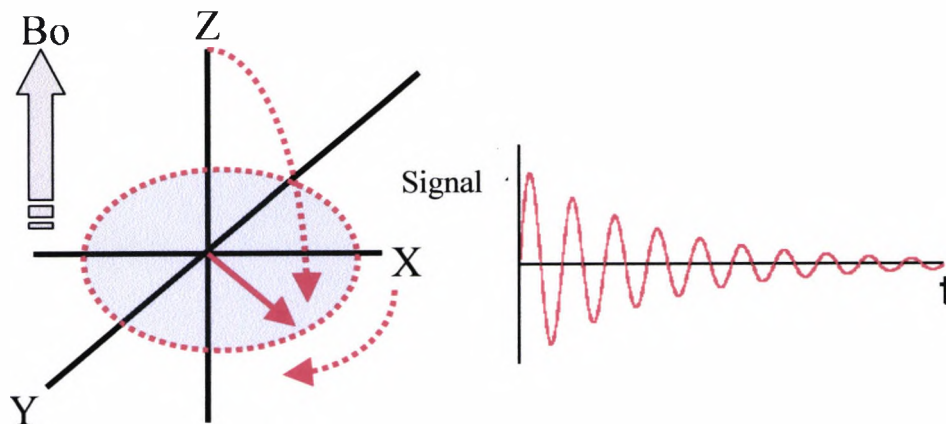


**Figure 2.9.** a) The precession of the net magnetization in the  $xy$  plane and b) the signal (FID) picked up by the  $RF$  coil.

The FID from a sample is picked up by the  $RF$  coil and the intensity of this process is a complex interaction of several intrinsic factors, including the density of the nuclei,  $N(H)$ , spin lattice relaxation ( $T1$ ) and spin-spin relaxation time ( $T2$ ), magnetic field inhomogeneity induced relaxation time ( $T2^*$ ), chemical shift and diffusion effects.

#### **2.4 Relaxation mechanisms**

As seen in previous sections, when  $M$  absorbs  $RF$  energy it is tipped into the  $xy$  plane. During relaxation, the protons release this energy in the form of an FID and return to their equilibrium position. However, the FID in MR imaging is much more complex than its description with the use of one proton. Relaxation times are measured for an entire sample and are statistical or average measurements. For example, relaxation times can be measured for gray matter or cerebrospinal fluid as bulk samples rather than for the individual water or fat molecules within the tissues. Two relaxation times can be measured, known as  $T1$  and  $T2$ . While both times measure the spontaneous energy transfer by an excited proton, they differ in the final deposition of the energy.

### 2.4.1 Spin Lattice Relaxation and its time constant $T1$

Spin-lattice Relaxation causes the magnetization  $M$  to return to its equilibrium position via the exchange of energy between spins and their surrounding molecular environment (or lattice). Spin-lattice or longitudinal relaxation  $T1$  is the time required for the  $z$  component of  $M$  (i.e.  $M_z$ ) to return to 63% of its original value following an excitation pulse (90-degree in this case). Molecular tumbling (i.e. vibration, rotation) produces small rapidly oscillating (around the Larmor frequency) variations in the size and direction of  $B_0$ . A magnetic moment in this oscillating  $B_0$  field will have transitions induced between spin states. Due to the bias in probability of transition between states towards a particular direction, the change in the population of states will on average return the magnetisation to its equilibrium state (see figure 2.10).

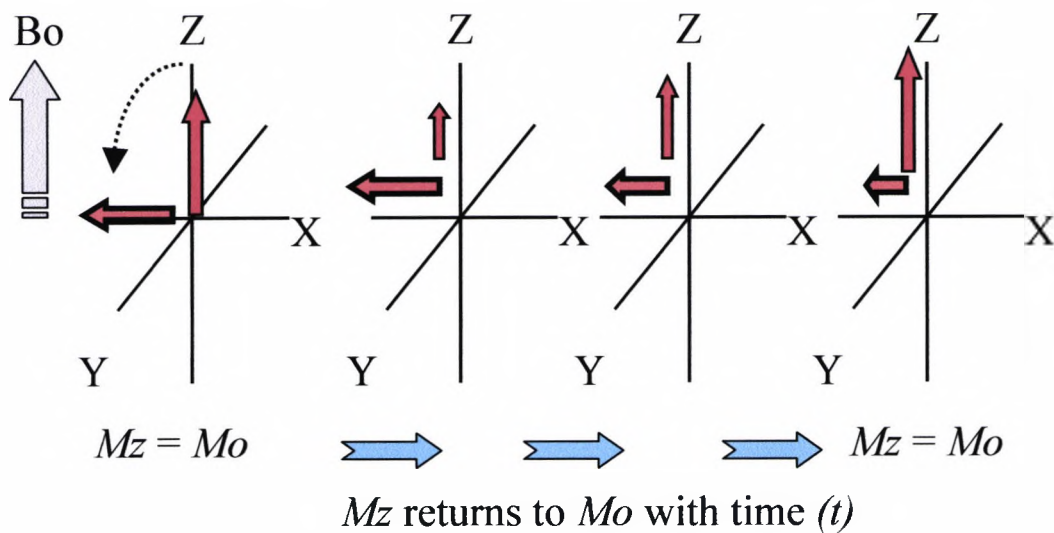


**Figure 2.10.** The return of longitudinal magnetization after a 90-degree RF pulse.

The return of magnetisation ( $M_z$ ) with time ( $t$ ) follows an exponential growth process, with  $T1$  being the time constant describing the rate of growth and is expressed mathematically below:

$$M_z(t) = M_0(1 - e^{-t/T1}) \quad (\text{eq. 2.5})$$

### 2.4.2 Spin-Spin Relaxation and its time constant $T_2$

The relaxation time  $T_2$  is the time required for the transverse component of  $M$  (i.e.  $M_{xy}$ ) to decay to 37% of its initial value via irreversible processes. After an  $RF$  pulse has been applied (i.e. 90-degree) there is coherent transverse magnetization  $M_{xy}$  (see figure 2.11). The coherence is gradually lost (dephased) as components of the transverse magnetization obtain different phase. This process causes the exchange of energy between spins (usually termed as spin-spin relaxation) rather than to the surrounding lattice (i.e. as in the case of  $T_1$ ) and results in a gradual loss of phase coherence.

The primary component in the loss of  $M_{xy}$  coherence in biological samples occurs through the exposure of spins to local, low frequency fluctuations in the magnetic field. This extra component of  $T_2$  relaxation ensures that  $T_2$  is always shorter or equal to  $T_1$ .

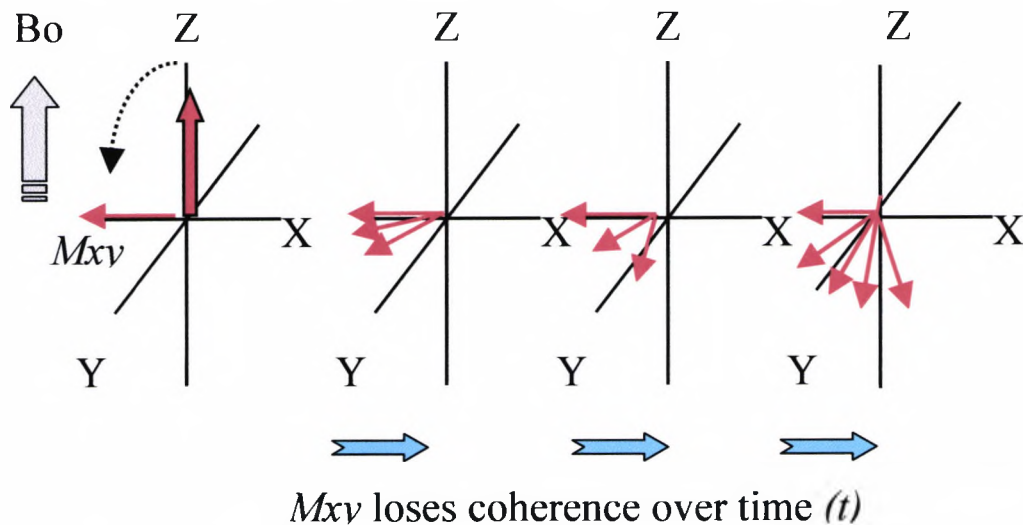


**Figure 2.11.** Loss of transverse magnetization after a 90-degree  $RF$  pulse.

The development of the net transverse magnetisation with time shows an exponential decay to zero:

$$\mathbf{M}_{xy}(t) = \mathbf{M}_{xy}(0) \cdot \exp\left(-\frac{t}{T_2}\right) \quad (\text{eq. 2.6})$$

Transverse magnetisation can also lose coherence through spatial variation in the main magnetic field  $B_0$ , causing a variation in spins' angular velocities. This non-uniformity in

---

$B_0$  may arise from a variety of sources which are sometimes categorized as external or intrinsic.

External sources refer to those outside the tissue being imaged and may be non-uniformity of  $B_0$  due to imperfections in magnet manufacturing, composition of nearby building walls or other sources of metal. Although every effort to maintain a homogeneous magnetic field prior to every MR imaging experiment is made, this homogeneity can be easily disturbed by external sources and shimming is usually applied to reduce this effect.

On the other hand, intrinsic sources refer to those originating within the tissue being imaged and may be related to differences in the magnetic susceptibility or degree of magnetic polarization of adjacent tissues (e.g. bone, marrow) which will distort the local magnetic field near the interface between the different tissues (this forms the basis of the work presented in chapter 4 and will be described in more detail in that chapter).

The sources of dephasing described above are reversible in MRI and are characterized by  $T_2'$ . The combination of  $T_2$  and  $T_2'$  is measured in MRI, and has its own relaxation parameter  $T_2^*$  and a decay described by equation 2.6 with the substitution of  $T_2^*$  for  $T_2$ . Although these sources of dephasing due to  $B_0$  inhomogeneities are usually unwanted, sometimes they can be very useful in providing additional information regarding various tissues in clinical imaging. This is usually achieved with the use of Gradient Echo imaging which will be described in subsequent sections.

In order to investigate how these sources of dephasing can be reversed, a sequence of events has to be considered.

Assume a 90-degree pulse that will flip  $M$  into the transverse plane. During a time ( $t$ ), proton dephasing will occur through  $T_2^*$  relaxation processes. This dephasing can be regarded as involving protons that dephase faster in the  $xy$  plane (i.e. moving faster) and protons that dephase slower (i.e. moving slower). The application of a 180-degree pulse

following the 90-degree pulse will cause the protons to reverse their phases relative to the resonant frequency (see figure 2.12). This means that the faster protons will lie behind the slower ones, but they will catch up.

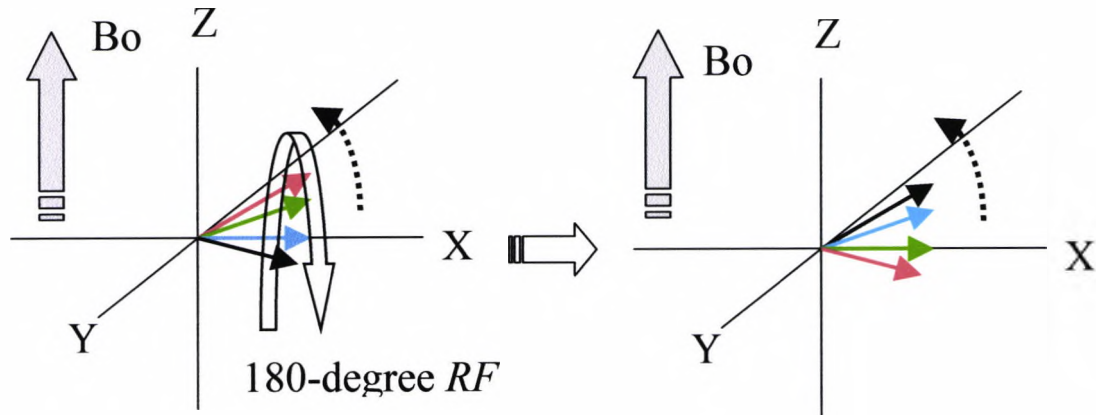


**Figure 2.12.** Reversal of proton dephasing due to  $T_2^*$  by the application of a 180-degree pulse. After the 90-degree pulse the magnetization  $M$  is tipped into the  $xy$  plane and begins to dephase shown on the left figure with the red arrow being a proton that dephases quicker and the black arrow, the slowest. The application of the 180-degree pulse will cause the faster protons to fold back as indicated on the right figure. However, the fast protons are still fast and will catch up with the slow ones.

Application of the 180-degree pulse causes the protons to reverse their phases. The rates and directions of precession for the protons do not change, only their relative phase. If time ( $t$ ) elapses again, then the protons will regain their transverse coherence. This reformation of phase coherence induces another signal in the receiver coil, known as Spin Echo. The application of more 180-degree pulses create more spin echoes with increased amount of  $T_2$  relaxation and signal loss. Figure 2.13 below demonstrates the effect of a series of  $RF$  pulses on the received signal.

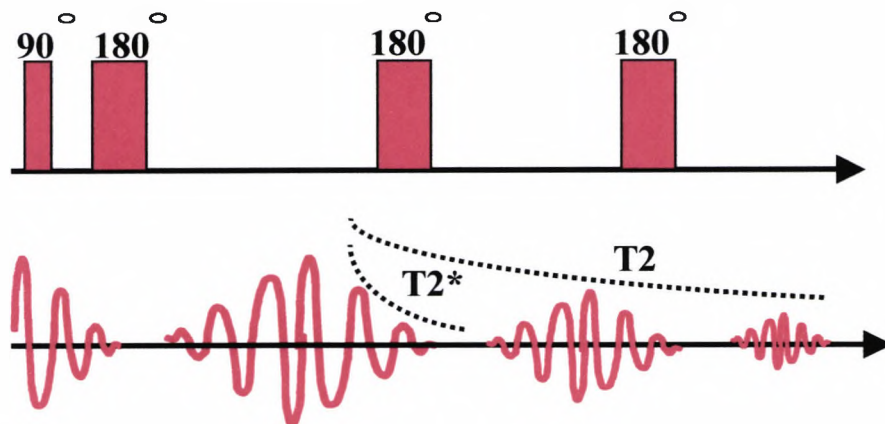


**Figure 2.13.** The effect on the signal from a series of  $RF$  pulses.  $T_2$  and  $T_2^*$  relaxation times.

---

## 2.5. Principles of Magnetic Resonance Imaging

In the previous sections, the relationship between the frequency of the  $RF$  energy that a proton absorbs and the magnetic field strength that it experiences was described. In addition, the relaxation mechanisms with which the protons return to equilibrium have also been described which involve the transmission of energy (weighted by the  $T1$  and  $T2$  relaxation times) in the form of an envelope of frequencies that is picked up by an  $RF$  coil. In order to localize these proton frequencies to different regions of space and form images in MRI, magnetic field gradients have to be employed. Three physical gradients are used, one in each of the  $x$ ,  $y$  and  $z$  directions which are usually referred to as readout or frequency encoding, phase encoding and slice selection, respectively.

The presence of magnetic field gradients can be described as an expanded version of the Larmor equation:

$$\omega_s = \gamma(B_0 + G l_s) \quad (eq. 2.7)$$

where  $\omega_s$  is the frequency of the proton at position  $l_s$  and  $G$  ( $\text{mT m}^{-1}$ ) is a vector representing the total gradient amplitude and direction. Equation 2.7 states that, in the presence of a gradient field, each proton will resonate at a unique frequency that depends on its exact position within the gradient field. The MR image is simply a frequency and phase map of the protons generated by unique magnetic fields at each point throughout the image. The picture element or pixel intensity is proportional to the number of protons contained within the volume element or voxel, weighted by the  $T1$  and  $T2$  relaxation times for the tissues within the voxel (Brown & Semelka, 1999).

### 2.5.1 Slice selection

The principle of slice selection is demonstrated in figure 2.14. A gradient ( $G_z$ ) is applied (in this case) in the  $z$  direction (marked in red in the middle figure). At the isocenter, the effect of the gradient is zero and the Larmor frequency applies. If an  $RF$  pulse containing a range of frequencies (bandwidth) about the Larmor frequency is applied, only that section of the object lying in the  $z$  direction will be excited (bottom figure).

Further away along the selection axis, either a higher or lower  $RF$  frequency will be needed for excitation. The slice thickness can be determined by the bandwidth of frequencies. However, typically, the  $RF$  pulse bandwidth is fixed and the slice thickness can be controlled by modifying the amplitude of the  $G_z$  gradient.

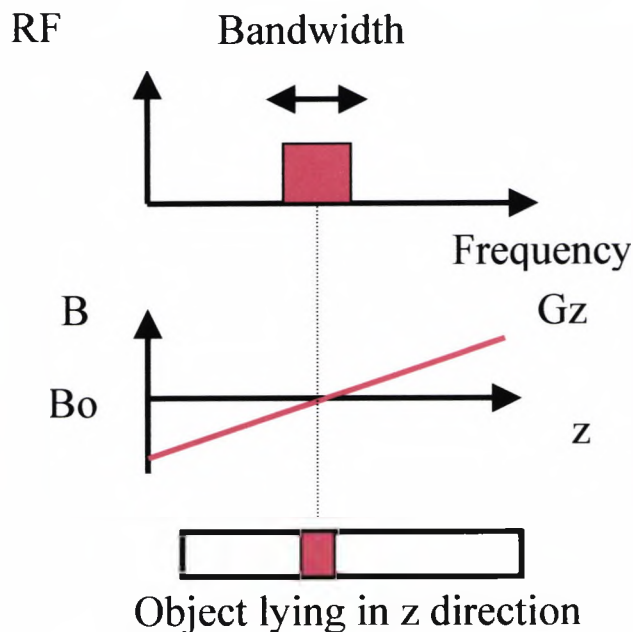


**Figure 2.14.** The principle of slice selection.

After a slice gradient has been applied the phase of the spins across its thickness become dispersed. This is because the transverse magnetization created during the  $RF$  pulse experiences the slice selective gradient that is applied and so spins precess at slightly different rates across the slice. Applying a gradient of opposite polarity, for the period that the transverse magnetization experienced the positive slice selective gradient, refocuses this dephasing.

### 2.5.2 Readout or frequency encoding

After selecting a slice from an object, information regarding individual pixels within this slice (i.e. the in-plane direction) is now needed. In the presence of a gradient known as readout gradient, information regarding one of the two dimensions of an image can be obtained. Assuming a slice of tissue with 9 voxels ( $3 \times 3$ ), the application of the readout

gradient in a direction perpendicular to the slice direction (e.g.  $x$  direction) will cause the protons to experience various levels of magnetic field depending on their position with respect to the readout gradient  $G_x$  (see figure 2.15). In this example, the center volume of the  $3 \times 3$  matrix will be unaffected by the  $G_x$  gradient. The column of the voxels to the right of midline will experience a higher magnetic field (and a change in frequency). The column of the voxels to the left will have a lower net magnetic field. Under the influence of this new gradient field, therefore, the protons begin to precess in accordance with equation 2.7. The magnitude of  $G_x$  and the frequency that is detected enable the corresponding position of the proton to be determined by Fourier Transformation (FT).

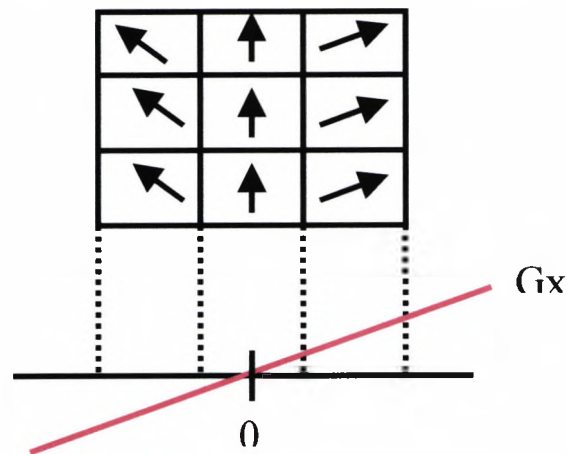


**Figure 2.15.** Frequency encoding gradient along the  $x$  axis. The arrows denote the position of precession (i.e. the phase) at a given point in time.

A gradient with half the area and opposite polarity is usually applied before the readout. This means that the spins will have phase coherence in the centre of the readout. Thus, the acquired signal will have maximum signal intensity in the centre of the readout and a full, symmetrical echo will be sampled.

### 2.5.3 Phase encoding

In a two-dimensional 2D FT technique, in addition to using the  $G_z$  gradient for slice selection and the  $G_x$  gradient for encoding in the  $x$  direction, a phase encoding gradient  $G_y$  is also applied, this time in the  $y$  direction. This gradient applies a linear phase shift to the magnetization in the phase encoding direction and is the only gradient that changes

amplitude during the data acquisition loop of a standard 2D imaging sequence (described in subsequent sections). The phase shift applied across the object is stepped according to the pre-selected number of pixels in this direction. Phase encoding is a similar process to frequency encoding (see figure 2.16).

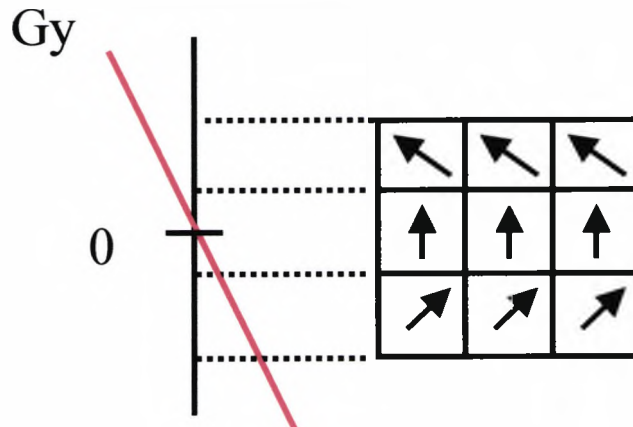


**Figure 2.16.** Phase encoding.

Typically, the phase encoding gradient is applied prior to the frequency encoding gradient and then switched off, returning the spins to their original frequency, but are ahead or behind in phase relative to their previous state. When the frequency encoding gradient is switched on the spins will now experience a change in their frequency (in addition to the change in phase from one  $G_y$  step). The same process is then repeated in an MR imaging experiment with a change in the amplitude of the  $G_y$  gradient determined by the pre-selected number of pixels in that direction.

Therefore, in simple terms, the MR image formation is obtained by repeating the slice excitation and signal detection multiple times, each with a different amplitude of  $G_y$ . This results in the protons in each voxel having a distinct frequency and phase at each  $G_y$  increment, which are unique and encode for the x and y co-ordinates.

#### 2.5.4 From raw data to image data

The previous section described how the MRI signals are localized in order to determine their position and characteristics within an object. However, these signals are complex

---

signals containing only frequency and phase information. In order to convert these signals into an image, several operations have to be performed. The digitized signals obtained from MRI experiments are initially stored as a complex data array with real and imaginary parts. Each detected signal for a given echo corresponds to a row and each row differs by the value of  $G_y$  applied prior to detection. The raw data matrix is thus a grid of data points with the readout direction displayed in the horizontal direction and the phase encoding direction displayed in the vertical direction. The raw data matrix is usually referred to as 'k-space' and all the data necessary to reconstruct an image is contained within it.

While each data point contributes to all aspects (frequency, phase, amplitude) of every location within the slice, some data points emphasize different features in the final image. The maximum signal content is located in the central portion of k-space (acquired with low amplitude  $G_y$ ) and provides the contrast in an image, while the outer portion (acquired with either high positive or high negative amplitude  $G_y$ ) provides edge definition to the resultant image (This forms the basis of the work presented in chapter 6)

The image data or display matrix is obtained via the 2D Fourier Transform from the raw data matrix. While the FT contains information regarding both the magnitude and phase of the measured signals, the normal image matrix contains only magnitude information. Although they must be the same dimension as the raw data matrix, image matrices are usually displayed as square images with readout as one direction and phase encoding as the other direction in the image.

## ***2.6 Pulse Sequences***

Pulse sequence diagrams are a simple means of showing how the *RF* pulses and gradients are applied in chronological order to map the raw data in k-space which will subsequently be FT'd to produce an MRI image. So far, the different steps of building an MRI image have been described individually. In this section, the anatomy of such a diagram is explained and the various common pulse sequences are described.

The discussion of MR pulse sequences below is pertinent in the context of using MR in the investigation of trabecular bone structure. For this reason, only the basic principles of two common MR pulse sequences (i.e. spin-echo and gradient echo) will be described and the adaptations required for these techniques when investigating trabecular bone structure, will be described in subsequent chapters.

### 2.6.1 The Spin-Echo (SE) MR pulse sequence

The basic components of a SE imaging sequence are shown in fig. 2.17 below. The SE sequence is composed of a series of selective 90-degree and 180-degree *RF* pulses repeated on an interval of *TR* (Repetition Time) seconds. The time between the first 90-degree pulse and the SE signal is referred to as *TE* (Echo Time). Both *TR* and *TE* are adjustable and provide the main means whereby image contrast can be manipulated.

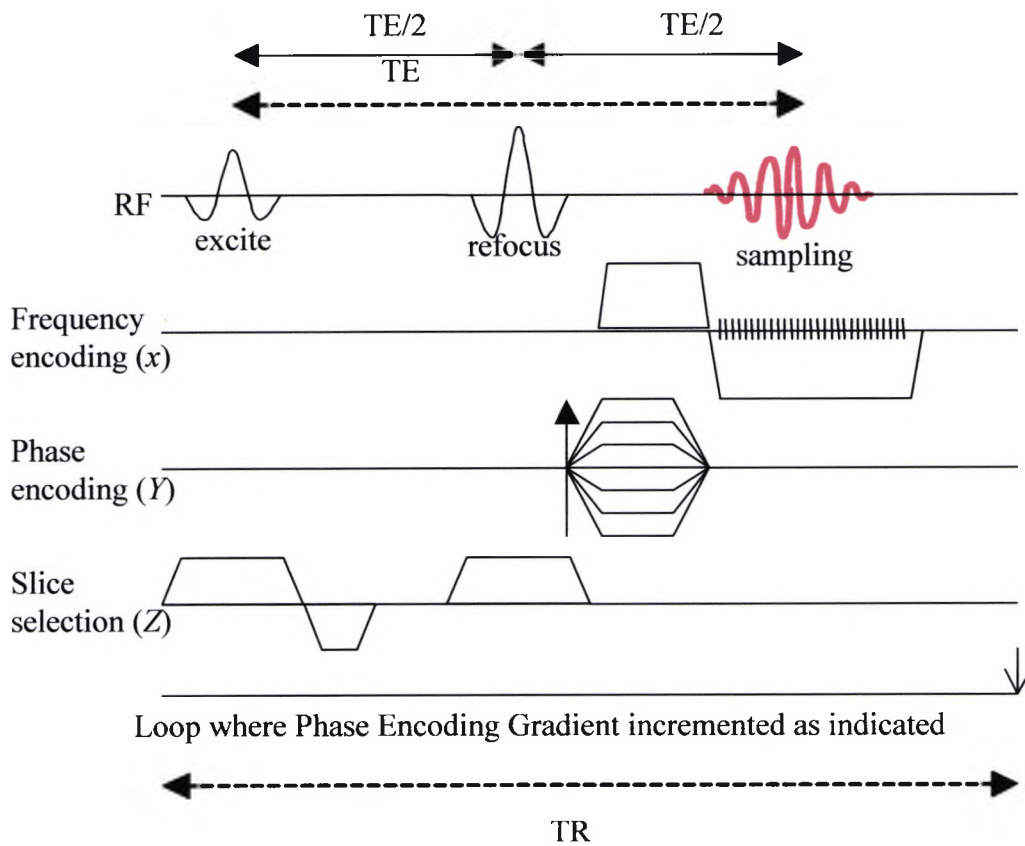


**Fig. 2.17.** General SE sequence.

The *RF* line on the diagram shows the application of a pulse to excite the spins in a slice (determined by the amplitude of the slice selection gradient for a given *RF* pulse) followed by a refocusing *RF* pulse. The refocusing pulse is positioned at time  $TE/2$  to reverse any phase evolution from constant local fields at the echo time. This is called a spin echo signal. In the 2DFT method one line of data is read out (in k-space) for each different phase encoding gradient. There is a time  $TR$  between the start of each phase encoding loop, this allows the longitudinal magnetization to recover before it is used again in the acquisition of next segment of data. The  $TR$  is thus typically of the order of  $T1$  to make sure a reasonable amount of the magnetization has relaxed and can then be used for the next excitation. The total scan time for the 2DFT is  $TR * nPE$  where  $nPE$  is the number of PE steps.

Assuming an ideal, rectangular slice profile and ignoring motion and diffusion effects, the signal from a voxel with tissue parameters,  $T1$ ,  $T2$ , and  $N(H)$  is given by:

$$S_{(SE)} = N(H) \left\{ 1 - 2 \exp\left(-\frac{TR - TE/2}{T1}\right) + \exp\left(-\frac{TR}{T1}\right) \right\} \cdot \exp\left(-\frac{TE}{T2}\right). \quad (eq. 2.8)$$

For the majority of imaging situations  $TR > TE$  so that the expression is approximated by:

$$S_{(SE)} = N(H) \left\{ 1 - \exp\left(-\frac{TR}{T1}\right) \right\} \cdot \exp\left(-\frac{TE}{T2}\right). \quad (eq. 2.9)$$

This shows that  $T1$  modulation of the signal is manipulated through the adjustable timing parameter  $TR$  while  $T2$  effects can be controlled through the parameter  $TE$ .

### 2.6.2 The Gradient-echo (GE) MR pulse sequence

GE sequences are a class of imaging techniques that do not use a 180-degree *RF* pulse to refocus the spins. The echo signal is generated only through gradient reversal and is known as a gradient echo.

The pulse sequence diagram of a GE pulse sequence is demonstrated on figure 2.18 below.

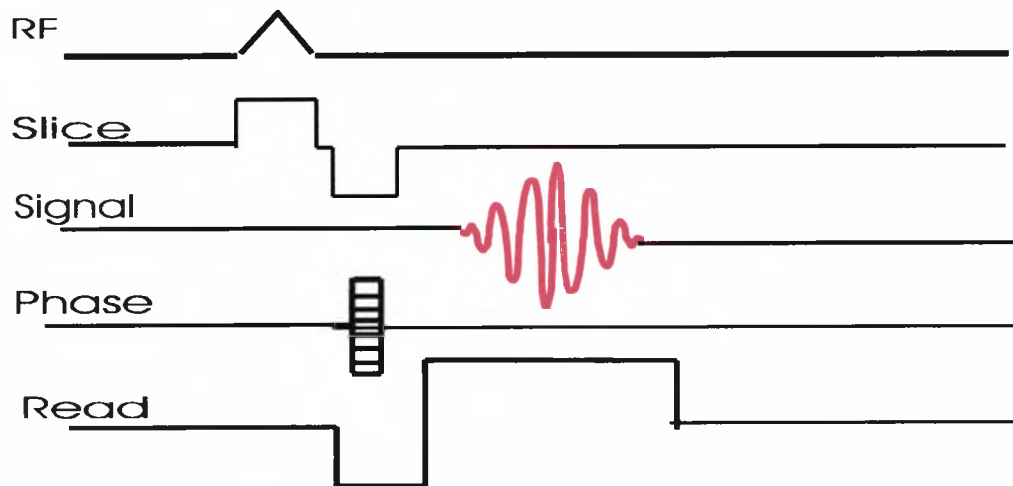


**Fig. 2.18.** General GE sequence.

The absence of the 180-degree *RF* pulse in GE sequences has several important consequences. Apart from lower *RF* power deposition to the patient, additional contrast mechanisms are also possible. The static sources for proton dephasing, the *B<sub>0</sub>* inhomogeneity and the magnetic susceptibility differences, contribute to the signal decay, so *TE* determines the amount of *T<sub>2</sub>\** weighting in a GE sequence rather than *T<sub>2</sub>* as in a SE image.

In single-slice GE images where spoiling gradients are applied before each excitation pulse, for a 90-degree flip angle and *TR* times that are long compared to *T<sub>2</sub>*, the transverse magnetization prior to each excitation pulse may be assumed to be dephased and the signal intensity may be written as:

$$I(TE) = I_0 e^{-TE/T_2^*} \quad (\text{eq. 2.10})$$

Where, *I<sub>0</sub>* depends on proton density. *T<sub>2</sub>\** can be defined as:

$$1/T_2^* = 1/T_2 + 1/T_2' \quad (\text{eq. 2.11})$$

---

where,  $1/T2^*$  is the observed decay rate as a function of  $TE$ ,  $1/T2$  is the intrinsic spin-spin effects, and  $1/T2'$  the dephasing time due to the main field inhomogeneity and also due to magnetic susceptibility differences.

### ***2.7 Safety issues in MRI***

Unlike x-ray based imaging techniques, MRI is considered to be a safe alternative in clinical decision making. However, even in MRI, several important safety parameters have to be taken into consideration.

#### **2.7.1 Static field effects**

A review of the literature reveals a variety of comments over the limits of magnetic field strength the body can be subjected to. Although the use of magnetic field strengths in the order of 1-2 Tesla have been safely used in the clinical setting over the last 25 years, higher magnetic field strengths are desirable in order to expand the applications of MRI. As seen in previous sections, the higher the magnetic field strength the more the potential MRI signal can be and a higher signal to noise can be achieved. However, the introduction of higher magnetic field strengths in the clinical setting may reveal unwanted effects in the human body that have not been encountered at lower magnetic field strengths.

Animal studies with the use of a variety of magnetic field strengths have shown no real effect on numbers of offspring, growth rates, feeding patterns or blood and urine biochemistry (McRobbie et al, 2003). In addition, epidemiological studies on female magnet workers have shown no deleterious effects on fertility, pregnancies or children. A cautious approach should nevertheless be adopted for both patients and staff who are pregnant.

Static fields also pose hazards through the displacement of ferro-magnetic implants (clips, coils, stents and especially cardiac pacemakers). The field can exert both a translational force and a torque on these magnetic objects. Most accidents reported are related to these implants.

---

### 2.7.2 RF effects

In addition to magnetic field issues, when an RF field interacts with tissue in the body energy is absorbed and heating can be developed. Thus, another important limit on an acquisition is the Specific Absorption Rate (SAR), which is defined as the total power in watts (W) per kilogram of tissue. This is a measure of the energy deposited in tissue and is governed by the likely temperature changes induced from this exposure. Therefore, the most important considerations prior to the application of an MRI technique are the overall energy deposition and, secondly, the distribution of this deposition (Shellock et al, 1986). Particular care must be taken over structures that receive a lot of RF power but which do not have mechanisms for redistributing the heat such as high levels of perfusion.

### 2.7.3 Gradient effects

The switching of the gradients induces electrical currents in conducting tissues according to Faraday's law. In modern MRI experiments, the rapidly changing magnetic field associated with the switching of the magnetic field gradients is able to generate currents in tissue, which may exceed the nerve depolarization threshold and cause peripheral nerve stimulation. Similarly, the possibility also exists that cardiac muscle can be stimulated which may be hazardous. However, extremely high exposure levels are needed for this, typically as high as 80 times the peripheral nerve stimulation threshold (McRobbie et al , 2003).

---

**Chapter 3: “*Investigation of the Physical and Biomechanical Properties of Bone and the Preparation of the MRI Experimental Set-up*”**

The main aim of the project was to investigate the value of MRI in the characterization of trabecular bone in an effort to determine whether MRI has a role in the early detection of Osteoporosis. Since MRI is not currently used in the clinical setting for such investigations, it was decided that the value of MRI would be investigated in-vitro with the use of human bone samples. An ongoing collaboration between the Radiation Laboratory at City University (Department of Radiography) and two London Hospitals (Whipps Cross Hospital & St Mary’s Hospital) had already been active prior to the start of this project. Femoral head samples from total hip replacement (THR) operations were readily available and kindly donated by the Orthopaedic Departments of these Hospitals on a regular basis.

An MRI research center was also required for the conduction of this project. A collaboration between the Radiation Physics Laboratory at City University (Department of Radiography) and the Department of Medical Physics and Bioengineering at University College London (UCL) resulted in regular access to the Bloomsbury Magnetic Resonance center (Welcome Trust).

In order to investigate the value of MRI in the characterization of trabecular bone, the physical and biomechanical properties of bone had to be investigated and compared with the MRI derived data. These parameters included the physical calculation of BMD (gold standard), the estimation of BMD using DEXA scanning, and the identification of a bone strength indicator (i.e. the Young’s Modulus, YM).

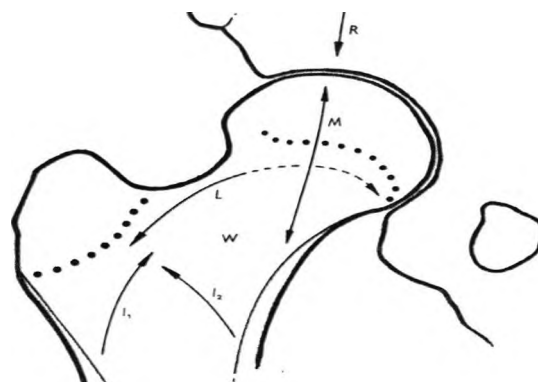
Access to a DEXA scanner was kindly made available by Dr. Ian Cullum at the Middlesex Hospital in London. A stress test machine for the determination of YM was available in the Engineering Department at City University.

### ***3.1 Preparation of the trabecular bone samples***

The preparation of the trabecular bone samples is based on a previously developed technique (Allday, 2004). The bone samples that are used here are 15 mm sided cubes cut from a radiographically predetermined location from within excised human femoral heads. The reason for the selection of this particular region from within the skeleton will be discussed.

Bones which predominantly consist of trabecular structures are generally the preferred measuring sites for the assessment of mineral density. This preference is based on the fact that trabecular bone responds about 3 to 4 times more than cortical bone (Pacifci and Avioli, 1993) and changes are first detectable in these regions (Grampp et al, 1999). In general, it has been shown that for bones with larger trabecular regions like the neck of femur, vertebral bodies and distal radius, the incidence of fractures is much greater (Majumdar, 1998).

In the head of femur, trabeculae can be classified into four main groups according to stress distributions (see figure 3.1).



(Whitehouse & Dyson, 1974, p. 422)

**Figure 3.1.** Approximation of the trabecular stress groups in the head of femur.

---

The medial group, M, originates from the strong cortical bone of the upper part of the shaft and extends in a gentle curve to the articular surface of the head. The lateral group, L, lies below the greater trochanter and the upper surface of the neck, and two further groups, *I1* and *I2*, which extend from the lateral and medial cortical bone and form the intertrochanteric arches. The area W in figure 3.1 represents the Ward's triangle which contains fewer trabeculae than neighbouring areas, particularly in the elderly population (Whitehouse & Dyson, 1974), and R represents the approximate direction of the main thrust (stress) from the acetabulum towards the femoral shaft in the standing position.

Figure 3.2 shows the location from where the bone cubes are cut with respect to the trabecular stress systems described above. The bone cubes are cut using an Isomet 1000 precision circular saw with a diamond cutting blade. Prior to cutting, each femoral head is radiographed in two projections (90 degree to each other) in order to provide the reference images for accurate positioning.

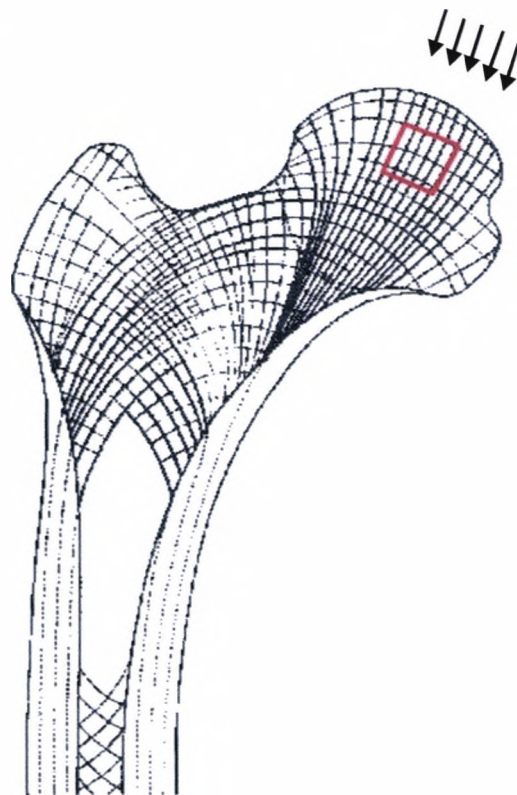


**Figure 3.2.** The exact location (square marked in red) from where the bone cubes are cut with respect to the trabecular stress systems and the forces applied (arrows).

---

Although every effort was made to cut the bone cubes with equal 15 mm dimensions in all three planes, it was noted that some bone cubes were characterized by slight variations. However, these slight variations were accounted for in all experiments which will be discussed in subsequent sections of this chapter.

Once cut, bone marrow lipids must be removed from the samples and replaced by water in order to study with MRI. Bone tissue by itself yields no signal because of the absence of mobile hydrogen protons and therefore, the trabecular spaces have to be occupied by a signal producing substance (water was chosen in this case but saline or other substances may also be used). Despite the fact that marrow can also offer high signal in MRI, this was not feasible in this case since, during the cutting process, yellow marrow (especially from the surfaces of the cube) is likely to escape and be replaced by air that can cause artifacts on the resultant data. In addition, there is evidence to suggest that the interaction of oxygen with yellow marrow on the surface of the bone cube may cause a change in the chemical composition of the marrow, and hence, affect the collection of uniform signal from the entire volume of the bone cube (Chung et al, 1993).

Thorough defatting is therefore important but with care not to damage the trabeculae. At this point it should be mentioned that the size of the bone cubes was determined with the defatting process in mind. As cube size increases, they become harder to clean since greater penetration of the cleaning solution is required. Many methods have been described in order to achieve this and include washing marrow out with a jet of cold water (Whitehouse & Dyson, 1974), cycles of submerging in detergent and evaporation (Majumdar et al, 1998), cycles of ethanol and water irrigation (Jiang et al, 1998). The defatting method chosen for this study involved a temperature controlled ultrasonic bath in conjunction with Alconox Terg-a-Zyme, an enzyme based detergent which works at its greatest efficiency at 40<sup>o</sup>C. The ultrasonic agitation generated by the ultrasound induced a more even distribution of the solution throughout the sample.

Each sample must be verified as clean using a standard qualitative biochemical test. The bone samples are agitated in ethanol using an ultrasound bath to ensure complete

---

penetration. The liquid is filtered off and poured into water. A cloudy appearance indicates the presence of lipid (it precipitates from the ethanol) whereas a clear liquid indicates that no lipid is present and hence, successful defatting. In general, complete defatting can be achieved within 30-100 hours depending on BMD and trabecular spacing variability between samples.

Once cleaned, samples have to be immersed in water for subsequent MRI experiments. However, by immersing the bone cubes into water, tiny air bubbles are likely to remain within the trabecular structure (i.e. because of surface tensions) and can cause artifacts in the resultant images (i.e. susceptibility artifacts). In order to account for this effect, the samples are placed in small beakers of water individually and degassed using a vacuum pump (Edwards No 5, High Vacuum International, U.K) which forces the air bubbles out of the sample. The effectiveness of the degassing process can be easily verified by a visual inspection of the high resolution MR images of the samples since air bubbles are easily observed. In the event of presence of air bubbles, the sample is placed back in the vacuum pump for additional time and re-assessed in the same way until all air bubbles have been removed. In general, it has been found that, on average, a sample can be effectively degassed within 45-60 minutes.

Despite the fact that samples from other locations within the skeleton could be equally (or even more) important to study in the same manner (e.g. spine, distal radius), limited sample availability confined the sample selection to femoral heads as hip replacement operations are very common. Currently there are more than 300 femoral head samples available. Due to the time consuming process of cutting, defatting, and degassing of the bone samples and with the limited access to the MRI scanner (over the three year period), it was decided that a total number of 30 samples would be employed.

### *3.2 Bone mineral density (BMD) measurements*

One of the most important parameters that is related to the strength of bone is BMD. Although BMD is not the only determinant of bone strength (as it will be shown in

---

subsequent sections and chapters), this is the only parameter that is currently assessed in the clinical setting for the characterization of Osteoporosis.

As shown in chapter 1, there are many imaging modalities that can be used to obtain an estimation of BMD. However, all these techniques are characterized with a certain degree of inaccuracy making the determination of the true BMD a difficult task. In the case of the bone samples that were used in this study, the true BMD could easily be calculated based on physical measurements. The method used for the calculation of the true BMD values for all 30 samples is presented in the following section.

### 3.2.1 Method

Density,  $\rho$  (i.e.  $\text{g/cm}^3$ ), can be calculated from the mass and volume of each sample from  $\rho=m/v$ , where  $m$  is the mass of the sample and  $v$  the volume of the sample. Prior to the measurements, the samples were thoroughly dried and the mass was then determined by obtaining the weight of the samples using a sensitive scale (minimum detectable limit of 0.01 g) and the volume was calculated by multiplying the length of the three sides of each sample. Although every effort was made during the cutting process of the bone cubes to achieve equal 15 mm dimensions in all three planes, it was later noted that some of the bone cubes were characterized by slight variations. Therefore, the calculation of the volume of each sample had to be performed manually with the use of a micrometer. However, since the calculation of the BMD in this way is somewhat operator dependant (i.e. the use of the micrometer to measure the dimensions of the sample), it was decided that the reproducibility of these calculations had to be tested. The possibility of errors entering due to inaccurate mass calculations was ruled out since the scale used gave consistent results.

### 3.2.2 Reproducibility assessment

A reproducibility assessment was carried out by using one of the 30 samples and repeating measurements on 10 separate occasions. The percentage of errors (i.e.

---

coefficient of variance - %CV) could be calculated from  $\frac{SD \times 100}{mean}$  where *SD* is the standard deviation and the mean is the average value of the 10 measurements.

The results of the reproducibility assessment revealed an error of only 0.59% (0.0033 SD), which was taken to be acceptable. It should be noted here that the ideal way to calculate the precision error of the technique would be to carry out repeated measurements on all 30 samples so that the percentage of error could be calculated pertaining to each sample individually. However, it was decided that the method used would still give an indication of the extent of errors which could be assigned to the rest of the samples. Besides, repeated measurements for all samples and with all techniques (especially MRI) would require considerable amount of experimental time, which would extend beyond the limited period of time available for this study.

### ***3.3 DEXA experimental measurements***

DEXA is currently the method of choice for the estimation of BMD in the clinical setting. Although many studies in the past have provided a thorough understanding of its accuracy for the determination of BMD (Genant et al, 1996), it was decided that this technique should be tested independently. The reason for this choice was the fact that many studies in the past have been conducting experiments with the use of volunteers or samples that had a great degree of variation with respect to the samples employed in this particular study. In order to be able to perform a true comparison between DEXA and the gold standard biomechanical properties of bone in this particular case, experiments had to be carried out with the use of the same bone samples.

#### **3.3.1 Method**

BMD measurements on the 30 samples were obtained using a DEXA machine (Hologic QDR-4500A) equipped with sub-region analysis software. The samples were scanned in groups of five as this was possible within the field of view (FOV) of the scanner and would be time saving. The sub-region analysis software enables the manual position of a

---

region of interest (ROI) on the samples from which the areal BMD (i.e.  $\text{g}/\text{cm}^2$ ) reading can be obtained (see figure 3.3).

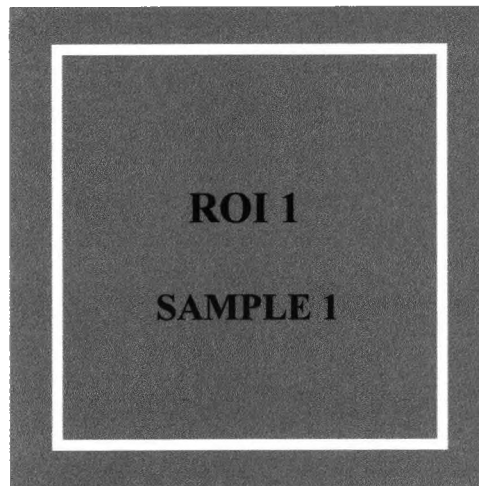


**Figure 3.3.** DEXA scanning principle. The shaded area represents one bone sample and the white square represents the ROI that is manually positioned on the sample's scout image so that a BMD reading can be made.

### 3.3.2 Reproducibility assessment

Initially, one sample was scanned for the reproducibility assessment of this technique. It was hypothesized that only one source of error was likely to exist in this particular investigation, this being the operator dependency. The possibility of errors entering at the time of data acquisition was excluded since possible contamination of the DEXA reading originating from cortical bone and soft tissue (i.e. muscle) or even obesity usually found in-vivo investigations, are inapplicable in this particular case. In this study, these effects would not be an issue of concern since the samples were purely made of trabecular bone. One bone sample was, therefore, scanned 10 times by positioning the ROI independently each time. Although the ROI had identical dimensions, it was hypothesized that if the ROI was not positioned by the operator at exactly the same position within the sample each time, this would act as a source of error. The %CV could be calculated from  $\frac{SD \times 100}{mean}$  where *SD* is the standard deviation and the mean is the average value of the measurements.

The results from the reproducibility assessment revealed an error of only 0.68% (0.0038 SD), which was taken to be acceptable. Since errors entering at the time of data acquisition were deemed inapplicable in this particular case, it was decided that the percentage identified from the reproducibility assessment with the use of one sample could be assigned to the rest of the samples without having to carry out repeated measurements on all samples individually.

### **3.4 Mechanical testing**

The identification of a bone strength indicator, like the Young's Modulus (YM) was also required for this study. The idea was to determine the YM of the bone samples in an effort to understand whether there was a relationship between this and other properties of bone. Most importantly, the results of these investigations could be compared with the MRI derived data.

#### **3.4.1 Method**

Mechanical tests were performed on the 30 bone samples with the use of a mechanically actuated test machine (Lloyds M30K, UK) by loading one sample at a time. While a sample is being loaded, a load-displacement curve is recorded (see figure. 3.4).

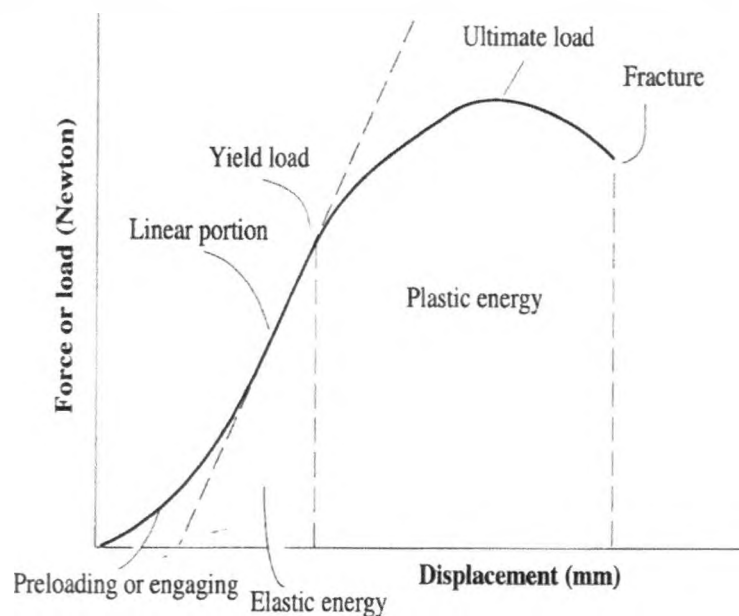


**Figure 3.4.** A typical load-displacement curve (An & Draughn, 2000, p.26).

Each sample was loaded with a gradually increasing force of 0-500 N in the superior-inferior direction so that trabeculae were running parallel to the applied force, as in the case of the real forces applied in the head of femur (see fig. 3.2), and displacement was recorded by the motion application system (in mm).

Load-displacement curves are particularly useful for measuring the strength and stiffness of whole structures but in order to compare behaviour of different materials, stress-strain curves are needed for standardization which can be obtained by converting the load-displacement curves and taking into account the dimensions of the object (An & Draughn, 2000). Assuming a three-dimensional model of the trabecular bone cube (see figure 3.5), stress ( $\sigma$ ) can be calculated by the magnitude of force (N) divided by the surface area ( $B \times C$ ) over which the force acts.

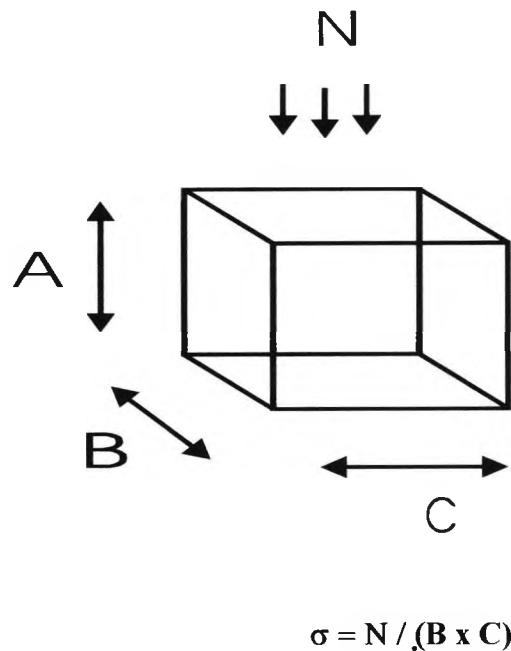


**Figure 3.5.** A three dimensional model of the trabecular bone cube.

Alternatively (see figure 3.6), strain ( $\epsilon$ ) is a dimensionless measure since it is the ratio of two quantities (both in units of length) and can be defined as deformation ( $\Delta L$ ) per unit length ( $L$ ).

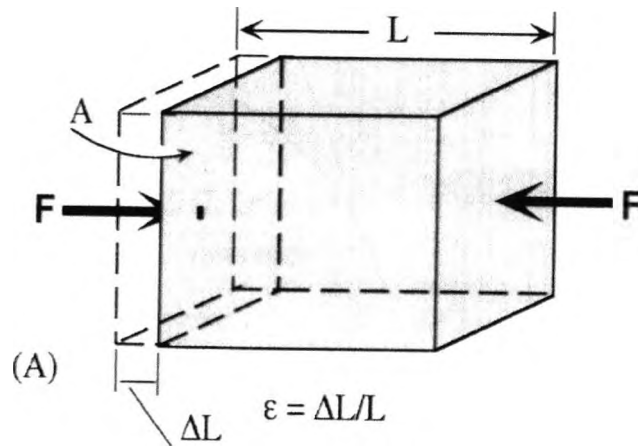


**Figure 3.6.** Demonstration of strain (An & Draughn, 2000, p. 27).

The stress-strain curves for each sample were therefore obtained by carefully measuring the dimensions of each cube and following the above conversion procedure (see figure 3.7).

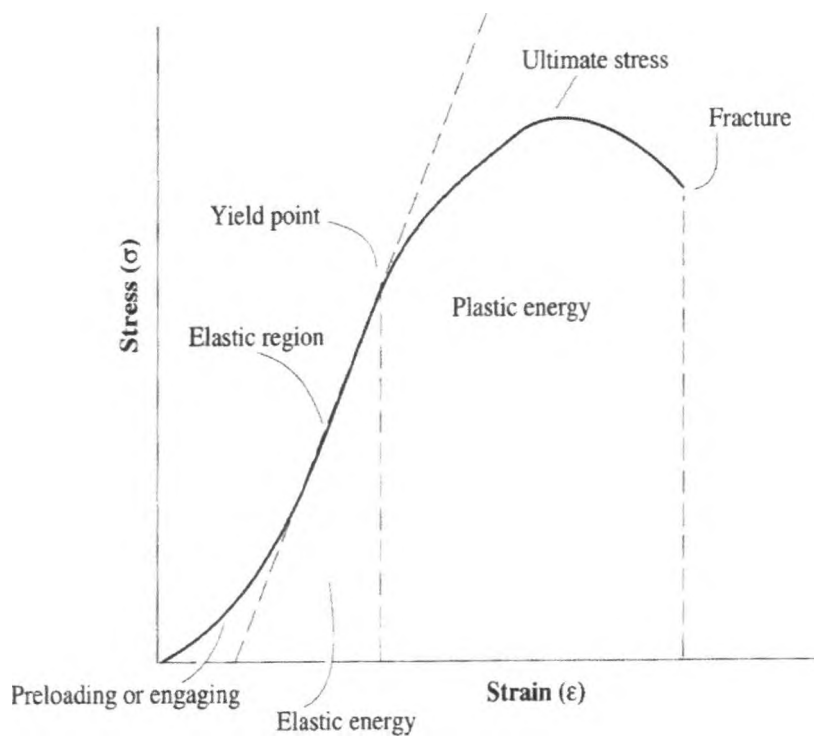


**Figure 3.7.** A typical stress-strain curve (An & Draughn, 2000, p. 28).

---

The slope of the “elastic region” from the resultant stress-strain curve is the modulus of elasticity or Young’s modulus (YM), which was calculated from the stress-strain curves for each sample.

#### 3.4.2 Reproducibility assessment

One again, a reproducibility assessment for this technique was deemed necessary and was carried out with the use of one bone sample. In this case it was hypothesized again that errors were likely to enter due to inconsistency in the operator’s performance. During pilot studies with the use of the stress machine, it was noted that if the object was not positioned at exactly the same place for each repeated measurement (in the center of the parallel actuated plates), the calculations of YM were inconsistent. The circular plates of the machine were, therefore, carefully measured and the center point was determined. A square shape with dimensions equivalent to the bone samples’ dimensions (i.e. 15 mm) was later marked on the plates to provide means for accurate positioning. One bone sample was tested 10 times (i.e. YM calculation) by repositioning the sample each time.

The results from the reproducibility assessment revealed an error of 4.1% (2.281 SD), which was calculated from  $\frac{SD \times 100}{mean}$ . This error was attributed to minute variations of sample positioning on each separate occasion which could be picked up by the highly sensitive recording mechanism of the mechanically actuated test machine. However, part of the error identified can be attributed to minute changes in the trabecular structure (i.e. fractures of tiny trabecular plates) between measurements, which may have accounted for a small variation of YM.

#### ***3.5. The relationships between the physical and biomechanical properties of bone***

In order to determine the relationships between the physical and biomechanical properties of the bone samples that were used in this study, the results from the physical calculations of BMD, DEXA scanning and stress tests were all compared.

### 3.5.1 DEXA (BMD) Vs calculated BMD

In order to determine the accuracy of DEXA for the estimation of BMD in these particular samples, the DEXA results were compared with the BMD obtained from the physical calculations. Figure 3.8 below shows this relationship.

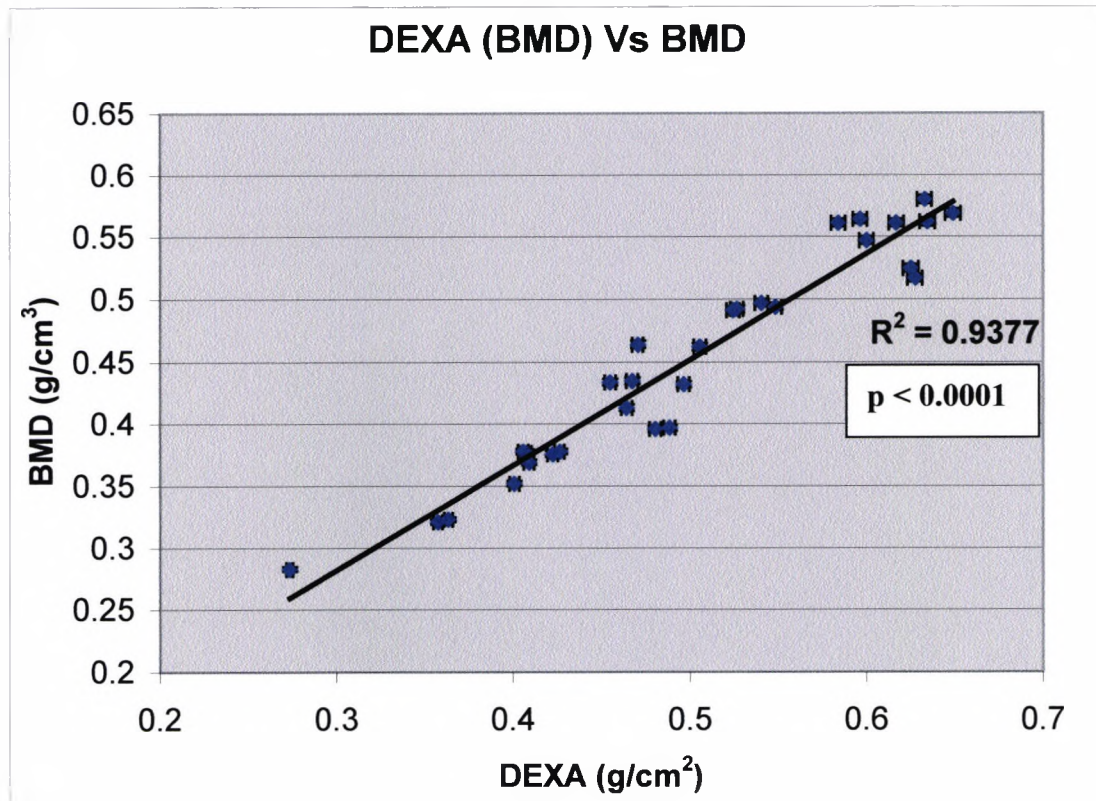


**Figure 3.8.** Relationship between DEXA (BMD) and BMD from physical calculations (gold standard). Error bars for each technique are represented as two standard deviations.

From figure 3.8 it can be seen that a very strong correlation exists between BMD estimated with DEXA and BMD derived from physical calculations. This result indicated that DEXA was particularly accurate in the estimation of BMD in these samples. However, as mentioned elsewhere, the samples used in this study were cut only from sections of trabecular bone and therefore, no contamination of the results from cortical bone and other tissue was present. Studies with the use of volunteers have shown that the accuracy of DEXA in the estimation of BMD is much less than that observed in this particular case.

### 3.5.2 YM Vs BMD

In order to investigate the relationship between BMD and bone strength, the BMD values derived from physical calculations on all 30 samples were compared with the YM values derived from the stress tests. Figure 3.9 below shows this relationship.

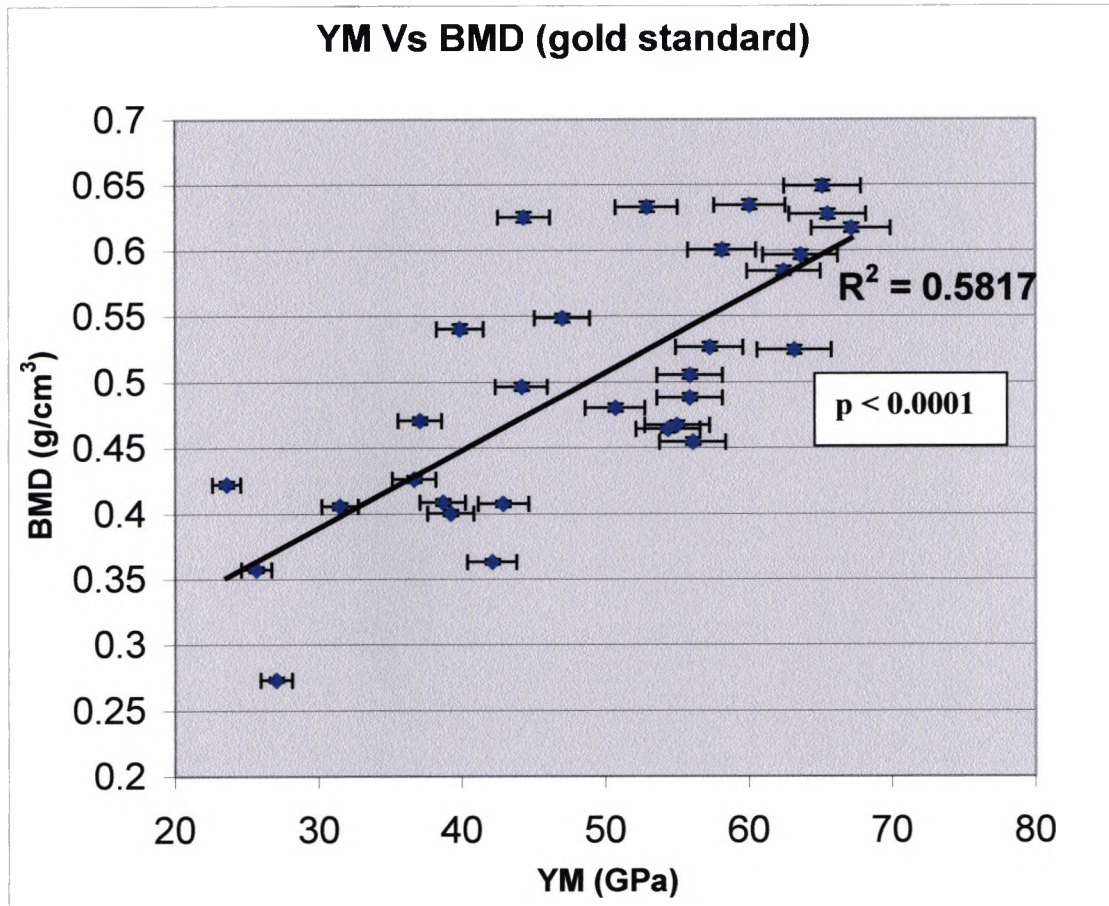


**Figure 3.9.** Relationship between YM and BMD (gold standard). Error bars for each technique are represented as two standard deviations.

Figure 3.9 above shows the relationship between YM and BMD for 30 samples. From the figure it can be seen that a positive relationship exists between BMD and bone strength. However, the relationship is not that strong suggesting that BMD is not the only determinant of bone strength. Studies revealed that the architecture of trabecular bone is also important in the estimation of bone strength. Assuming two bone samples that have

identical BMD values, if stress is applied to them, they will fracture at different points in time.



**Figure 3.10.** Two bone samples with identical BMD values. Note the difference in the arrangement of the trabecular bone within the samples and also the difference in the thickness of the trabecular plates.

Figure 3.10 shows two trabecular bone samples that have identical BMD. However, the sample on the right contains more thinner interconnected plates than the sample on the left containing a thicker and less interconnected arrangement. Studies have shown that trabecular bone samples with a more thinner interconnected arrangement (the sample on the right) can be much stronger than samples with a thicker arrangement (Kleerekoper et al, 1985). It can therefore be appreciated that BMD cannot be used as an isolated method for the estimation of fracture prevalence.

### ***3.6 Preparation of the MRI experimental set-up***

Scanning was performed with the use of a small bore research MRI scanner (Bruker Avance spectrometer) operating at 7 Tesla magnetic field strength with independent work stations linked for remote data processing. Data processing was performed on Sun workstations and PCs with software developed in house using MATLAB version 6.1 (The Mathworks, Inc).

---

The initial task prior to carrying out the MRI experiments was the identification, construction and optimization of the MRI accessories that would be used with the specific bone samples chosen for this study. In view of the vast amount of theoretical factors affecting the success of any given MRI experiment, it was decided that all these had to be investigated individually if useful data was to be obtained and relied upon. These factors can be classified into technical parameters (i.e. magnetic field strength, *RF* coil type and MRI accessories that offer reproducibility), tissue parameters (i.e. proton density, *T1*, *T2*, *T2\** and magnetic susceptibility) and imaging parameters (i.e. the choice of pulse sequence, *TR*, *TE* and voxel size), which interact in multiple ways and affect the resultant image appearance, resolution and quality. The following section is intended to provide an outline of the optimization with respect to the technical parameters. The optimization of all other factors will be discussed in subsequent sections according to the chosen MRI experimental protocol.

Since the samples had to be immersed in water for the experiments, it was decided that these should be placed in a container small enough to fit in the magnet, easy to handle and also shaped according to the circular nature of the magnetic bore in order to provide a better means of accurate positioning. Accurate positioning of the sample within the magnet was thought to be a very important factor since most of the MRI experiments would have to be performed on separate occasions and, if not accounted for, this could become a potential source of errors (due to variations in magnetic field uniformity in relation to the isocenter of the bore of the magnet). Therefore, it was decided that a standard clinical 50ml syringe would be suitable for use. In order to appreciate the possible effects of inaccurate positioning (and also to decide how much effort should be put into the design and construction of the sample holding devices), a pilot study had to be carried out and is presented here.

Since the standard spin-echo and standard gradient-echo pulse sequences would be employed in subsequent MRI experiments with the use of the bone samples, it was decided that both pulse sequences should be employed to scan a water-filled syringe at different locations within the bore of the magnet and calculating the SNR variation from

random positionings. SNR calculations were carried out using a standard image/background method. For each acquisition, a central slice was used and by placing 5 regions of interest (ROIs) in the signal portion (S) of the image as well as 5 ROIs in the background portion (N), SNR was calculated as the ratio of S/N. Figure 3.11 demonstrates an axial MR image of the water-filled syringe with a circular signal portion (i.e. water in the syringe) along with the 10 regions of interest that were deposited in order to calculate the SNR for each acquisition.

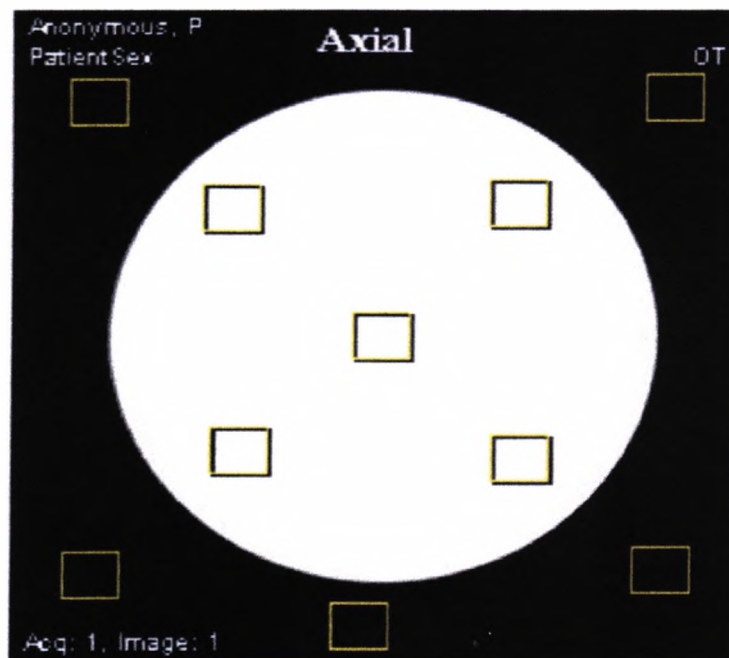


**Figure 3.11.** SNR calculation method.

All ROIs had the same number of pixels and S was measured from the mean of the 5 mean values of the 5 ROIs in the signal portion and N from the mean value of the 5 standard deviations of the 5 ROIs in the background. SNR was then calculated as S/N.

Using a manually actuated holding device, the syringe was initially positioned in the isocenter of the bore of the magnet and then moved in increments and in different directions by keeping the same imaging parameters constant for both the spin-echo and gradient-echo pulse sequences (see figure 3.12). The increments that the syringe was moved were 11mm and 25mm in four directions with respect to the isocenter of the magnet (i.e. up, down, left and right). The mean and standard deviation of the SNR

values from all nine positions investigated were used to calculate the coefficient of variance from  $\frac{SD \times 100}{mean}$ . The same operation was carried out on data from both the spin-echo and gradient-echo acquisitions.

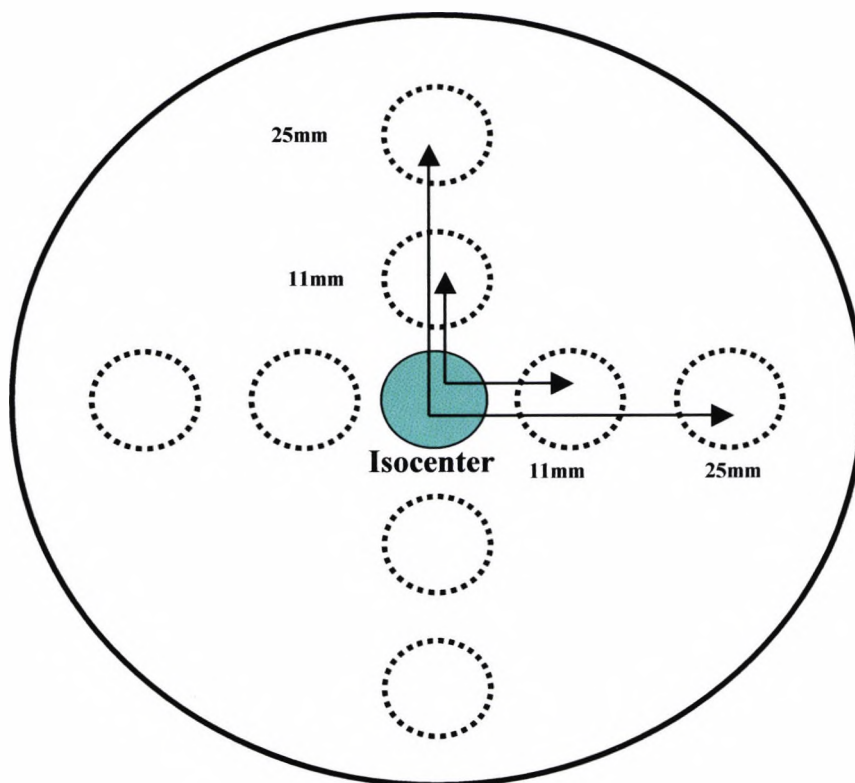


**Figure 3.12.** Investigation of the effects of inaccurate sample positioning within the bore of the magnet

The results revealed that there was a 3.27% fluctuation for the spin-echo data and 19.3% for the gradient-echo. In addition, by investigating each position individually, it was concluded that the further away from the isocenter the sample was positioned, the more fluctuation was present in the results. The higher fluctuation noted for the gradient-echo data was in accordance with the theoretical predictions since the effects of inhomogeneity cannot be eliminated with the gradient reversal, whereas for the spin-echo, the application of the 180-degree *RF* pulse accounts for these effects.

In view of the findings from the above investigation, it was decided that some adjustments had to be made in order to account for these effects. It was decided that a

---

standard 50ml syringe could still be used to accommodate the bone sample. One side of the syringe was cut off and two identical handles were used to support the sample between them in the middle of the syringe tube which was filled with water. The sample was secured in a precisely cut plastic ring which had a square opening in the middle (see figure 3.13).

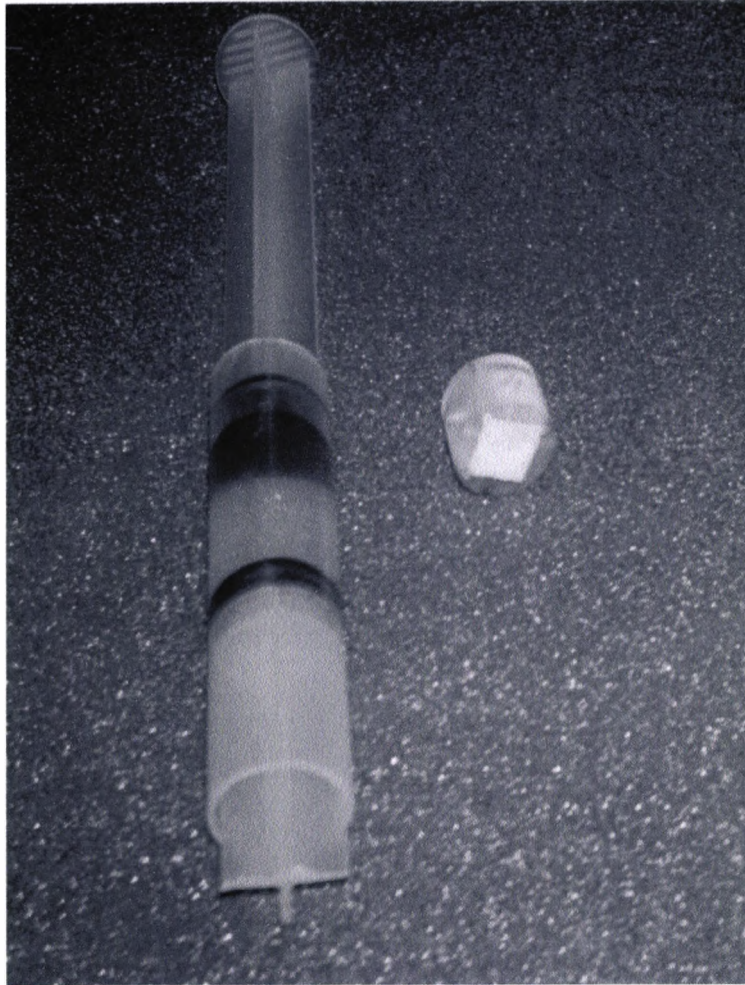


**Figure 3.13.** The syringe used for the experiments with a bone sample secured in a plastic ring that fits in the syringe in the space between the two handles which is filled with water.

Assuming a three dimensional Cartesian co-ordinate system with the Z direction along the bore of the magnet, the purpose of the ring was to provide accurate positioning of the sample in the x, y direction within the syringe since the z direction could be controlled simply by pushing the handles of the syringe.

---

In order to provide accurate positioning of the sample/syringe in the isocenter of the bore of the magnet, a device had to be constructed (see figure 3.14).

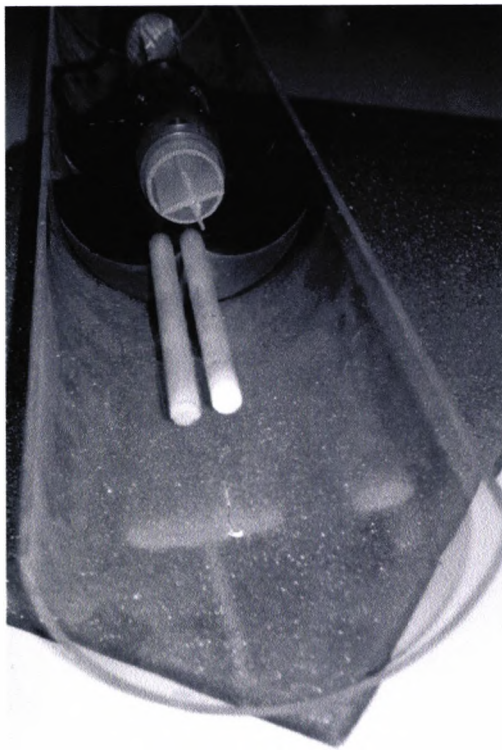


**Figure 3.14.** The positioning device with the syringe attached in the middle.

The semi-circular nature of the device accounted for the correct positioning of the sample in the x, y direction (with respect to the bore of the magnet) and the sliding properties of the whole device, accounted for the z direction.

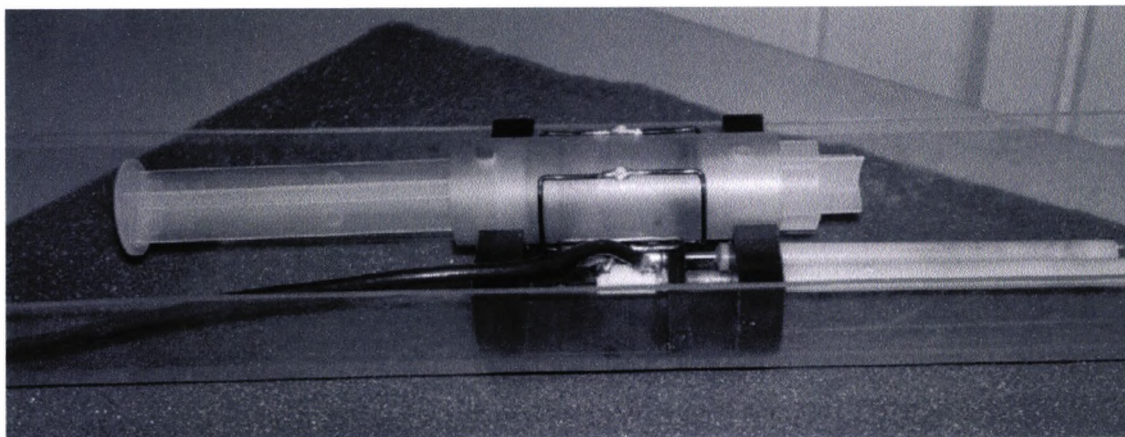


**Figure 3.15.** The complete experimental device with the syringe and the coil attached to it.

---

In consideration of the theoretical influences of the *RF* coil design and properties with respect to the SNR, a saddle coil was designed and built in-house at UCL by Dr. David Carmichael and Dr. John Thornton (see figure 3.15). The saddle coil design uses a pair of coils wound on a cylindrical surface. The coils face each other and are located symmetrically on a cylindrical surface of known radius and are connected so as to carry current in parallel directions. Because of its easy adaptation to tests tubes (in this case the syringe with the sample in) as well as the ability to produce a relatively homogeneous field near its centre (Bronskill & Sprawls, 1993), this design was chosen.

## ***Chapter 4: “Quantitative Magnetic Resonance (QMR) and its Value in the Investigation of Trabecular Bone”***

Direct MR measurement of mineralized elements has been relatively unsuccessful, because bone tissue is a solid material that has low mobile proton density. However, trabecular bone can be assessed indirectly by measurements of the surrounding bone marrow. QMR uses the fact that near the boundary of two physical phases of different magnetic susceptibility (in this case, trabecular bone and bone marrow), the magnetic susceptibility of trabecular bone is much smaller than the bone marrow. This causes spatial inhomogeneities in the static magnetic field which result in an alteration of the marrow relaxation times and properties which can be measured (Majumdar & Genant, 1995b).

Studies have shown that marrow relaxation times  $T_2$  and particularly  $T_2^*$  may be related to the quantity and spatial arrangement of trabecular bone. Since quantity and spatial arrangement of trabecular bone are also directly related to bone strength, it was decided that the technique should be further investigated in an effort to determine whether it can have a value in the characterization of trabecular structure and fracture prevalence. The idea was to carry out these investigations with the use of bone samples (see chapter 3 for more information on the bone sample characteristics), which had accurately predetermined physical and biomechanical properties in an effort to obtain a better understanding of the value of this technique.

In-vitro investigations were carried out with the use of 30 bone samples at 7 T magnetic field strength. The details of the method employed in these investigations are presented along with the findings, which are discussed with respect to similar investigations.

---

#### 4.1 Theory

If samples consisting of materials with different magnetic susceptibilities (as in the case of bone and marrow) are placed in a magnetic field, the magnetic lines of force are distorted through this material (see figure. 4.1 below).

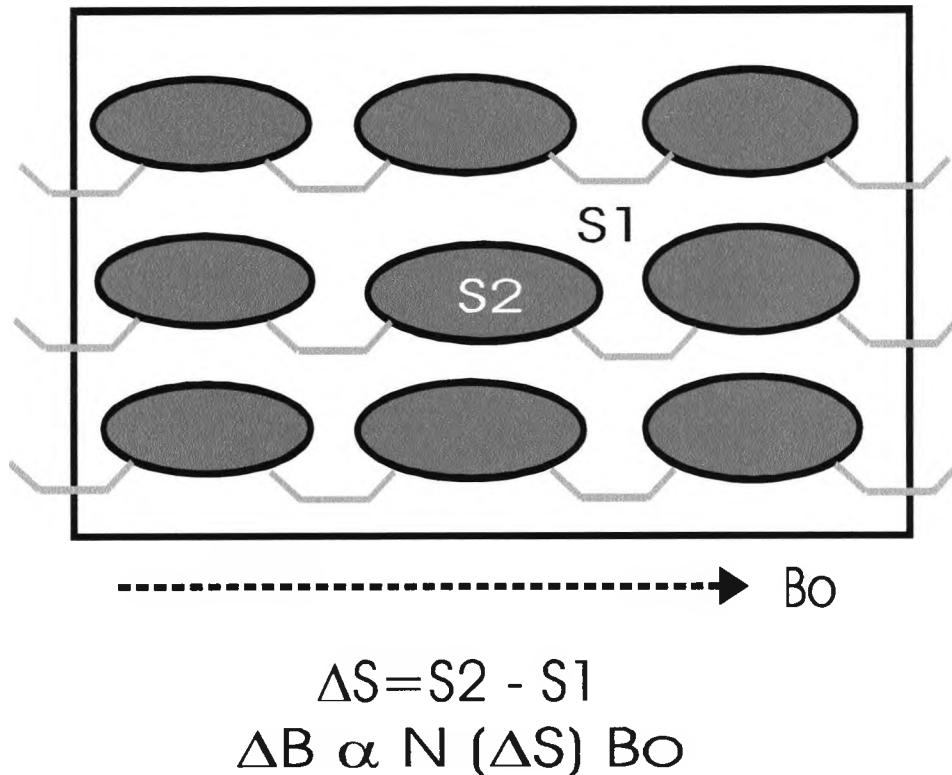


**Figure 4.1** Susceptibility variations within a sample such as between the trabecular bone (S2) and bone marrow (S1) result in a distortion of the magnetic lines of force. This results in the generation of magnetic field inhomogeneities and gradients in the magnetic field ( $\Delta B$ ) that depend on the magnitude of the difference in magnetic susceptibility ( $\Delta S$ ), field strength ( $B_0$ ) and the number of discontinuities in magnetic susceptibility ( $N$ ) (Majumdar & Genant, 1995b).

The diffusion of protons in these magnetic field inhomogeneities result in an irreversible loss of magnetization which cannot be fully recovered with the application of a 180-degree *RF* pulse in Spin-Echo (SE) imaging, and therefore, a shortening of the marrow relaxation time  $T_2$  occurs. As seen from the equations in figure 4.1, the effect on the marrow relaxation time  $T_2$  can be more pronounced in higher magnetic field strengths. In Gradient-Echo (GE) sequences the effect of magnetic field inhomogeneities are manifested more strongly by observing the marrow relaxation time  $T_2^*$ . In GE sequences the magnetization is dephased and decays faster than would be predicted by the

relaxation time  $T_2$  alone, and the additional contribution due to field inhomogeneities and the  $T_2$  relaxation properties are combined to give one characteristic time,  $T_2^*$  (Majumdar & Genant, 1995b). Figure 4.2 below demonstrates the effect of magnetic field inhomogeneity on  $T_2^*$ .

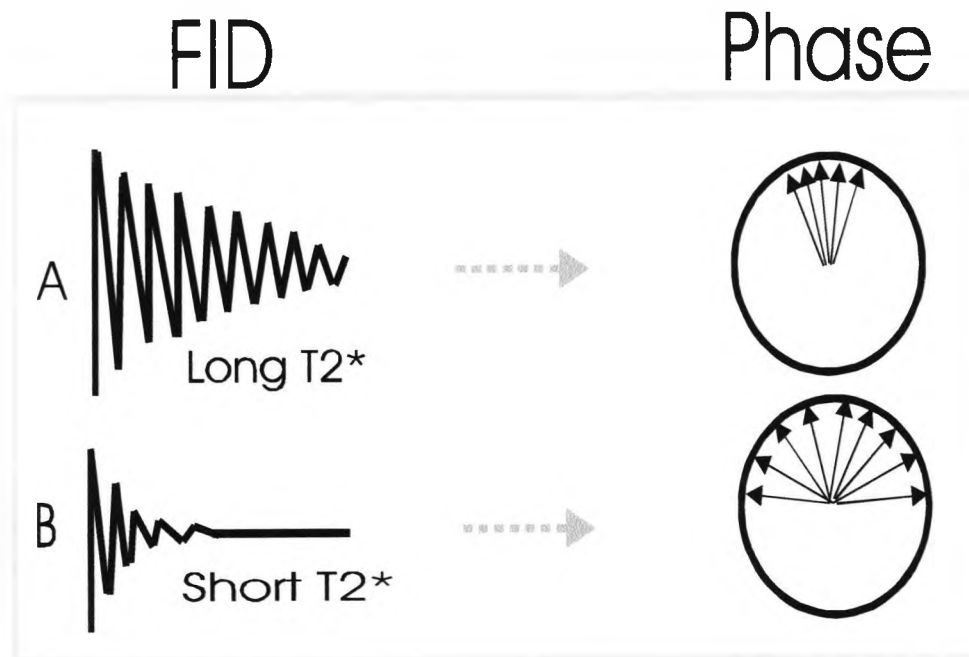


**Figure 4.2.** Effect of magnetic field inhomogeneity on  $T_2^*$ . (A) Homogeneous field. (B) Inhomogeneous field. Note that the more inhomogeneous the field the faster the isochromats constituting the magnetisation are dephased and thus the shorter the  $T_2^*$  (Chung et al, 1993).

GE pulse sequences have been extensively used for the determination of  $T_2^*$  and SE for the determination of  $T_2$ . In both cases, images are usually obtained at different  $TE$  values by keeping  $TR$  constant.

In SE, signal intensity  $S$  decays according to,

$$S = S_0 \cdot \exp\left(-\frac{TE}{T_2}\right) \quad (\text{eq. 4.1})$$

---

Taking natural logarithms gives,

$$\log(S) \propto -TE/T_2 \quad (\text{eq. 4.2})$$

The log of the total signal intensity from the volume selected varies linearly with echo time. A first order 'least squares' polynomial fit to the data can then determine the overall  $T_2$  value. The same process is employed in GE by substituting  $T_2$  for  $T_2^*$  on the above equations and plotted in the same way as described above (see figure 4.3 below).

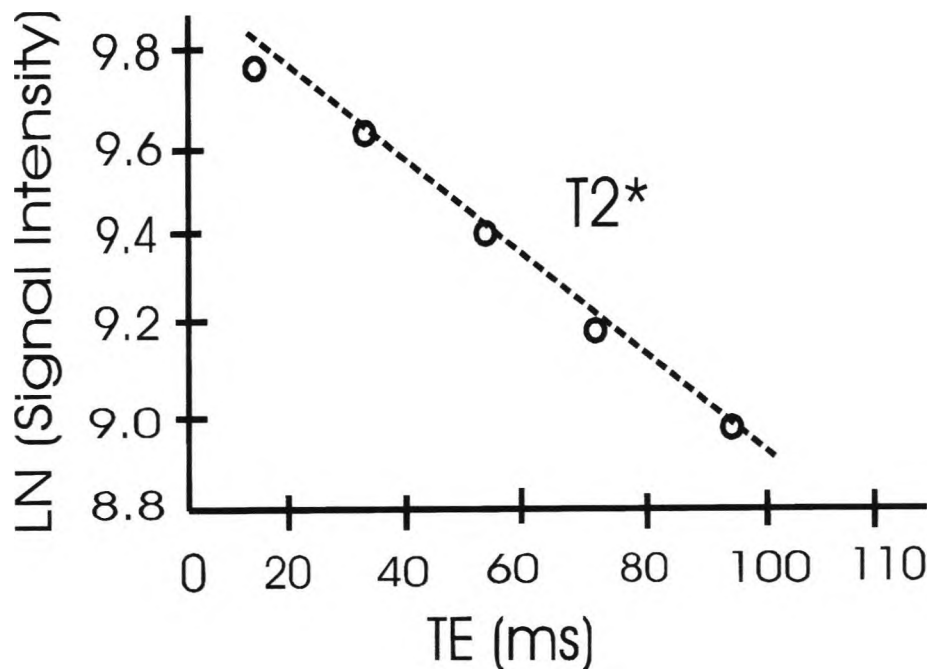


**Figure 4.3.** Signal intensity versus  $TE$  with the use of GE for the determination of  $T_2^*$ .

As seen in chapter 2, the decay rate  $1/T_2^*$  (or  $R_2^*$ ) is the sum of two contributions, i) the non-reversible transverse relaxation rate  $1/T_2$  or  $R_2$  (which is related to the relative amount of free water, protein, fat and other carbon-hydrogen compounds in the tissue) and ii) the reversible transverse relaxation rate  $1/T_2'$  or  $R_2'$  (which is related to extrinsic and intrinsic magnetic inhomogeneity. Extrinsic magnetic inhomogeneity is caused by imperfect magnetic shimming or other external factors and intrinsic inhomogeneity is the

difference in magnetic susceptibility between bone and marrow). The relationship between  $R2^*$ ,  $R2$  and  $R2'$  is shown by the following equations,

$$\frac{1}{T_2^*} = R_2^* = \frac{1}{T_2} + \frac{1}{T_2'} = R_2 + R_2' \quad (\text{eq. 4.3})$$

Although most studies with the use of QMR for the investigation of trabecular structure rely on a measurement of the total transverse relaxation rate  $R2^*$ , a direct measurement of  $R2'$  is more desirable (especially for in-vivo situations) since  $R2'$  is purely related to magnetic inhomogeneity due to a difference in magnetic susceptibility between bone and marrow. On the other hand,  $R2^*$  may change as a result of variations in  $R2$  unrelated to changes in trabecular bone density or spatial distribution.

Although GE and SE can be performed separately and used in combination to calculate  $R2'$  (using the equation 4.3 described above), investigators have explored the possibility of measuring  $T2^*$  and  $T2$  in one acquisition. The Partially Refocussed Interleaved Multiple Echo (PRIME) sequence is one of them (Kang et al, 1999). The sequence is both SE and GE containing both 180-degree  $RF$  pulses and gradient reversals (see figure 4.4).

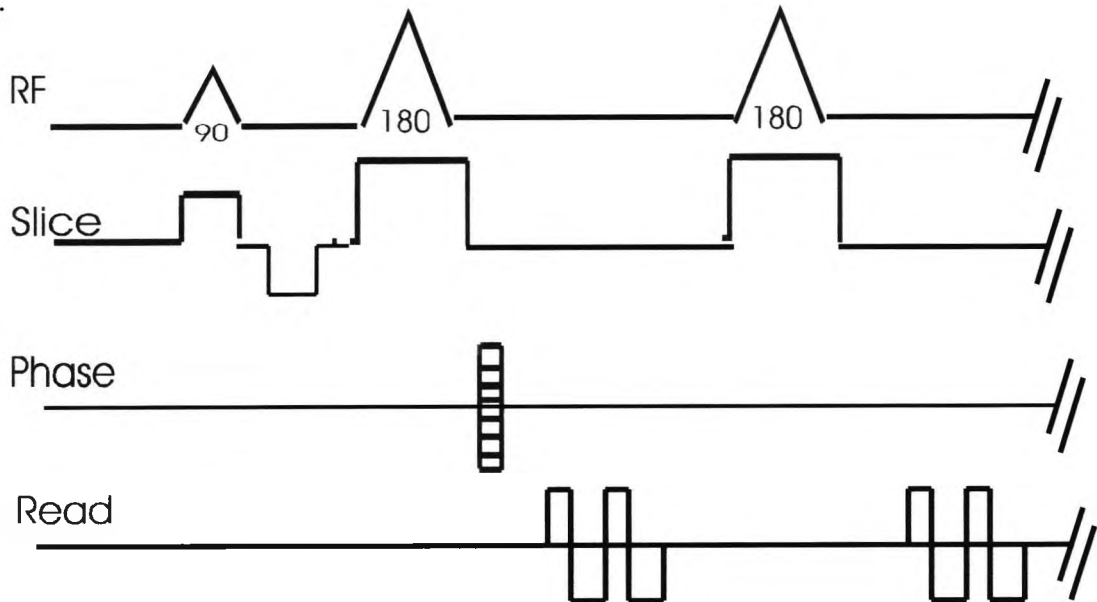


**Figure 4.4.** The PRIME sequence.

In addition, investigators have also explored the possibility of measuring  $R2'$  directly by modifying the conventional SE pulse sequence, (Rosenthal et al, 1990). These efforts resulted in the development of the asymmetric SE (ASE). Figure 4.5 below shows the pulse sequence diagram of an ASE.

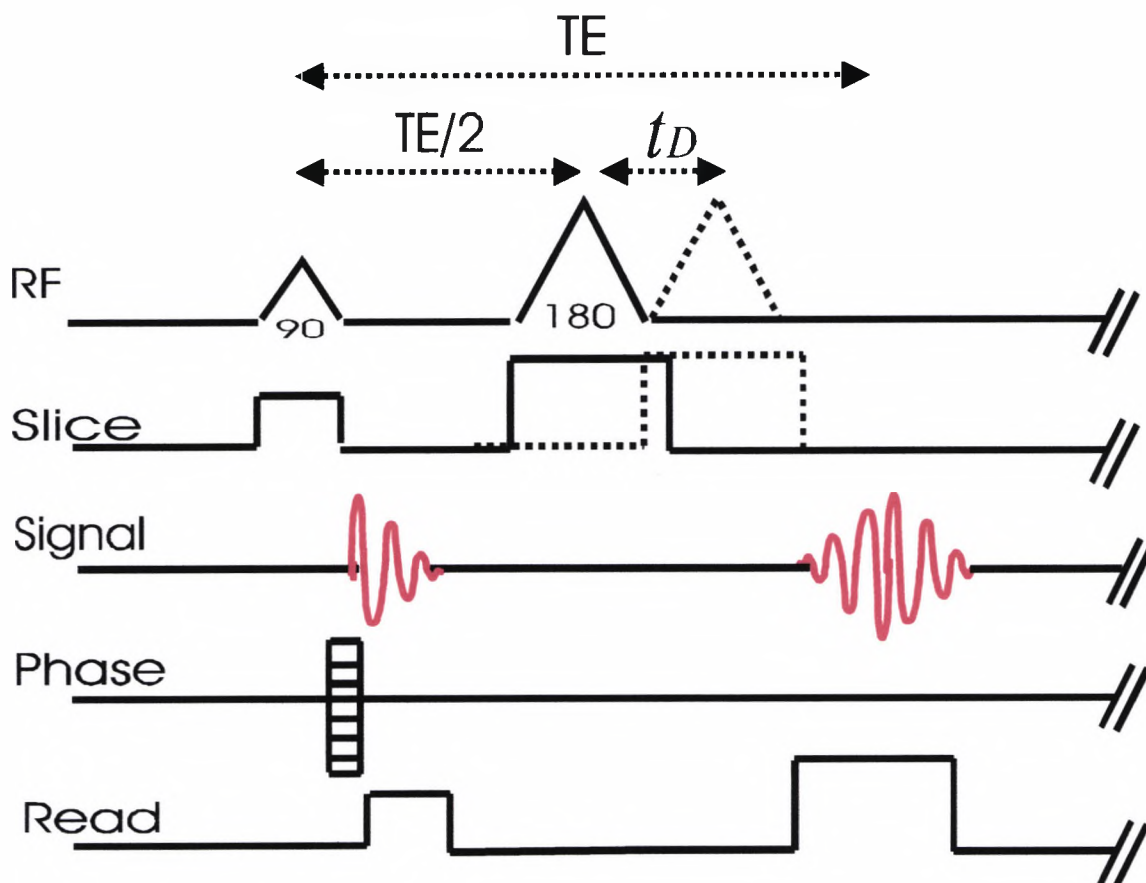


**Figure 4.5** Asymmetric SE pulse sequence.

In the ASE sequence, the 180-degree  $RF$  pulse is offset by a time  $t_D$  with respect to time  $TE/2$ , its placement in a traditional SE sequence. This offset introduces a decrease in signal intensity compared to that at  $t = 0$ , which is due to transverse dephasing of spins due to field inhomogeneities only, and does not include the effects of intrinsic relaxation ( $T_2$ ). By shifting the 180-degree  $RF$  pulse in  $t_D$  increments, signal loss as a function of time can be plotted which is often referred to as “ASE decay curve” (Selby et al, 1996).

The equation describing the signal intensity  $I$  for an ASE, according to Engelke et al (1994), may be written as,

$$I = I_0 e^{-\frac{TE}{T2}} \left( 1 - 2e^{-\frac{TR - (\frac{TE - 2t_D}{2})}{T1}} + e^{-\frac{TR}{T1}} \right) e^{-2t_D(R2')} \quad (\text{eq. 4.4})$$

With  $I_0$  being a scaling factor that includes contributions from proton density and slice profile,  $TR$  is the repetition time,  $TE$  the echo time, and  $t_D$  the offset time between  $TE/2$  and the time at which the refocusing pulse is applied.  $T1$  and  $T2$  are the spin lattice and spin-spin relaxation times respectively, and  $R2'$  describes the additional decay induced by magnetic susceptibility differences and inherent inhomogeneities.

As shown,  $R2'$  may contain information on both the BMD content and spatial arrangement in trabecular bone. In addition, experimental studies with the use of a physical model have shown that  $R2'$  may also be affected by the orientation of the trabeculae with respect to the main magnetic field,  $B_0$  (Yablonskiy et al, 1996).

As shown in previous chapters, trabeculae develop as an anisotropic lattice. They show, however, thicker columnar or plate-like trabeculae along lines of biomechanical stress (see figure 3.2, chapter 3) and nearly perpendicular thinner supporting structures. By concentrating on phantoms to simulate bone samples with such an arrangement (as in the case of the bone samples used in this study), Yablonskiy et al (1996) have demonstrated that  $R2'$  relaxation rate is equal to,

$$R2' = S \times 2\pi\gamma \times \Delta\chi \times B_0 \times \sin^2 \theta \quad (\text{eq. 4.5})$$

With  $S$  being the volume fraction of the trabecular columns along lines of biomechanical stress,  $\gamma$  the gyromagnetic ratio,  $\Delta\chi$  is the susceptibility difference between substance and substrate (bone and marrow, for example),  $B_0$  the magnitude of the main magnetic field and  $\theta$ , the angle between the main magnetic field ( $B_0$ ) and the columnar orientation.

---

#### ***4.2 A review of the studies with the use of Quantitative Magnetic Resonance***

From theoretical considerations (as described above), a shortening of the relaxation time  $T2^*$  (i.e. increased relaxation rate  $1/T2^*$  or  $R2^*$ ) becomes greater with an increase in concentration of trabecular bone in the surrounding homogeneous marrow tissue. Thus, in a normal dense trabecular network,  $T2^*$  shortening should be more pronounced than in rarefied osteoporotic trabeculae (Majumdar & Genant, 1995b). Experimental studies have explored the theoretical predictions.

Using MR techniques, the impact of bone on the MR properties of marrow were first investigated in 1986 by Davis et al (1986). In their study, trabecular bone from autopsy specimens were ground up and sifted into a series of powders with varying densities. The bone powders were immersed in saline and cottonseed oil (i.e. to simulate bone marrow) and the relaxation times were investigated with the use of a 5.88 T magnetic field strength system. The authors found that with increasing density, there was an increase in field inhomogeneities which resulted in the shortening of  $T2^*$  relaxation time.

The effect of trabecular bone on marrow  $R2'$  was also detected at lower field strength of 0.6 T by Rosenthal et al (1990). The authors performed imaging experiments in excised cadaveric specimens with the use of an asymmetric SE pulse sequence and found that the relaxation rate  $R2'$  of saline present in the marrow spaces was higher (i.e. shorter  $T2'$  time) than that of pure saline that constituted the phantom and suggested that  $R2'$  is related to the density of bone. The authors also carried out a comparison of their findings with other similar studies with the use of higher magnetic field strengths and postulated that  $R2'$  relaxation rate increases with magnetic field strength, confirming the theoretical predictions.

From computer simulations and phantom studies it has been shown that the relaxation rate  $1/T2^*$  of bone marrow is affected not only by the density of the trabecular matrix but also by its spatial architecture and this was initially addressed by Majumdar (1991). The simulations used a two-dimensional model of randomly distributed point susceptibility discontinuities embedded in a homogeneous medium assuming a magnetic susceptibility

---

difference between the two media of  $\Delta\chi$ . The results showed an increased  $1/T2^*$  decay rate with a) increasing  $\Delta\chi$ , b) increasing number of points, and c) an influence of the distribution of the susceptibility discontinuities on the  $1/T2^*$  decay rate. These results indicate a dependency of  $1/T2^*$  on both density and structure.

In comparison with the above, a study conducted by Engelke et al (1994) sought to investigate the possibility of separating the density from the structural effects on the relaxation time  $T2^*$ . In order to achieve this, several phantoms were built which consisted of parallel polyethylene strings arranged in a variety of different patterns to simulate a) a constant uniform trabecular distribution with increasing trabecular thickness (i.e. simulating varying density but constant spatial distribution of the trabeculae) and b) different structures with identical overall trabecular density. An asymmetric SE pulse sequence was used to determine the  $R2'$  relaxation rate. The results showed an increasing  $R2'$  decay rate with a) decreasing spacing while the string density was constant and b) with increasing string density while the string arrangement was constant.

A study by Kang et al (1999), used twelve cuboidal bone samples extracted from sheep vertebrae to study  $R2'$  and  $R2^*$  with the use of the PRIME sequence. The samples were immersed in water for the experiments and the bone properties were determined from physical calculations. The bone samples were cut from predetermined locations that had well defined trabecular orientation and by imaging the samples at 0 and 90 degrees with respect to  $B_0$  (in order to remove the dependence on density) they concluded that 35% of the variation in  $R2'$  may be accounted for by variations in trabecular separation. In addition, the authors found that there was little variation between  $R2'$  and  $R2^*$  which was assigned to the fact that the samples were water filled with a consequent narrow range of  $T2$  values between samples. The need to measure  $R2'$  directly in-vivo was stressed due to a possible wide range of  $T2$  values from different marrow compositions that might affect  $R2^*$ .

The angular effect of the columnar or plate-like trabeculae along lines of biomechanical stress with respect to  $B_0$  has also been investigated. This dependence was firstly

---

identified by Yablonskiy et al (1996). Using a physical model, the authors sought to quantify the anisotropic behavior of uniaxial trabecular bone. To test the model, a phantom of parallel polyethylene filaments was scanned every 15 degrees between 0 and 90 degrees with respect to  $B_0$ .  $R2'$  decay showed anisotropic behavior and changed according to  $\sin^2(\theta)$ , confirming that columnar structures parallel to  $B_0$  will cause less MR susceptibility effects than any other orientation, with greatest  $R2'$  decay observed at 90 degrees. A similar observation was made by Brismar (2000) using 12 defatted human vertebrae.

The investigation of  $R2'$  in trabecular bone has recently been described in in-vivo situations in a small number of studies. One of the first reported in-vivo assessments of  $R2^*$  was by Wehrli et al (1995). The authors employed 146 osteoporotic women with predetermined vertebral BMD measured by DEXA and performed QMR experiments for the calculation of  $R2^*$  in the same subjects. The results from the study revealed that  $R2^*$  was lower in patients with lower BMD levels with a correlation of  $R^2=0.54$ .

A study by Guglielmi et al (1995) sought to investigate the relationship of  $R2^*$  and BMD measured with DEXA in 6 volunteers. The region of interest was the calcaneus in this particular case. Measurements were carried out with the use of a 1.5 T scanner and  $T2^*$  relaxation times were calculated with a standard GE pulse sequence. The results from this study revealed a positive correlation between  $R2^*$  and BMD with  $R^2=0.66$ .

A study by Song et al (1997) presented preliminary findings regarding the effect of magnetic field strength on the measured  $R2'$ . The authors carried out experiments with the use of 5 volunteers at 1.5 T and 4 T magnetic field strengths. The region of interest in this study was the calcaneus. The results from this study showed  $R2'$  to increase by a factor of 2.73 between 1.5 T and 4 T.

The first reported study looking into the relationship of  $R2^*$  and BMD in-vivo in the hip was in 1998 by Link et al (Link et al, 1998a). The authors obtained  $T2^*$  maps of the proximal femur at 1.5 T and compared the findings with BMD determined by DEXA.

---

Twenty-three postmenopausal women were employed in this study and a positive correlation was shown with  $R^2=0.50$ .

#### **4.3 Pilot studies – technical considerations**

In consideration of the vast amount of theoretical factors involved in the successful conduction of any MRI experiment, it was decided that optimization of the QMR technique pertaining to this particular study with the use of trabecular bone cubes was needed. It was decided that  $R2'$  values should be obtained with the use of GE (i.e.  $T2^*$  calculation) and SE (i.e.  $T2$  calculation) independently for reasons that have been explained.

One bone sample was used for the pilot studies and the focus of attention was the determination of the appropriate imaging parameters to use for valid calculations of the  $T2$  and  $T2^*$  relaxation times of the samples. In addition, data analysis considerations, angulation considerations and reproducibility assessments of the QMR technique are also presented here.

Information regarding the optimization of the technical parameters (i.e. MR imaging accessories and  $RF$  coil) and the characteristics of the bone samples used in this study can be found in chapter 3.

##### **4.3.1 Imaging parameters**

Although different acquisition modes are used in each case (i.e. spin echo and gradient echo),  $T2$  and  $T2^*$  relaxation times can be calculated in a similar way by obtaining images with constant  $TR$  and different  $TE$  values. The relaxation times are then calculated from the slope of the natural logarithm of signal intensity against  $TE$ . There can be numerous possible combinations of  $TR$  and  $TE$  values chosen to produce valid relaxation times of different samples. The important point that had to be considered here was the fact that the bone samples were immersed in water for these experiments rather than in bone marrow as would be the case for in-vivo situations. Although a variety of different media were considered for inclusion in the water solution to allow for reduced  $TR$ , this

---

was later abandoned as it was realised that very large quantities of the solution would be required since most of the procedure of preparing and securing the bone samples in the syringe had to be carried out manually inside large containers of any given solution.

In view of the theoretical influences of  $TR$  on the SNR, the higher the  $TR$  values (with respect to the  $T1$  relaxation time of the tissue) chosen, the higher the signal will be. However, by using very high  $TR$  values, the total scanning time increases and, therefore, a balance has to be achieved between these two factors. With respect to the  $TE$ , on the other hand, the lower the  $TE$  values (with respect to the  $T2$  relaxation time of the tissue), the higher the signal will be. In addition, the more  $TE$  values are employed, the more accurate the slope of signal intensity against  $TE$  will be since more points will be present on the graph (Whittall et al, 1999).

Bearing in mind the above relations, different combinations of  $TR$  and  $TE$  values were performed for both  $T2^*$  and  $T2$  calculations and an appropriate imaging protocol was established for GE and SE, respectively. For  $T2$ , a standard SE sequence (MSME) was used. The sequence was tested in two modes. Firstly, images with six different  $TE$  values were obtained in separate acquisitions (single-echo acquisitions); initially the  $TE$  values used were 15ms, 35ms, 45ms, 65ms, 75ms and 85ms. Secondly, six images were formed from multiple echoes obtained in the same acquisition by the insertion of extra 180-degree  $RF$  pulses. The echo times used were 20ms, 30ms, 40ms, 50ms, 60ms and 70ms with an image being formed at each. The other parameters used were FoV=3cm /  $TR=3000$ ms / Matrix size=96x96 / 16 adjacent slices acquired in an interlaced order / slice thickness = 1mm. Both protocols achieved a satisfactory measurement. While there would be a time advantage for using a multiple-echo sequence in-vivo, the multiple single-echo approach was used on the sample to obtain values of  $T2$  because it was considered more robust to any variation in  $B_1$ . In order to achieve a faster (but at the same time meaningful) protocol, the  $TE$  values were later decreased to three (i.e. 20ms, 50ms and 80ms), which had no significant impact on the calculated  $T2$ .

---

A similar process was employed for the optimization of the  $T2^*$  calculations. A standard GE sequence supplied by the manufacturer (GEFI\_BIO) was used to obtain  $T2^*$  weighted images. Initially, six different  $TE$  values were employed that were later reduced to three of 5ms, 15ms and 25ms. The other imaging parameters used were FoV=3cm /  $TR=2000$  / Matrix size=96x96 /  $30^\circ$  flip angle and 16 adjacent slices / slice thickness=1mm. Although more efficient protocols may have been used (more likely in the expense of scanning time), it was decided that standardization of these specific GE and SE protocols would still produce comparable results when all 30 samples were employed.

#### 4.3.2 Data analysis

During the optimization of the imaging parameters described above,  $T2$  and  $T2^*$  relaxation times of the sample were calculated for the whole cube (i.e. all 16 slices) from the signal intensity versus  $TE$  curve. For easier and quicker data analysis, a function was developed in-house using the MATLAB 6.1 interface. Initially, the algorithm requires the data files to be specified manually. The manual deposition of a region of interest to include the bone cube area only from one of the 16 slices from each scan is then required and  $T2$  or  $T2^*$  are computed automatically for the whole cube (all the slices) from the slope of the natural logarithm of signal intensity versus  $TE$ . Since both GE and SE acquisitions were performed on each occasion without moving the sample, the coordinates of the ROI were kept invariant for all calculations. This enabled the obtainment of both  $T2$  and  $T2^*$  values from the same ROI within each sample.

In addition, in order to avoid possible contamination of the results from automatic scaling of the data by the image reconstruction algorithm of the manufacturer, it was decided that the resultant images had to be reconstructed “manually” from the “fid” file obtained from each scan. A function in MATLAB 6.1 was developed in-house (by Dr. Andrew Priest) to perform this task and was kindly made available for all subsequent experiments.

#### 4.3.3 Reproducibility assessment

With respect to the reproducibility assessment of these QMR imaging protocols, several experiments had to be carried out prior to the actual data collection with the use of the 30

---

bone samples. In this particular QMR technique, it was hypothesized that two main sources of errors were likely to exist and should be investigated: those that enter at the time of data acquisition and those that enter during data analysis. The only contribution to precision error occurring during image analysis is the placement of the analysis region of interest (ROI), which is a manual operation. At the time of data collection, on the other hand, various machine dependent factors (i.e. coil tuning, main magnetic field inhomogeneity, transmitter/receiver settings, incorrect positioning of the sample), may contribute to the overall precision error of the technique. It is possible to separate these two contributions so that technique modifications aimed at improving errors can be directed at either data acquisition or analytic procedures accordingly.

In order to do this, one bone sample was used for this experiment, and by keeping all imaging parameters constant (field of view, matrix size, number and thickness of slices,  $TR$  and  $TE$ ), a series of identical scans was performed. This series of identical scans (using the final imaging protocols identified from the optimization stage) for  $T2$  and  $T2^*$  calculations was performed firstly, by leaving the bone sample in the magnet and simply repeating the  $T2$  and  $T2^*$  imaging protocols (i.e. using the initial coil tuning, transmitter/receiver settings) and secondly, by removing the bone sample from the magnet each time and having to reposition the sample. Initially, a series of 10 identical scans were performed for  $T2$  and  $T2^*$  calculations without moving the sample from the magnet and a series of 10 identical scans were then performed by repositioning the sample 10 times in the magnet.

The results from the repeated experiments with both GE and SE without moving the sample revealed no deviation at all between the 10 measurements of  $T2^*$  and  $T2$ , respectively. This finding suggested that the initial coil tuning, transmitter/receiver settings and main magnetic field homogeneity remained fairly robust between measurements without any deviation. In addition, with respect to the data analysis method, the possibility of errors was ruled out since the function that was developed in MATLAB for the image analysis and  $T2^*$  and  $T2$  calculations had a pre-specified location that the ROI was to be applied to which was repeated for all slices and all scans.

---

With respect to the 10 repeated  $T2$  and  $T2^*$  measurements by repositioning the sample each time, 4.3% and 2.3% errors were identified, respectively. The reduced precision of SE was assigned to a number of factors ranging from the data analysis technique (i.e. imperfect positioning of the ROI on every separate occasion) and technical parameters (i.e. coil tuning, transmitter/receiver settings). Most importantly, however, the level of diffusion was predicted to be a significant factor affecting the measured value of  $T2$  due to the sample being filled with free water (Deichmann et al, 1995). This would not normally be such a strong influence in-vivo because water protons in marrow are much less mobile. The errors identified with the use of GE were assigned to a combination of data analysis and imperfect shimming of the main magnetic field on each separate occasion.

Despite the errors identified from the reproducibility assessment, it was decided that both techniques could still be used for the data collection. Based on the recommendation by Och et al (1992) that measured SNR values with the use of a standard imaging protocol should be within 5% of the original value for Quality Assurance (QA) testing, it was decided that further technique modifications were not necessary and would have added further delay to the main data collection.

#### 4.3.4 Effects of angle

As it has been shown from theory, the trabecular orientation with respect to the main magnetic field strength can also have an effect on the calculation of the relaxation times and this should be taken into consideration. Since the bone samples used in this study were obtained from a predetermined location with known trabecular orientation, it was thought that this effect could be partly controlled by placing all the samples in a similar manner with respect to main magnetic field (i.e. the trabecular flow parallel to  $B_0$ ) when all 30 samples were employed for the actual data collection.

However, in order test the hypothesis that  $T2^*$  is indeed affected by the orientation of the trabecular structure, the same bone sample that was used for the pilot studies was employed. The sample was scanned with the use of the gradient echo and the final

imaging parameters that were identified from the optimization stage by calculating the  $T2^*$  value of the sample (all 16 slices) each time. A purpose built sample holder was used which allowed the rotation of the sample in various degrees of angle with respect to  $B_0$  (see figure 4.6 below). The sample holder was made with the use of a syringe so that the same  $RF$  coil could be used. A special rotating mechanism was located and adapted to fit within the syringe. Special insulation was used to allow for the manual rotation (black handle) of the sample within the water-filled environment.



**Figure 4.6.** The sample holder used for the investigation of the effect of angle on  $T2^*$ . The black handle on the side allowed for a precise manual rotation of the sample within the syringe in accurate increments of 10 degrees.

The  $T2^*$  value of the whole cube (all 16 slices) was calculated for 0 to 90 degrees in increments of 10 (see figure 4.7).

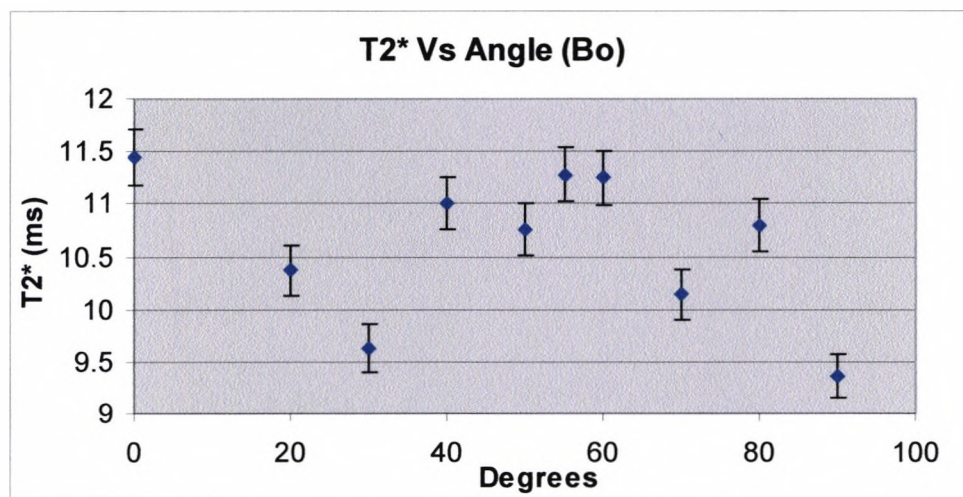


**Figure 4.7.** Effects of angle on  $T2^*$ .

---

From figure 4.7 it can be seen that  $T2^*$  can be affected by the orientation of the trabecular columns with respect to  $B_0$  (irrespective of density). Although the  $T2^*$  value for 0 degrees was  $T2^*=11.45\text{ms}$  and for 90 degrees  $T2^*=9.36$ , indicating a variation of 18.25%,  $T2^*$  did not seem to be affected in a linear fashion as predicted theoretically. This can be explained by appreciating the fact that the orientation of the trabeculae (although defined) cannot be compared to the well defined parallel string filaments of the phantom that the  $\sin^2(\theta)$  law applies. The nearly perpendicular thinner supporting structures within the defined thicker trabecular distribution are, therefore, responsible for this deviation, which can be unique for each bone sample (i.e. based on the number or thickness of these structures).

#### **4.4 Method**

Quantitative measurements (i.e.  $R2'$ ) were performed at 7 T on 30 bone samples of similar dimensions but different properties with the use of the imaging protocol that was identified from the optimization stage (see section 4.3.1). The 30 samples were scanned on different occasions individually and both  $T2$  and  $T2^*$  imaging protocols were employed for each sample on every occasion. All the samples were positioned in the magnet in a similar manner so that the trabecular orientation was parallel to the main magnetic field.

Prior to all the measurements, each sample was imaged individually with the use of a high resolution imaging protocol in order to ensure that no air bubbles were present within the trabecular structure of each sample. In this way, susceptibility artefacts (i.e. from air/bone/water boundaries) that would interfere with the data analysis, would be eliminated.  $R2'$  values for each sample (whole cube) were calculated from the  $T2$  and  $T2^*$  values with the use of a software that was developed in-house (see section 4.3.2).

In order to identify possible relationships between  $R2'$  and the biomechanical properties of the bone samples, BMD and YM of the samples were also identified (see chapter 3).

---

#### 4.5 Results

The graphs, including the linear fits and  $R^2$  values on the graphs were generated using Excel (Microsoft). The errors on the graphs were calculated from reproducibility assessments pertaining to each technique individually and are presented as two standard deviations.

##### 4.5.1 QMR and BMD

Figure 4.8 below indicates the relationship between  $R2'$  and BMD for 30 bone samples. DEXA BMD data are not presented here since only the gold standard BMD values from physical calculations can give a true understanding of the relationships.

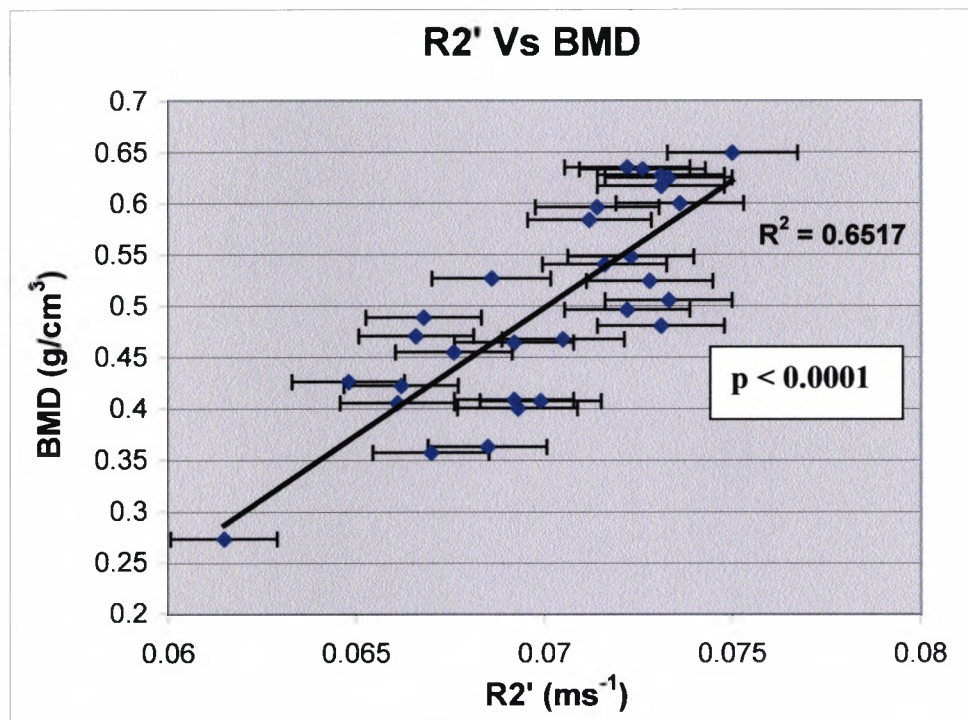


**Figure 4.8.** Relationship between  $R2'$  and BMD (gold standard) in 30 bone samples.

From figure 4.8 it can be seen that a positive correlation of  $R2'$  and BMD exists with  $R^2=0.6517$ . All the samples were scanned with the main trabecular orientation parallel to  $B_0$  in order to avoid contributions from the angular dependence demonstrated in the previous section (allowing true comparisons between all the samples).

---

From the results of this relationship it can be seen that the relaxation rate  $R2'$  increases with increased density of the trabecular structure. It can therefore be postulated that  $R2'$  is indeed related to BMD. Despite the strong correlation identified, however, it can be observed that  $R2'$  contains information other than the BMD since the correlation would have been much higher if  $R2'$  was a true measure of BMD.

As seen in chapter 3 (see figure 3.10), two samples with identical BMD values may have very different trabecular architecture (different trabecular plate thickness or separation) and this may cause different levels of magnetic susceptibility effects with a consequent effect on  $R2'$  decay rates. This phenomenon was observed by investigating the individual  $R2'$  decay rates of bone samples that had very similar BMD levels. Since all the samples were positioned in the magnet with the main trabecular orientation parallel to the main magnetic field, the deviation in  $R2'$  was assigned to a variance of the nearly perpendicular thinner supporting structures within the defined thicker trabecular orientation.

In addition, the angle experiments that were described in section 4.3.4 (that removed the effects of density) have also shown that  $R2'$  varies from factors other than density. The variance in  $R2'$  was, this time, related to the main trabecular orientation with respect to the  $B_0$  rather than (to a lesser extent) the near perpendicular supporting structures.

In order to test the hypothesis that  $R2^*$  may be different from  $R2'$  due to variations of  $T2$  between tissues, the relaxation rate  $R2^*$  (obtained using GE) was plotted independently against BMD (see figure 4.9). Since the same solution (water) was used for all samples in this study, such a variation was not expected and it can be confirmed from the results of this relationship. The small variation observed can be assigned to variable diffusion effects between samples, which could relate to the size of the spaces within the bone.

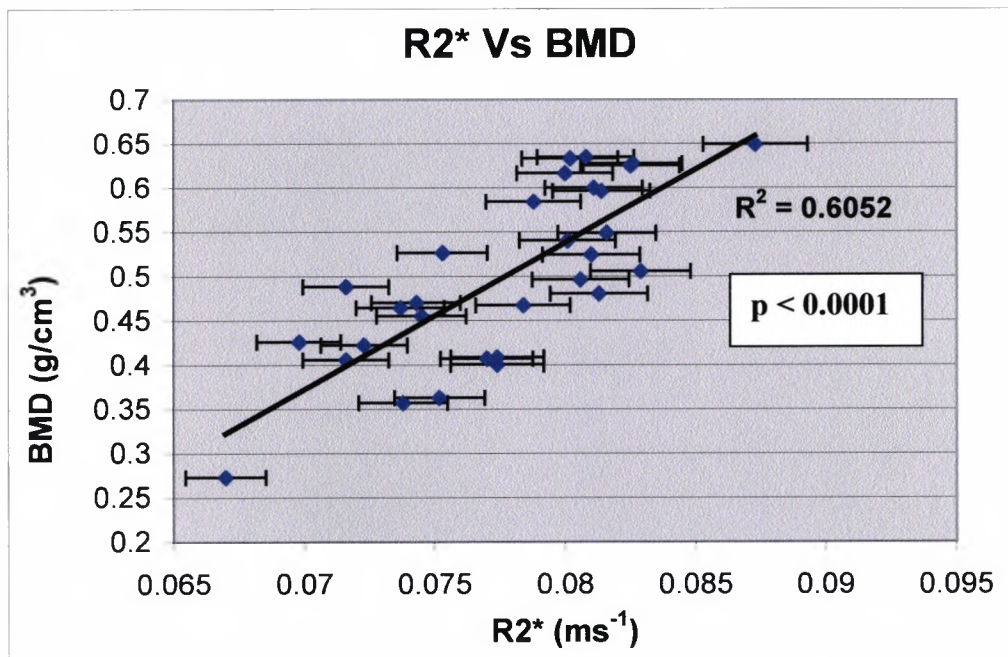


**Figure 4.9.** Relationship between  $R2^*$  and BMD (gold standard).

On the other hand, in order to assess whether  $T2$  itself was related to BMD, the  $R2$  relaxation rate (as obtained by SE) was also plotted against BMD (see figure 4.10).

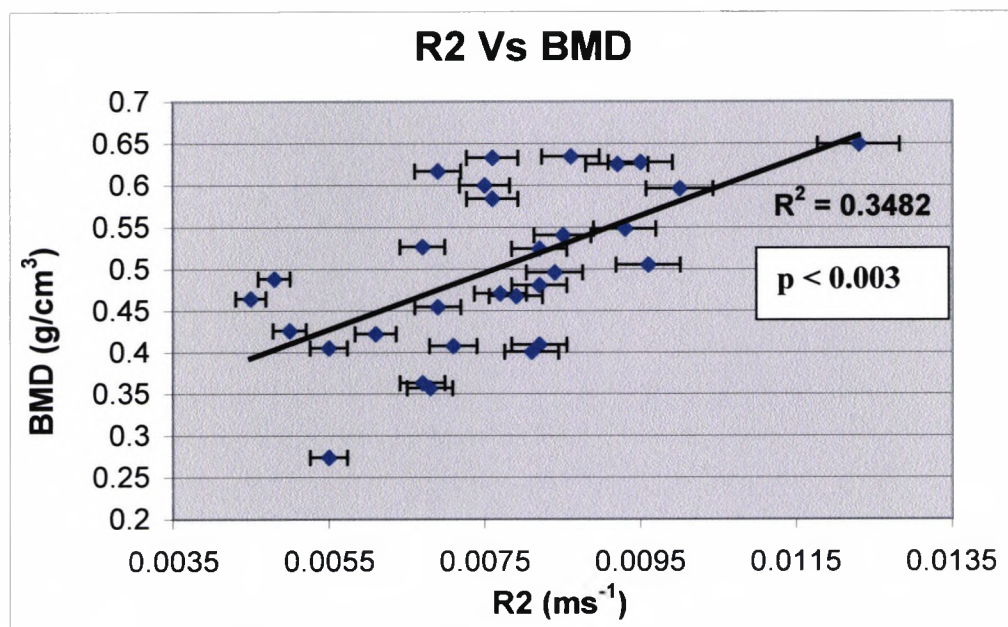


**Figure 4.10.** Relationship between  $R2$  and BMD (gold standard).

Figure 4.10 shows that there is a poor relationship between  $R2$  and BMD. This result was somewhat expected and can be explained by the ability of the SE to reverse the effects of magnetic susceptibility (180-degree  $RF$  pulse) caused by increased trabeculation.

#### 4.5.2 QMR and YM

So far, the results from the relationships between  $R2'$  and  $R2$  with respect to BMD have been presented. In order to assess whether any relationships exist between  $R2'$  and  $R2$  and the strength of bone,  $R2'$  and  $R2$  were plotted against YM. Figure 4.11 indicates the relationship between  $R2'$  and YM. From the results it can be observed that there was a fairly strong positive correlation between these two parameters with  $R^2 = 0.4834$ .

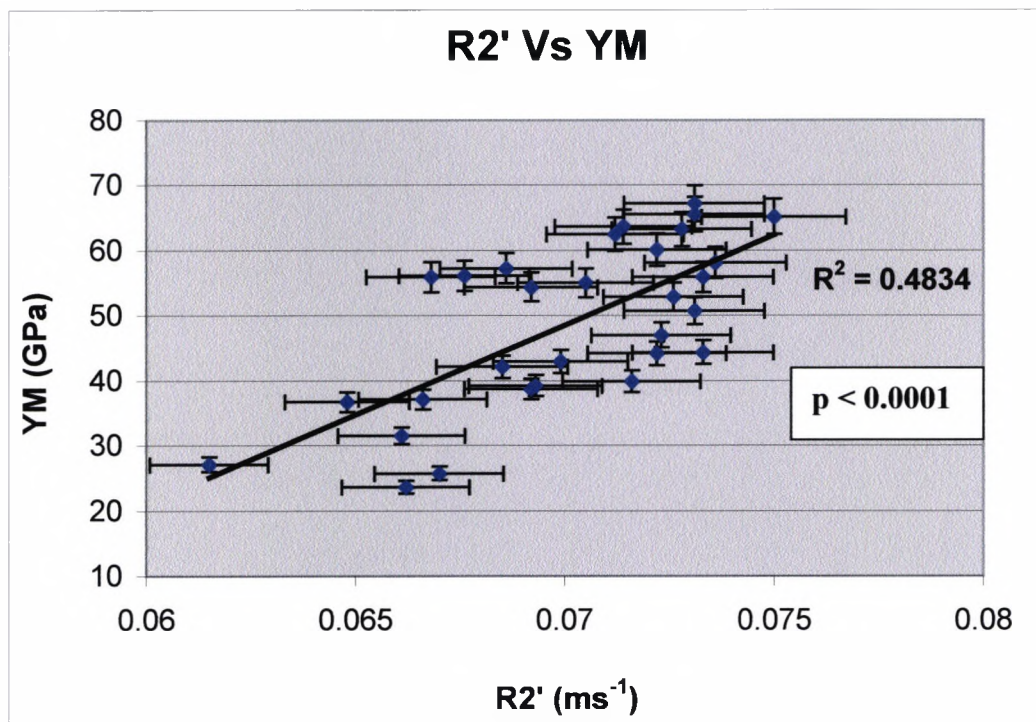


**Figure 4.11.** Relationship between  $R2'$  and YM.

Figure 4.11, however, suggests that  $R2'$  was not a strong enough correlate to bone strength to be used as a sole indicator of fracture risk.  $R2'$  correlates more strongly to the density of bone than to its strength as measured by the YM.

In order to investigate whether  $R2$  may be related to YM these parameters were also plotted against each other (figure 4.12). From the figure it can be seen that there was no correlation between these two parameters. This result was also expected since almost the entire signal is from water in the spaces between the bone. The  $R2$  of this water is unlikely to be related to either the structure or volume of bone within a sample and it is these factors that determine the YM of the samples.

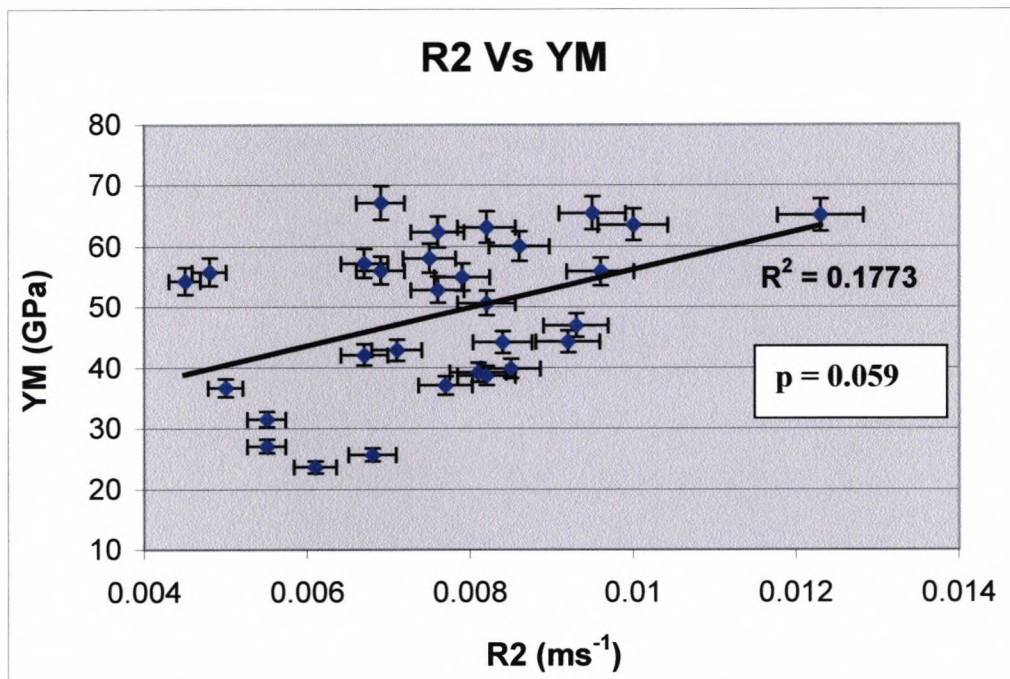


**Figure 4.12.** Relationship between  $R2$  and YM.

#### **4.6 Discussion**

The key questions raised in this chapter are: i) can QMR be used to estimate BMD and how do the results obtained in this work compare with previous findings? ii) Can QMR be used to assess bone strength and how do the results compare with previous findings? iii) What prospects are there for QMR to become an accurate and safe way of assessing bone in diseases such as osteoporosis?

---

#### 4.6.1 QMR and BMD

The results from this work have been shown to be in agreement with previous work in the field. Studies have employed similar methods to study bone samples extracted from various locations of the human skeleton ranging from vertebral bodies (Majumdar et al, 1991), the calcaneus (Remy & Guillot, 1998) and the head of femur showing relationships of  $R2^*/R2'$  Vs BMD of  $R^2=0.33 - 0.79$ . This study has demonstrated this relationship to be in accordance with other studies with a correlation of  $R2'=0.6517$ .

Although most previous studies were carried out using similar methods, the qualities that make this study unique are, i) the higher magnetic field strength (i.e. 7 T used whereas for all other studies the main magnetic field strength ranged from 0.6 - 5.88 T), ii) the large number of samples used (i.e. 30 samples used in this study whereas 3-15 have been reported in other in-vitro studies) and iii) the particular attention to the optimization of the QMR technique by the construction of special devices to allow for reproducibility that has not been addressed thoroughly in all other studies.

Despite the above difference all the studies that have been carried out have shown that BMD can have an effect on the decay rate  $R2'$ . However, it has been shown that  $R2'$  contains information not only regarding BMD but also regarding trabecular architecture. This effect was realised by observing the  $R2'$  decay rates of samples with very similar BMD values. Since all the samples were positioned with the trabecular orientation parallel to  $B_0$  (to allow comparisons), the variation in  $R2'$  between samples of similar BMD may be assigned to variability in trabecular architecture (i.e. trabecular separation or thickness).

This effect can also be demonstrated by performing experiments with the use of one sample and by rotating the main trabecular orientation at different degrees with respect to the main magnetic field ( $B_0$ ) in order to remove the effects of density. However, the variability of  $R2'$  in this case has been partly explained as a quantification of BMD along that direction (Brismar et al, 1999) in the following way. Assuming a bone sample with the main trabecular orientation (which constitutes the majority of total BMD) parallel to

---

$B_0$  and the near perpendicular supporting structures (which constitute the rest of the total BMD) perpendicular to  $B_0$ , the angular dependence may be valuable in quantifying BMD of the main trabecular orientation since, as the angle increases, the distortion of the magnetic field that affects  $R2'$  originates mainly from the main trabecular orientation rather than the supporting structures (Brismar et al, 1999). Although these investigators seem to believe that BMD can be extracted from this angular dependence, its applicability to in-vivo situations is questionable. Additional considerations that need to be addressed for in-vivo situations will be discussed in subsequent sections.

Although the investigations of  $R2'$  with respect to BMD have not been carried out at different magnetic field strengths in this study, a comparison of the data obtained in this study with other similar studies in the field has revealed that the correlations of  $R2'$  and BMD have not changed in favor of higher magnetic field strength as in the case of the 7 T scanner employed in this particular study.

#### 4.6.2. QMR and YM

Since trabecular density and architecture ultimately govern the biomechanical properties of bone, the relationship between  $R2'$  and YM has also been addressed. The results from this work have been shown to be in agreement with previous work. Studies have shown a fairly wide range of relationships of  $R2^*/R2'$  Vs YM with  $R^2=0.27 - 0.88$ . This study has demonstrated this relationship to be of  $R2'=0.4834$ . Although the results indicate that there is a correlation between the  $R2'$  decay rate and YM, this correlation is not high enough to allow for the technique to be used as a stand-alone method to predict bone strength.

#### 4.6.3 Translation of QMR to in-vivo situations

A number of in-vivo studies have been carried out for the investigation of the relationship between  $R2'$  and BMD. These studies, although limited, have reported correlations of  $R^2=0.50 - 0.66$ . However, the application of QMR in the clinical setting faces problems that have not been encountered with the use of bone samples and have not been addressed thoroughly in these preliminary studies.

---

Perhaps the most important consideration prior to the application of QMR to the clinical setting is the determination of the gold standard biomechanical properties of bone so that the QMR derived data can be compared with. Unfortunately, for most of the studies reported with the use of QMR in-vivo, DEXA was chosen as the technique for BMD calculations. As it has been seen from chapter 1, DEXA is characterized by a certain degree of inaccuracy when compared with in-vitro studies. Therefore, the potential value of QMR in the clinical setting cannot be assessed properly. Unless more accurate techniques for the determination of the true BMD in-vivo have been employed, the potential value of QMR in the clinical setting must be further investigated.

In addition, studies have consistently been using  $R2^*$  as a parameter of choice for the assessment of trabecular bone quantity and architecture. As shown from this study and various other studies,  $R2^*$  may be affected by variations in the  $T2$  relaxation time of tissue, which has not been observed to a great extent in this study since all the samples were immersed in the same solution (i.e. water). The composition of yellow marrow and red marrow in various locations of the human skeleton varies to an extent which may interfere with the estimation of  $R2^*$ . It can be suggested, therefore, that there is a pressing need for use of the  $R2'$  decay rate for in-vivo investigations in order to avoid  $T2$  influences from subject and anatomic location variability.

The ideal utility of QMR to in-vivo situations would be for the technique to offer BMD and trabecular architecture information in an effort to determine fracture prevalence. Unfortunately, a strength indicator (like YM) cannot be obtained in-vivo and the potential of the technique with respect to the determination of bone strength can only be assessed indirectly by analyzing the quantitative and structural information that can be extracted.

With respect to BMD quantification, QMR has been shown in-vivo to provide good correlations despite the limitations described above. However, with respect to architectural information, more work needs to be done. The angular dependence of  $R2'$  in-vitro has been shown to provide a possible quantification of BMD for the main trabecular orientation. However, based on the fact that only 23.2% of bone loss in

---

osteoporosis is related to the plate width of the main trabecular orientation whereas 67.6% is due to the thinner supporting structures (Weinstein & Hutson, 1987), the angular dependence on  $R2'$  may be of less significant importance at the present time. In addition, bearing in mind that this additional information cannot be obtained in the most important anatomic locations in-vivo (i.e. spine and femur), utilization of this angular dependence in the clinical setting becomes much more difficult. Perhaps the introduction of open magnets in future research in this respect may strengthen the potential of the technique.

#### ***4.7 Conclusion***

QMR has been presented as a new technique capable of providing information with respect to BMD and architecture of trabecular bone in-vitro. It has the advantage that it can be performed at medium to low resolution giving decreased acquisition times and permitting the use of scanners at clinically available field strength.

The results from this study have been shown to be in accordance with other studies that have been carried out in the field with the use of similar methods but without any notable improvements arising from the higher magnetic field strength used in this study. The  $R2'$  decay rate has been shown to provide a good correlation with BMD and to a lesser extent with YM. The potential value of the technique in-vivo has also been addressed and the issues of concern that may apply to in-vivo situations have been presented.

Based on the results from the in-vitro study that has been presented here and in the literature along with the issues of concern that apply to in-vivo situations, it can be suggested that, at present stage, QMR cannot be used as a stand-alone technique for the characterization of diseases such as osteoporosis. Perhaps the association of the information that can be extracted from QMR with other techniques in the future that offer complementary information (i.e. mean trabecular plate thickness, or mean trabecular separation) may provide a better understanding of QMR and its full potential may be uncovered. However, until data from such investigations are forthcoming, QMR in the routine characterization of osteoporosis must be considered investigational.

## ***Chapter 5: "Magnetic Resonance Microscopy (MRM) and its Value in the Investigation of Trabecular Bone"***

Micromorphology of bone has traditionally been assessed by means of optical microscopy or scanning electron microscopy but the destructive nature of the procedures has been particularly limiting (Chung et al, 1995). It is in the context of non-invasive assessment of trabecular bone architecture that recent efforts have been directed to the development of imaging techniques such as MRM. MRM is a non-invasive technique that provides high resolution images in arbitrary planes, as well as in three dimensions, and may be potentially useful for the characterisation of the trabecular network both in vitro and in vivo at various skeletal sites (Genant & Majumdar, 1997).

### ***5.1 Theory***

In human trabecular bone, trabecular thickness is of the order 100-200  $\mu\text{m}$  and intertrabecular spacings 300-600  $\mu\text{m}$  (Jara et al, 1993). MRM has its rationale in the acquisition of high resolution images to depict individual trabeculae (see figure 5.1). In this way changes in both the concentration and spatial distribution of trabecular bone may be studied more effectively by extracting the information directly from the acquired images.

As seen in chapter 2, the higher the resolution obtainable, the more accurate the representation of trabecular bone can be since, at lower resolutions, misrepresentation of the structure may occur due to partial volume effects (PV) with a concomitant negative effect on the characterization of the information extracted. Therefore, in MRM, it would be desirable to obtain the highest resolution images possible in order to secure a meaningful characterization of the structure.

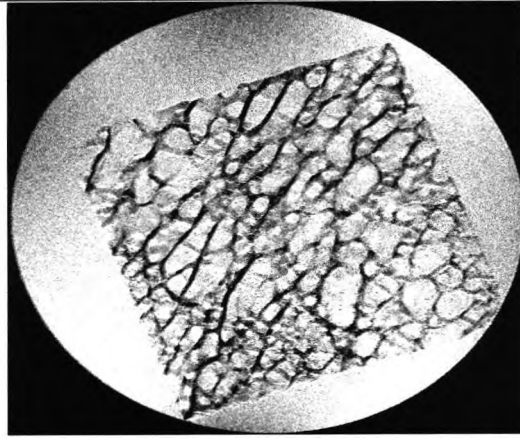


**Figure 5.1.** High resolution image of a trabecular bone sample. Trabeculae are demonstrated as black pixels (signal void) whereas water within the trabecular bone and outside the sample is demonstrated as bright pixels.

However, due to the large number of tissue parameters, imaging parameters and technical parameters that are involved in MRI (which can interact in multiple ways and affect the resultant image), a standard imaging protocol for use in all situations would be impossible to produce. Therefore, a task specific MRI protocol has to be designed and optimized if useful data is to be obtained and relied upon.

Perhaps the most important factor that governs the successful acquisition of useful high resolution MRI images is the achievement of a careful balance between signal to noise ratio (SNR) and spatial resolution within a reasonable examination time. However, in order to achieve this, a great number of factors have to be taken into consideration and will be described in subsequent sections individually.

#### 5.1.1. Magnetic field strength

A relatively wide range of magnetic field strengths have been used in MRI. The size of an MR system is expressed in terms of its magnetic field strength. A higher magnetic field strength produces higher MR signals, with the SNR theoretically increasing linearly with the field. Stark & Bradley (1992), indicate the relationship of SNR and magnetic field strength by,

---

$$\text{SNR} \sim \frac{\omega^2}{\sqrt{\alpha\omega^2 + b\omega^2}} \quad (\text{eq. 5.1})$$

Where  $\omega$  is the operating frequency and the factors  $a$  and  $b$  are constants that comprise, among other parameters, coil and object size. It is evident from the equation that as operating frequency increases, SNR increases. Although most of the whole-body MR systems in the clinical setting are operating at field strengths of 0.2-3 T, special purpose small bore magnets operating at higher magnetic field strengths are often used for research purposes. The advantage of higher SNR at higher magnetic field strengths may be traded for increased spatial resolution or decreased imaging time (described in subsequent sections).

#### 5.1.2 Hardware

The design of the receiving *RF* coil can play an important role in the reduction of noise (and hence the improvement of SNR). Usually the major source of noise is from the patient's tissue. Signal in MRI is inherently weak and *RF* coils that are as close as possible (and even contoured to adapt) to the tissue to be imaged are the best solution to this problem (Bronskill & Sprawls, 1993). *RF* coils available are usually categorized into volume and surface coils. Volume coils completely encompass the anatomy of interest whereas surface coils are good for detecting signal near the anatomical region of interest. While volume coils have been extensively used in whole body imaging, surface coils have recently found important applications in orthopaedic cases. Therefore, specific coil designs are found to have major SNR advantages for a given scanning goal.

#### 5.1.3 Imaging parameters

The image cycle repetition time *TR* is a factor that determines signal intensity. The signal level for a specific tissue is proportional to the level of longitudinal magnetization regrowth obtained at the end of each cycle. The level of longitudinal magnetization reached by the end of each cycle is determined by the relationship of *TR* to the *T1* relaxation time of the tissue. Although increasing *TR* will increase signal intensity, the

---

total scanning time will also increase. In addition, since signal intensity is also influenced by the relationship of  $TE$  to the  $T2$  values of tissue, the shorter the  $TE$  value selected the higher the signal intensity will be. Therefore, according to the nature of the tissue to be imaged, a careful balance between these parameters is necessary.

Another important factor that determines the acquisition of high resolution images is the appropriate selection of the voxel size. Two of the three dimensions of a voxel (i.e. the in-plane resolution) can be adjusted by the operator, simply by selecting the field of view (FOV) and the matrix size of a specific acquisition. On the other hand, the third dimension of the voxel can be adjusted (again by the operator) by selecting the slice thickness of a given imaging experiment. Signal strength is proportional to the volume of tissue contained in a voxel. The use of large voxels gives high SNR but reduces spatial resolution. Therefore, care must be taken not to compromise SNR in the pursuit of high spatial resolution, or vice versa.

Spatial resolution in the frequency encoding direction comes 'free' in terms of scan time (but not in terms of SNR) if the matrix is increased while the  $FOV$  is kept constant. A change of the matrix size in the phase encoding direction, however, requires more lines of data to be acquired which takes time according to: scan time = Number of excitations ( $NEX$ )  $\times$   $TR$   $\times$  Number of phase encoding steps (matrix size in the phase encoding direction).  $NEX$  is an averaging parameter that does not affect resolution but reduces the noise. However, from the above equation, scan time is affected by  $NEX$ .

#### 5.1.4 Pulse sequences

The type of pulse sequence used is also a major factor that may affect the acquisition of high resolution images of the trabecular structure. SE and GE based sequences are the most commonly used but with varying appearances due to the different mechanisms involved in the data collection scheme. As shown in chapter 2, the use of GE based pulse sequences may be advantageous in that lower  $RF$  power is deposited in the patient and may be quicker to perform in most of the cases. However, since the effects of magnetic

---

susceptibility are manifested more strongly in GE based pulse sequences, overestimation and underestimation of structures are more likely to occur.

As shown in chapter 2, in SE imaging the effects of proton dephasing due to susceptibility and magnetic field inhomogeneities can be reversed with the application of a 180-degree *RF* pulse whereas in GE imaging, these effects cannot be reversed with the gradient reversal. It can therefore be predicted, theoretically, that the selection of *TE* (particularly in GE sequences) may be of importance in the acquisition of high resolution images of trabecular structure. However, the selection of the minimum possible *TE* would be a reasonable measure to alleviate this problem.

#### 5.1.5 Image analysis

Provided the MRM images have been obtained by considering (and achieving a balance between) the above important factors, they may be used to calculate standard histomorphometry measures of bone structure by image segmentation and histomorphometric image analysis. Common histomorphometry measures in trabecular bone include bone volume fraction (BVF), mean trabecular thickness (Tb.Th) and mean trabecular separation (Tb.S), which may provide additional information regarding the strength of bone rather than the measure of BMD alone (Majumdar & Genant, 1995a).

In theory, bone area fraction (BAF) from a region of interest (ROI) can be extracted by summing the bone pixels and dividing by the total number of pixels in the ROI. This can be generalised to include all the slices from an acquisition (by performing the same operation on all slices) in order to obtain the bone volume fraction (BVF) of a volume of interest (VOI). Assuming the trabeculae are of elongated shape, the mean trabecular thickness in the image is approximately given by the area divided by half the perimeter length of the trabecular boundary (Chung et al, 1995). The mean trabecular separation (which is the measure of the marrow cavity pore size) can be measured as the mean distance between adjacent trabeculae. A full description of the extraction of this information can be given by investigating the different steps involved in image segmentation and histomorphometric image analysis individually.

Typically, the image is first segmented into bone and marrow phases, and histomorphometric analysis is then performed on the resulting binary image (a binary image contains pixels of value 0 or 1 only which correspond to black and white pixels, respectively). An intensity threshold is selected on the image pixel intensity histogram (see figure 5.2). The first peak corresponds to signal-free regions including bone and background and the second pertains to pixels containing protons in the marrow cavities.

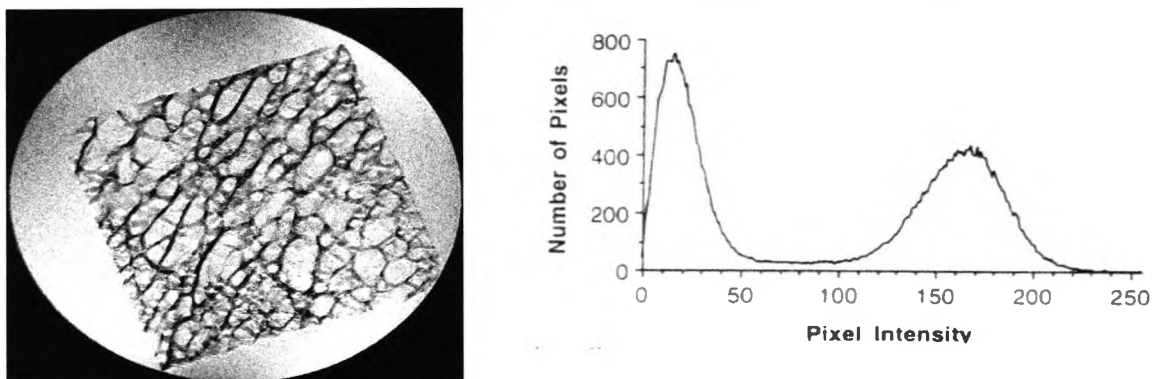


**Fig. 5.2.** On the left, a high resolution image of a bone sample is displayed and on the right, the corresponding intensity histogram (Chung et al, 1995).

The choice of the threshold value for pixel segmentation is specific to the characteristics of the histogram resulting from a magnitude MR image (Chung et al, 1995). This means that at voxel sizes far smaller than the trabecular thickness most voxels are occupied by either bone or bone marrow, leading to a bimodal intensity histogram as shown in figure 5.2 above. In this case segmentation is straightforward and a threshold can be selected to be at the midpoint between the peaks from bone and bone marrow (see figure 5.3).

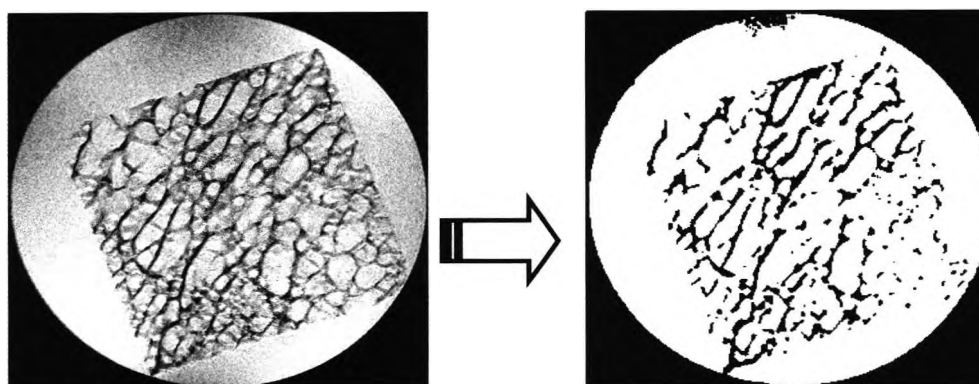


**Figure 5.3.** Binarization of a high resolution MR image by thresholding.

---

Noise, of course, broadens the histogram and so does partial volume averaging (PV). PV in this case (i.e. the case of trabecular bone) refers to a fractional occupancy of voxels by bone and marrow, as it occurs at decreasing resolution when voxel size becomes comparable to or exceeds trabecular thickness (see figure 5.4).

In cases of PV, the signal from within each voxel is averaged together and the intensity from each voxel is a combination of bone and bone marrow which result in a mono-modal image histogram making the threshold value identification and image segmentation a difficult task. A variety of approaches have been suggested to remedy this problem (which will be presented in the next section) in the low resolution regime which are based on complex statistical (or sometimes refer to as probabilistic) image processing algorithms but which can be potentially biased.

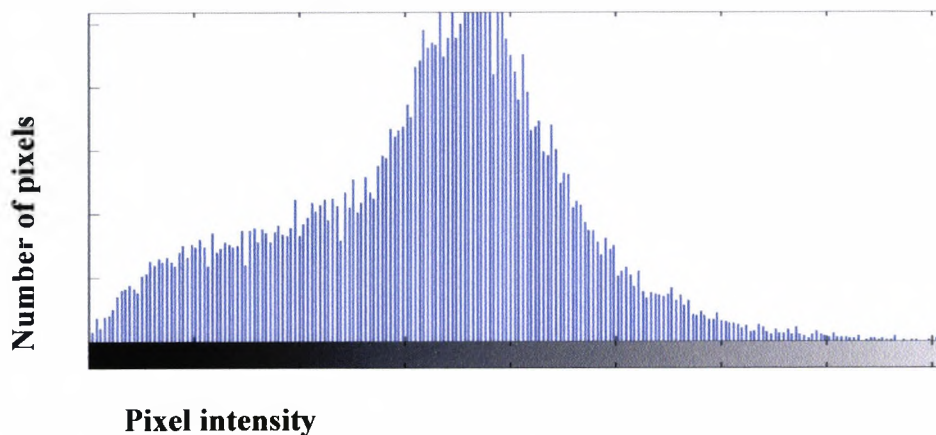


**Figure 5.4.** The effect of PV on the intensity histogram. This histogram can be compared with the histogram in figure 5.2 that was obtained at higher resolution in order to appreciate the effects of PV.

At the present time, there is no established technique for measuring the accuracy of any segmentation scheme and every thresholding scheme (at lower resolution) has some associated subjectivity that may be operator dependent or dependent on the automated criteria that are specified in an algorithm (Genant & Majumdar, 1997, p. 136).

Following segmentation (provided the image histograms are bimodal), single pixels of anomalously high or low intensity arising from noise can be eliminated by the application

---

of a filter to the binary image and clearly defined trabecular structure is present in the binary images suitable for histomorphometric image analysis by the measurement of common stereological parameters such bone volume fraction (BVF) mean trabecular thickness (Tb.Th), and mean trabecular separation (Tb.S). For demonstration purposes, the following description of histomorphometric image analysis is based on a bimodal intensity histogram.

As described previously, bone area fraction (BAF) can be calculated by adding the bone pixels of the binary image and dividing by the total number of pixels. The same operation can be performed on all slices from the acquisition in order to calculate the BVF of the whole sample. It should be mentioned, however, that the images are cropped to include the sample only. In order to calculate the mean trabecular thickness (Tb.Th), the total perimeter length of the trabecular boundary has to be identified which is the interface between trabeculae and bone marrow (i.e. between adjoining pixels of value 0 and 1 in the segmented image). Figure 5.5 below demonstrates this operation.

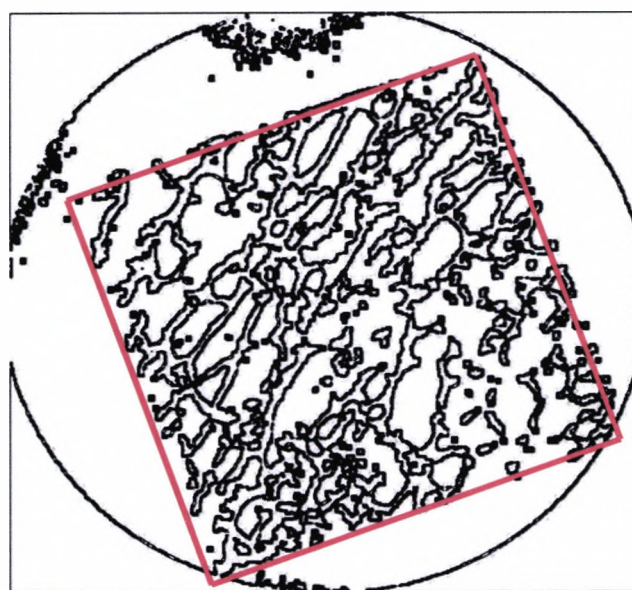


**Figure 5.5.** Trabecular boundary identification. The square marked in red indicates the final cropped image.

The mean trabecular thickness can be obtained by dividing the total area of the trabeculae by half the perimeter length (Chung et al, 1995).

---

Mean trabecular separation can be measured as the mean distance between adjacent trabeculae. Since in some cases (i.e. femur) the trabeculae can have a preferential orientation along the load bearing direction, the mean trabecular separation is usually a directional quantity. The measurement of this parameter can be performed by applying a grid of parallel test lines (and rotating this grid in increments of angle from 0-180 degrees) in the segmented image and calculating the average length of the lines in the marrow cavities along each increment (see figure 5.6). In this way, the mean Tb.S can be measured for the total area or volume independent of direction and also for each direction individually.

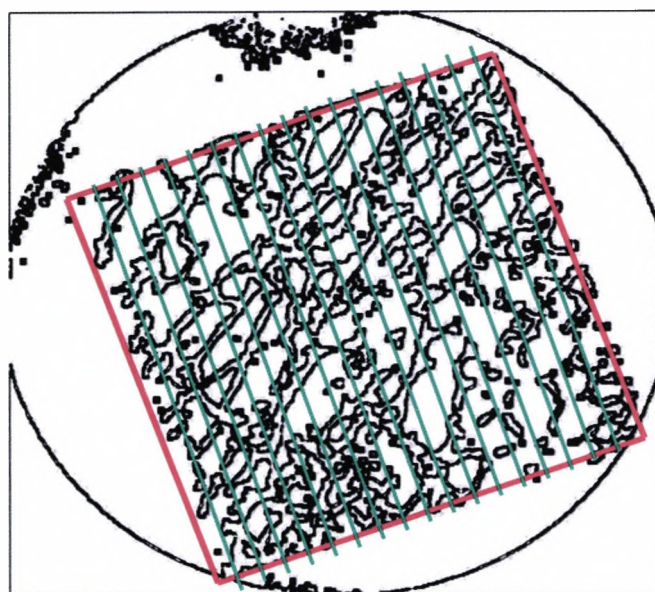


**Figure 5.6.** Method for calculating the mean trabecular separation.

There can be a variety of segmentation techniques and histomorphometric image analysis techniques that can be employed for the extraction of structural information from high resolution MRI images of trabecular bone. However, the method presented here is based on the work by Chung et al (1995), which seems to be the method of choice for a large number of investigators. Although deviations of this technique have been proposed, it can

---

be appreciated that, no matter which method is employed, standardization of a particular method in a large number of samples should still provide comparable results.

### ***5.2 A review of the studies with the use of Magnetic Resonance Microscopy***

There are many studies that have been carried out with the use of MRM for the assessment of trabecular bone structure in vitro. The majority of these studies were carried out with the use of very high magnetic field strengths and resolutions much higher than the structure to be imaged allowing for accurate characterization of histomorphometry features.

Hipp et al (1996) obtained 92 x 92 x 92  $\mu\text{m}$  resolution images (3D SE) of trabecular bone samples at 8.6 T and compared the extracted histomorphometry features with the ones extracted from optical imaging at 23  $\mu\text{m}$  resolution (gold standard). The total scanning time for the MRM experiments (per sample) was 50 minutes and 16 bone samples were studied. The chosen protocol in this study allowed clear bimodal image histograms to be obtained with consequent high correlations of all the histomorphometry features in their results.

Chung et al (1995) obtained 78  $\mu\text{m}$  isotropic resolution of bone cubes using three dimensional imaging at 9.4 T and found good correlations between MR derived parameters and gold standard histomorphometric measures. The authors suggested that only such high resolutions can provide accurate characterization of all histomorphometric measures in trabecular bone since measurements at lower resolutions are affected by PV.

In order to minimize scan timing at high magnetic field strength, Majumdar et al (1998) sought to investigate the effect of using different pulse sequences for the acquisition of MRM images of trabecular bone at 4.7 T. Using a specially designed phantom containing structure of known volume and dimensions (equivalent to trabecular bone dimensions), volumetric 3D GE and 3D SE were compared by acquiring identical scans (with resolution of 128 x 128 x 128  $\mu\text{m}$ ) and observing the differences in the MR derived morphological parameters compared with the gold standard. These authors observed that

---

3D GE was much faster to perform but the results obtained overestimated Tb.Th and underestimated Tb.S. This was assigned to magnetic susceptibility effects that could not be reversed with the use of 3D GE and affected the appearance and dimensions of the structure. Nevertheless, because of the ability of the technique to obtain high resolution data within reasonable scanning times, the authors suggested that this pulse sequence should still be used in MRM by reducing the echo time (TE) as much as possible in order to alleviate these effects. 3D SE was consequently regarded as inappropriate due to the long scanning times required to achieve a reasonable balance between SNR and resolution even at high magnetic field strengths.

Similarly, Jara et al (1993) examined the possibility of using two conceptually related variable-flip-angle 3D SE pulse sequences at high magnetic field strengths. The authors showed that these pulse sequences were found to be substantially less sensitive to distortions from magnetic dipole fields occurring at the boundaries of two phases of different magnetic susceptibility and offered similar results to 3D GE imaging.

While most of the MRM studies with the use of high magnetic field strengths sought to achieve accurate characterization of histomorphometry features from the MRM images, only a fraction of these studies addressed the actual value of these newly derived features with respect to bone strength prediction. Borah et al (2000) obtained 85 x 85 x 85  $\mu\text{m}$  resolution 3D SE MRM images at 4.7 T and compared the histomorphometry features with Young's Modulus (YM). The authors found that only the BVF could explain most of the strength in their bone samples (70-75%) whereas the other histomorphometry features could not provide useful information individually in this respect. However, by combining the BVF with other features in a multiple regression analysis, this significantly improved the predictability of bone strength.

A similar observation was made in the study by Wehrli et al (1998b). These authors obtained 48  $\mu\text{m}$  and 78  $\mu\text{m}$  MRM images of trabecular bone in vitro (excised distal radius) at 9.4 T. While 60% of the bone strength (as determined by YM) was explained by BVF, the rest 40% was assigned to the other common histomorphometry features. The

---

authors found that the number of the perpendicular supporting trabeculae (i.e. the thin trabeculae connecting the thick trabeculae that form the normal trabecular flow) provided complimentary information with respect to bone strength when combined with the BVF in multiple regression analyses.

MRM studies that have been carried out with the use of high magnetic field strengths in vitro have shown potential to provide information on both BVF and trabecular architecture. However, it was soon realized that further research in the field of MRM had to be directed at achieving equivalent results at lower magnetic field strengths if this technique was going to be utilised in the clinical setting. However, at the lower resolution regime it was realized that only high level image processing techniques could enable this transition. Image processing in MRM is currently an area that undergoes intense scrutiny in an effort to alleviate the effects of PV in resolutions achievable with the currently available clinical MR systems.

A study by Antoniadis et al (1999) sought to investigate the possibility of using a different method for image segmentation other than the conventional techniques such as thresholding (which only applies successfully to very high resolution data). The authors developed a probabilistic relaxation labelling technique which uses local features of the trabecular bone images to improve segmentation. Their technique showed that it may provide more accurate segmentation than thresholding at low magnetic field strengths, especially by preserving the connectivity of the trabecular network.

Wehrli et al (1998a) suggested a new technique that claims to obviate the need for threshold setting in the low resolution regime. The basis of this method is to iteratively deconvolve the actual histogram, which is achieved by resorting to a model histogram consisting of two  $\delta$ -functions (for bone and bone marrow, respectively) as a starting point. The model histogram is first convolved with Rician noise and compared with the experimental histogram, and the error between the two histograms determined. Subsequently, the error is subtracted from the initial estimate and the process repeated until the error has fallen below a predetermined threshold. Finally, the histogram

---

intensities are assigned to the image pixels on the basis of the probability of a pixel to contain bone, and connectivity arguments. Nevertheless, the authors admit that this technique (i.e. the resultant noise-deconvolved images) still suffer from blurring due to PV.

In addition, Hwang & Wehrli (2002) have recently proposed a novel image processing technique that also claims to alleviate the PV in the low resolution regime. The “subvoxel processing technique”, as it is named, relies on two fundamental assumptions: i) smaller voxels are more likely to have high BVF and ii) bone is generally in close proximity to more bone. The algorithm’s starting point is the partitioning of each voxel into eight subvoxels. The algorithm enforces strict conservation of bone mass (i.e. the total BVF in the original voxel is merely redistributed among the eight subvoxels). The precise amount allotted to a subvoxel is determined by the amount and location of bone outside the voxel but adjacent to the subvoxel. Thus, bone tends to be sequestered in subvoxels that are closer to other bone.

Recently, a variety of studies looking into the value of MRM in the characterisation of trabecular morphology have also been carried out in-vivo. At clinical magnetic field strengths, Link et al (1998b) sought to investigate the trabecular structure of 50 patients (23 known osteoporotic and 27 non-osteoporotic) in the calcaneus at 1.5T and 195 x 195 x 500 micron resolution. A 3D GE pulse sequence was used and the standard histomorphometry features (i.e. BVF, mean Tb.S and mean Tb.Th) were calculated (by thresholding) in all subjects. The authors admitted that the resolution used was not sufficient to calculate the true histomorphometry features and therefore named their histomorphometry measures as “apparent”. Nevertheless, by comparing the findings of the osteoporotic and non-osteoporotic subjects they found statistically significant differences between the two groups and suggested that MRM of the calcaneus may still be a valuable tool for the characterization of osteoporotic and non-osteoporotic patients at lower resolutions. Of particular importance was the variation in BVF and Tb.S between the two groups (lower BVF and higher Tb.S in osteoporotic subjects) rather than the Tb.Th (which appeared to be similar in both groups). They postulated that their findings

---

matched the fact that perpendicular supporting trabeculae are lost preferentially in osteoporosis. However, they appreciated that (due to the low resolution used) if smaller trabeculae could have been picked up, Tb.S measures might have been different.

A similar study by Majumdar et al (1999) sought to investigate the value of MRM for the investigation of the distal radius at 1.5 T and 156 x 156 x 500 micron resolution. A 3D GE pulse sequence was used and the standard histomorphometry features were calculated by thresholding. The authors employed 39 subjects (20 known osteoporotic and 19 non-osteoporotic). By comparing the findings of the osteoporotic and non-osteoporotic subjects they found statistically significant differences between the two groups and suggested that MRM of the distal radius may be an invaluable tool for the characterization of osteoporotic and non-osteoporotic patients. The most significant differences between the two groups were found to be in the BVF and Tb.S measures (lower BVF and higher Tb.S in osteoporotic subjects) rather than the Tb.Th (which also appeared to be similar in both groups). However, the significance of these finding was much lower than similar studies investigating the calcaneus.

### ***5.3 Pilot studies – technical considerations***

As seen in previous sections, a large number of factors have to be taken into consideration if reliable high resolution data are to be obtained and relied upon. For this reason it was decided that prior to the investigation of all the trabecular bone samples, pilot studies had to be carried out for the optimization of the MRM technique.

#### **5.3.1 Technique optimization**

With respect to hardware and accessories, the same 7 T magnet was used in the pilot experiments and with the same custom-made imaging accessories that were described in the previous chapters. SE pulse sequences were not investigated for reasons that have been explained earlier. A 3D GE FLASH (Frahm et al, 1986) was employed and the MRM optimization was directed at identifying the appropriate imaging parameters to allow for a reasonable balance between SNR and resolution and at a reasonable scanning time.

A cubic phantom was made from plastic sides and had similar dimensions to the actual bone samples (i.e. 15 mm sided). Within the phantom a number of cylindrical strings (fishing line) were attached that had various dimensions ranging from 100-300 microns. The dimensions were deliberately selected to be in this range so that to simulate the mean trabecular plate thickness of around 100-300 microns (see figure 5.7). The cavity within the phantom was filled with water and degassed in a similar fashion to the trabecular bone samples.

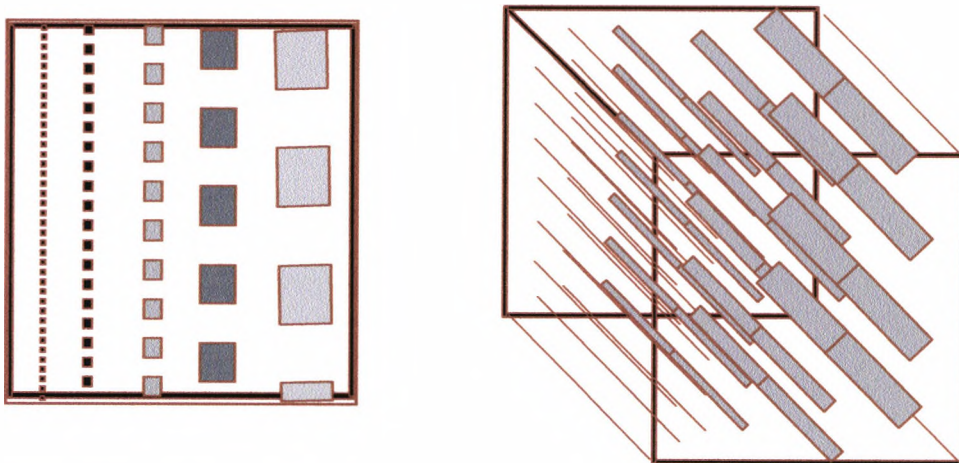


**Figure 5.7.** Schematic axial and oblique views of the phantom constructed for the pilot studies.

In view of the theory behind the acquisition of high resolution data, it was anticipated that (based on the small dimensions of trabecular bone) it would be impossible to obtain adequate resolution to probe structure (i.e. to obtain a true bimodal image histogram) within reasonable scanning time and a deliberate scanning time restriction should be imposed. The reason for this scanning time restriction was two-fold. Firstly, the scan timing should reflect the acceptable examinations times used in the clinical setting. Due to patient co-operation and satisfaction, coupled with the need to prevent motion artifacts in MRI, examination times beyond 10 minutes are usually unacceptable in the clinical setting. Secondly, the deliberate restriction in scan timing imposed here would allow high resolution images to be obtained equivalent to the ones achievable (or feasible) with the use of MR systems available in the clinical setting. The acquisition of higher resolution

---

images (by utilizing the full capabilities of the 7 T scanner used here) would serve no purpose in attempting to translate the results into the clinical environment.

Therefore, the optimization of the MRM technique was directed to conform with this restriction and a variety of pulse sequence combinations, imaging parameters and voxel sizes were investigated. The assessment of the performance of each acquisition was carried out by observing the SNR level and carrying out string area fraction (in a similar way to bone area fraction) calculations on each image of the phantom and from each acquisition.

SNR calculations were carried out in a similar way as described in chapter 3 (see figure 3.11) and the optimum SNR value was targeted to be between SNR=10-15 based on previous suggestions (Wehrli et al, 1998a). On the other hand, string area fraction was calculated by thresholding (i.e. using as threshold the value between the string and water peaks on the image histograms since a clear bimodal histogram was achieved with the use of the phantom). Due to the known number and dimensions of the strings within the phantom, the gold-standard string area fraction from each image and from each acquisition could be calculated and compared with the MR derived value. This enabled the determination of the most appropriate balance between SNR and resolution within 10 minutes scanning time.

### 5.3.2 Image processing

In order to investigate the optimized MRM technique that was derived from the phantom study, one bone sample was initially examined since the presence of more structure in the sample was expected to produce more PV and possibly interfere with the thresholding operation. Therefore, the investigation of one bone sample would assist in the optimization of the thresholding operation based on the resultant bone image histograms.

Figure 5.8 below demonstrates a high resolution image of the bone sample (using the optimized protocol identified from the phantom study), a cropped region to include only trabecular bone and the corresponding image histogram.

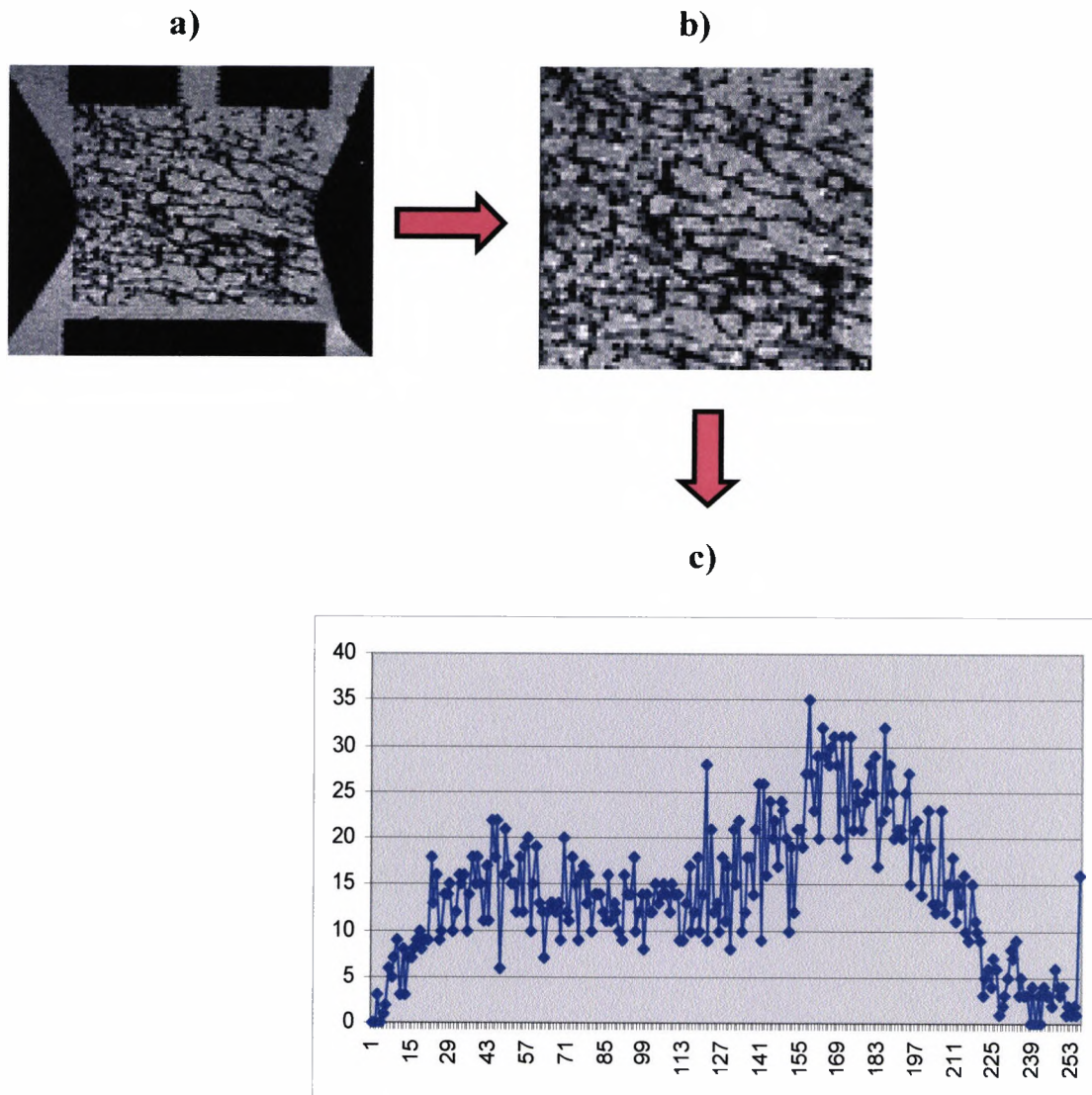


**Figure 5.8.** a) A high resolution image of a bone sample, b) a cropped region and c) the corresponding image histogram.

As it can be seen from figure 5.8 above, the resultant image histogram with the use of the optimized MRM technique did not allow a true bimodal histogram to be obtained for the bone sample. This was a result of the scanning time restriction that was imposed which did not allow higher resolution images to be obtained. However, it was decided that the optimized MRM technique could still be employed by optimizing the thresholding operation. This was done by analyzing the image histogram in a variety of ways to determine the best correlation between the BVF (extracted for the whole sample) and the

gold standard BMD (identified from physical measurements). The image histogram was analysed in two different ways. Firstly by identifying the mean signal intensity from the cropped image (in figure 5.8) and setting the threshold value to be that value and secondly, by applying a polynomial fit (6<sup>th</sup> order) on the histogram and identifying the maxima and minima from the fit (see figure 5.9).

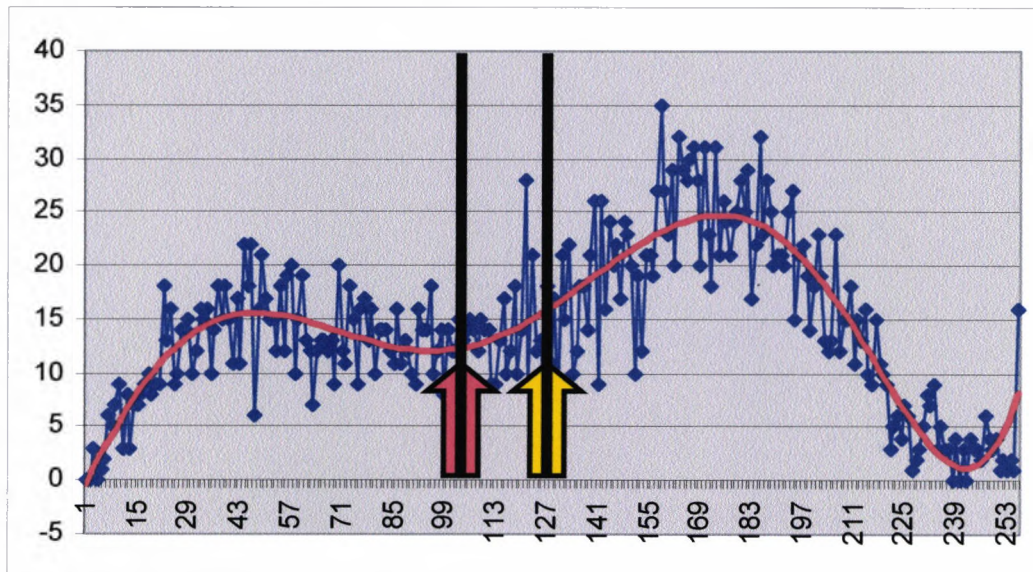


**Figure 5.9.** Identification of the threshold value from the image histogram in two different ways. The fit on the data (marked in red color) indicates a polynomial curve fitting of the 6<sup>th</sup> order. The red arrow displays the position of the minimum value between the two maxima on the curve (i.e. the tall peak represents water pixels and the lower peak represents bone pixels). The threshold value in this case was 106 on a 256 gray scale. The yellow arrow displays the mean signal intensity identified from the cropped image. The value in this case was 129 on the 256 gray scale.

The results from the histogram investigations revealed that the selection of the mean value from the cropped images offered better correlation between BVF and BMD in this case and it was decided that it should be used for the investigation of all the bone samples to follow. Therefore, a function in MATLAB 6.1 was developed which would perform histomorphometry analysis on the samples (in a way that was described in section 5.1.5) provided that a region of interest was specified by the operator. In this way, the image analysis on all the samples in the main study to follow would be carried out in a standard fashion allowing for reasonable reproducibility (also see next section 5.3.3).

---

### 5.3.3 Reproducibility assessment

Sources of error in the MRM technique were hypothesized to arise from the data acquisition stage and also from the image analysis operations. With respect to the data acquisition stage, errors were anticipated to arise from repositioning of the samples within the bore of the magnet. However, since the magnet and imaging accessories used in the MRM study were the same ones employed for the QMR study presented in the previous chapter, no additional investigations were deemed necessary in this respect and the same observations should be assumed. However, with respect to the possible errors arising from the image analysis operations, several experiments had to be carried out. It was anticipated that the only source of error arising in this case would be due to an inter-operator variability in the selection of the region of interest that the images were cropped for image analysis. Therefore, the same sample was analysed several times on separate occasions (i.e. one week gap in between) by specifying the region of interest to include as much of the bone sample possible each time. The percentage of errors (i.e. coefficient of variance - %CV) could be calculated from  $\frac{SD \times 100}{mean}$  where SD is the standard deviation and mean is the average value of the measurements. The results from these investigations revealed errors less than 0.6% for all histomorphometry measures

### 5.4 Method

All measurements were performed on a 7T, 12cm bore, Bruker Avance spectrometer running under Paravision 2.0. 3D images were acquired for the same 30 bone samples that were used in the previous chapter that had their gold standard biomechanical properties pre-determined (see chapter 3). A 3D FLASH (Frahm et al, 1986) sequence was used with a resolution of 195 microns in all directions (256x256x256 matrix, 5cm FOV, TR/TE=9.16/4.23ms, 30° flip angle). The MR scan parameters used were based on the pilot studies and optimized to produce adequate balance of SNR and resolution within 10 minutes scanning time. Although higher resolution images could have been obtained, it was decided that the investigations with the bone samples should be carried out in such a way so as to reflect the current resolution capabilities of clinical systems.

All the images for all 30 samples were processed with the software developed in-house using Matlab 6.1 (described in section 5.1.5). The BVF, mean Tb.Th and mean Tb.S were calculated in this way and compared with the gold standard biomechanical properties of the samples identified in chapter 3.

Apart from investigating the histomorphometry features individually with the gold standard biomechanical properties of bone, a multiple regression analysis was also carried out in order to determine whether the MRM derived histomorphometry measures could predict bone strength. Using multiple regression analysis, independent variables (i.e. BVF, mean Tb.Th and mean Tb.S) were analysed individually or in combination in order to determine how well they could predict the dependent variable (i.e. Young's Modulus).

### 5.5 Results

The graphs, including the linear fits and  $R^2$  values on the graphs were generated using Excel (Microsoft). The errors on the graphs were calculated from reproducibility assessments pertaining to each technique individually and are presented as two standard deviations.

Figure 5.10 below shows the relationship between MRM derived BVF and BMD derived from physical measurements on 30 bone samples.

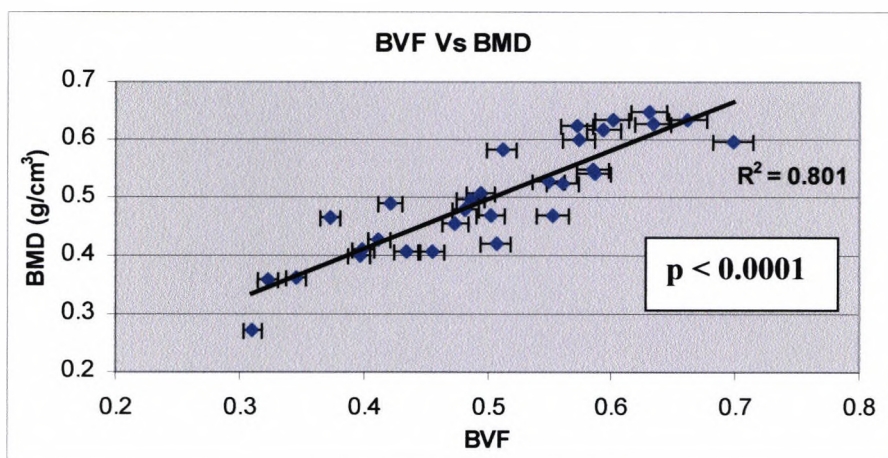


**Figure 5.10.** Relationship between BVF and BMD in 30 bone samples.

Figure 5.10 demonstrates a strong relationship between BVF and BMD in 30 bone samples with  $R^2=0.801$ . This indicates that BVF extraction from high resolution images may be a simple and valuable tool for the estimation of BMD. However, because of the scanning time restriction that was imposed for imaging the bone samples, this did not allow a clear bimodal histogram to be obtained which would have resulted in a stronger correlation. The resolution chosen in the imaging protocol was such that the results could be translated to MR systems available in the clinical setting.

A comparison of BVF with Young's Modulus (YM) of elasticity is shown on figure 5.11 below.

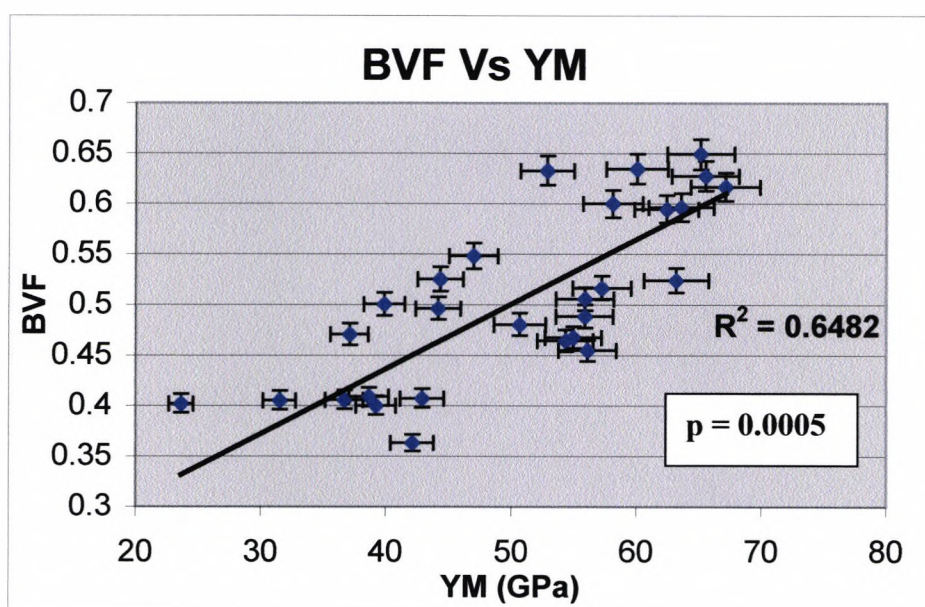


**Figure 5.11.** Relationship between BVF and YM.

The results from a comparison of BVF with YM above indicate a strong positive relationship of  $R^2=0.6482$ . Although strong, this result indicates that BVF can only partly explain bone strength and that additional parameters are responsible for the total strength of bone. This finding is in agreement with the relationship of the gold standard BMD and YM identified in chapter 3 with  $R^2=0.5817$ . Both results indicate that bone strength cannot be predicted with a measure of BMD or BVF alone and additional architectural parameters are involved. In order to investigate this hypothesis, the mean

Tb.Th and mean Tb.S were calculated for all 30 samples and are compared with YM in figures 5.12 and 5.13 below.

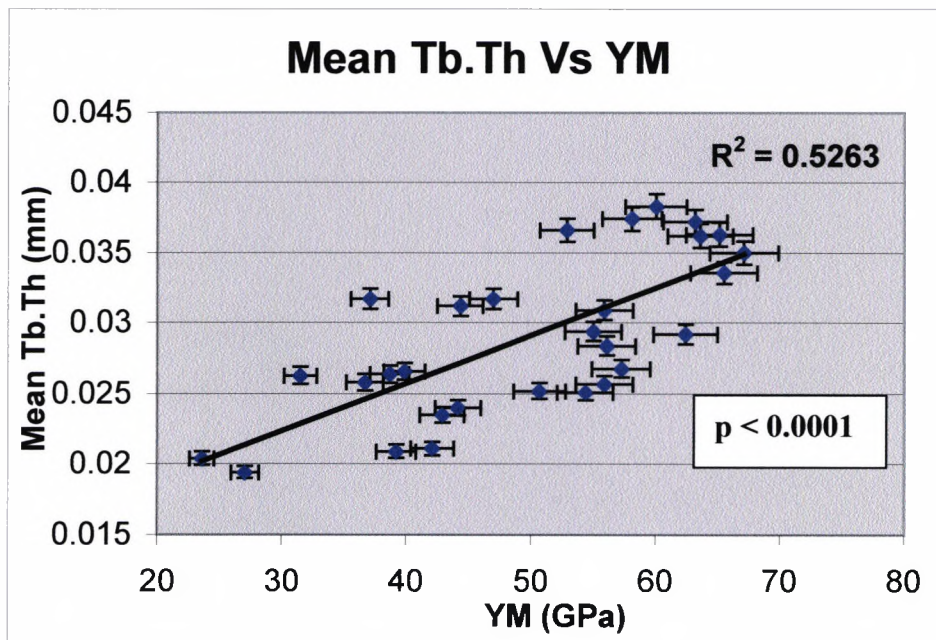


**Figure 5.12.** Relationship between mean Tb.Th and YM.

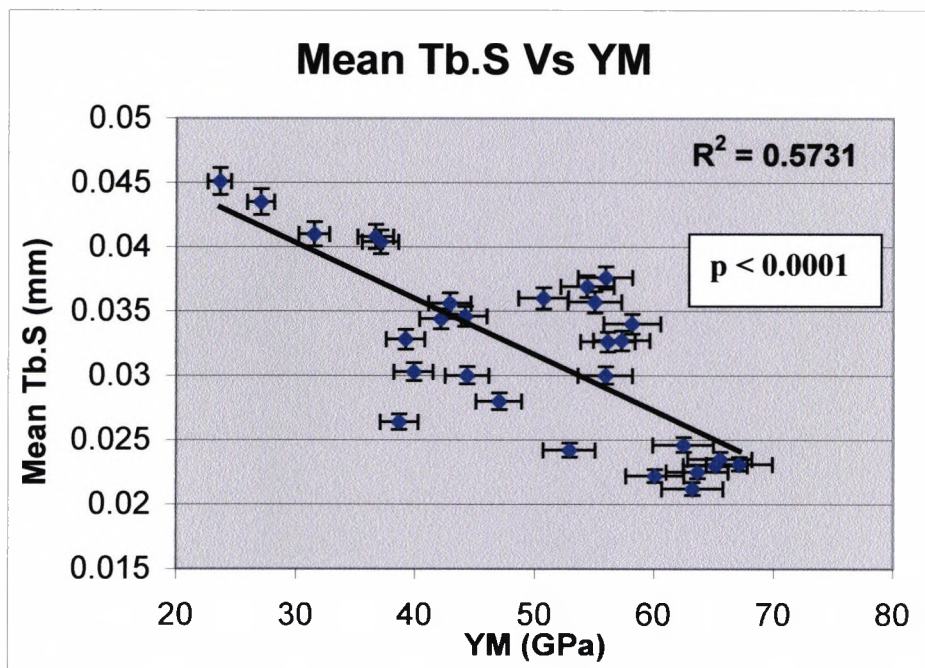


**Figure 5.13.** Relationship between mean Tb.S and YM.

Although strong correlations exist between mean Tb.Th and YM and mean Tb.S and YM from figures 5.12 and 5.13 above, these histomorphometry measures cannot be used individually to predict bone strength in this particular study.

In order to investigate the possibility of obtaining a better prediction of bone strength from a combination of the histomorphometry measures obtained in this study, a multiple regression analysis was carried out. From this analysis, a significant model emerged with  $P < 0.0005$  and adjusted  $R^2 = 0.657$ . Significant variables are shown on table 5.1 below.

<i>Predictor Variable</i>	<i>Beta</i>	<i>P</i>
BVF	0.530	$P < 0.0005$
Mean Tb.Th	0.023	$P = 0.002$
Mean Tb.S	0.331	$P < 0.0005$

**Table 5.1.** Results from the multiple regression analysis on 30 bone samples.

The adjusted  $R^2 = 0.657$  (which takes into account the number of variables in the model and the number of observations this model is based on) indicates that the model accounts for 65.7% of the variance in the dependent variable (i.e. YM). The beta value is a measure of how strongly each independent variable (i.e. BVF or mean Tb.Th or mean Tb.S) influences the dependent variable. The higher the beta value the greater the impact of the independent variable will be on the dependent variable. In this particular case, BVF had the biggest beta value whereas mean Tb.Th had the lowest.

In addition, the adjusted  $R^2 = 0.657$  increases to  $R^2 = 0.682$  ( $p < 0.001$ ) if the gold standard BMD is included in the multiple regression analysis. What can be observed is as follows: If higher resolution images are obtained with MMR (in the expense of longer examination times), the TbS and TbTh values become more accurate and so does BVF. Studies have shown that true TbS + true TbTh + True BVF in multiple regression analyses can predict up to 85-90% of YM (Homminga et al, 2002). However, in order to achieve these values, examination times in excess of 2-3 hours are required (and also

---

magnetic field strengths not currently tested in the clinical setting) which are unacceptable. The example above (i.e. that employed the gold standard BMD in this specific multiple regression analysis) has not greatly increased the prediction of YM since the TbTh and TbS values were calculated using a resolution that was not optimum (i.e. due to scanning time considerations).

## **5.6 Discussion**

The key questions raised in this chapter are: i) can MRM be used to estimate BMD and other common trabecular bone histomorphometry measures? How do the results obtained in this work compare with previous findings? ii) Can MRM be used to assess bone strength? How do the results compare with previous findings?

### **5.6.1 MRM and the estimation of common trabecular bone histomorphometry measures**

As it was described in the theory section of MRM, the higher the resolution achievable, the better the estimation of the trabecular bone histomorphometry measures can be. This is due to the reduction of PV (inherent to lower resolution images), which may influence the calculations of these measures in a negative way. However, the acquisition of high resolution images in MRI greatly depends on the use of high magnetic field strengths and long scanning times which are not acceptable in the clinical setting. Therefore, in order to obtain a more realistic understanding of the potential value of the MRM technique in the clinical setting, it was decided that the MRM technique used in this particular study had to be optimized and tested in such conditions so that to reflect the current capabilities of the clinical MR systems available. This was achieved by imposing a deliberate scanning time restriction and without utilizing the full potential of the 7 T scanner used.

Although a positive correlation of BMD and BVF was found with  $R^2=0.801$ , this was not strong enough to provide a true representation of BMD. If a deliberate scanning time restriction had not been imposed, a higher correlation would have been achieved strengthening, therefore, the overall value of the technique. Studies with the use of high magnetic field strengths and unlimited scanning times revealed much stronger correlations of MRM derived histomorphometry measures and the gold standard

---

measures obtained from serial sectioning. However, these studies did not suffer from the effects of PV and the information could be easily extracted by a simple thresholding operation.

The results from this study indicate that the utilization of MRM in the clinical setting at the present time greatly depends on the introduction of more sophisticated image processing techniques that may help to alleviate the effects of PV in the limited resolution regime. In this particular study, two simple methods of image processing were tested which provided varying but not optimum results. While a number of image processing methods have recently been suggested by some investigators, the real potential of these methods is yet to be fully evaluated. Due to the limited number of studies carried out in this field so far it is unsure which one of these methods may be the most valuable for use at the present time. Perhaps, further evaluation of image processing techniques in MRM along with the introduction of higher magnetic field strengths in the clinical setting may strengthen the potential of MRM in the estimation of the true trabecular bone histomorphometry measures.

#### 5.6.2. MRM in the assessment of bone strength

Perhaps the most important reason for the recent widespread investigations of trabecular bone with the use of MRM by many research groups is the realization of the potential ability of the technique to provide information not only regarding BMD but also regarding trabecular architecture. As it has been seen in chapter 3 and previous investigations, BMD can only explain bone strength to a certain degree whereas the rest of the strength remains hidden in the architecture of trabecular bone. In this particular study, BVF extracted from MRM images has been shown to relate to YM with a correlation of  $R^2=0.6482$ . This has been shown to be in agreement with the relationship of true BMD and YM obtained from physical measurements in chapter 3 with  $R^2=0.5817$ . Although the resolution used in this particular study was not optimum, it can still be appreciated that even if it was, the results would still not provide a better correlation than the one observed here. In fact, it would probably be lower as it would be

---

approaching the observed  $R^2=0.5817$  between gold standard BMD and YM from physical measurements.

In order to investigate whether common histomorphometry measures can provide a better prediction of strength (or complimentary information), these were plotted against YM individually. The results from these investigations revealed positive correlations of Tb.Th Vs YM and Tb.S Vs YM with  $R^2=0.5263$  and  $R^2=0.5731$ , respectively. In order to investigate the value of these findings, a multiple regression analysis was performed. The results from this analysis indicated that a significant model emerged which could explain 65.7% of the variation in YM if all the histomorphometry measures were combined. In addition, it has been shown that BVF and Tb.S are more likely to predict bone strength rather than Tb.Th since they had higher beta values. These findings are in agreement with other studies carried out at clinical field strength. The question arising here, however, is why all these histomorphometry measures combined together did not provide a better prediction of YM in this particular case? This can be explained by appreciating that the resolution used in this particular case was not optimum to allow for a better prediction of YM. In addition, studies have shown that the absolute bone strength prediction does not rely solely on these histomorphometry features and other parameters relating to the connectivity of trabecular bone are also being investigated which are not fully understood. What seems to be agreed at the present time, is that at optimum resolutions, the combination of BVF, mean Tb.Th and mean Tb.S in multiple regression analyses may be capable of predicting up to 85-90% of the variation in mechanical strength of bone (Homminga et al, 2002).

### ***5.7 Conclusion***

MRM is an exciting new technique for the investigation of trabecular bone. The greatest advantage of this technique is the potential ability to provide information not only relating to BMD but also regarding trabecular architecture. The results from this study have shown that, at resolutions achievable in the clinical setting, this technique cannot provide estimation of the absolute histomorphometry measures of trabecular bone since the obtainable images suffer from PV with a concomitant negative effect on the

---

histomorphometry analysis. However, further improvements in image processing techniques to reduce the effects of PV in the lower resolution regime might allow more accurate calculations of the histomorphometry measures which, in turn, will allow better understanding of the relationship between trabecular architecture and bone strength.

## ***Chapter 6: “Sub-Pixel Enhancement of Non-uniform Tissue (SPENT) and its value in the investigation of Trabecular Bone”***

A new method is presented which provides an original form of contrast based on the level of uniformity of magnetization distribution within a voxel. The original idea behind SPENT was aimed at resolving the issue of partial volume effects in a standard image in the low resolution regime, which would ultimately provide information on structure without the need of unacceptably long scan times. As seen in chapter 5, the most effective way for extracting and quantifying BVF with the use of MRI is by the acquisition of higher resolution images, which is proportional to the accuracy of BVF quantification. However, the higher the resolution obtainable, the longer the examination/experimental time, which makes it inapplicable at the lower magnetic field strengths currently available in the clinical setting.

While research groups focus on the development of high-level image processing techniques to probe structure that is smaller than the size of a voxel in the limited resolution regime (Fernandez-Seara et al, 2001 and Hwang and Wehrli, 2002), the work presented here concentrates on the development of more efficient acquisition schemes to serve the same purpose (Carmichael et al, 2002 and Carmichael et al, 2003). Over the last three years, experiments for the assessment of SPENT have been carried out at UCL Department of Medical Physics & Bioengineering. The use of specially designed phantoms to represent non-uniform structure along with computer simulations formed a major role in appreciating the potential value of the technique with respect to the investigation of trabecular structure (Carmichael, 2003).

### ***6.1 Theory***

SPENT can be described in terms of the k-space area sampled to create an image. In k-space the majority of the signal typically lies in the centre, where the main low frequency

---

features of an object are encoded. In higher frequency regions of k-space smaller details of an object are to be found, however, the SNR of this information is usually decreased. To image at the highest possible resolution, k-space is normally sampled up to the point at which no more useful information is acquired. Normally, all the k-space data is then Fourier Transformed (FT'd) to produce an image.

SPENT has its rationale in the utilization of specific areas (or 'tiles') of k-space in the higher frequency areas only (rather than all the data in k-space) in an effort to target specific information (see figure 6.1). These areas of k-space are FT'd separately and, on the resultant images, a  $2\pi$  phase wrap across each image pixel is imposed which means that signal in pixels is due to inhomogeneous voxels (edges between tissue types within a voxel) and dark pixels are due to homogeneous voxels. If the SPENT signal changes when there are more or less structures (i.e. edges), it might produce information relating to the structure contained within a sample (or region of interest) without the potentially biased image processing techniques usually used.

Figure 6.1 below shows which sections of k-space are utilized to extract the desired information. The shaded sections of k-space (in this case the x and y direction) are FT'd separately to obtain the SPENT images. Each shaded area of k-space has the same dimension as the central low resolution standard image.

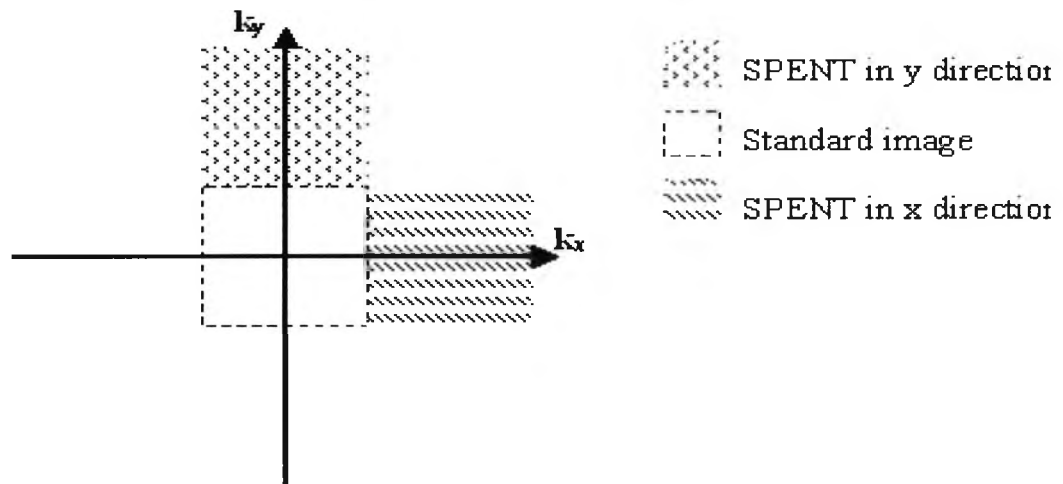


**Figure 6.1.** Shaded areas of k-space in the x and y direction that are used to produce SPENT images by applying FT only to these specific areas individually.

In the case of trabecular bone it is expected that each voxel will have a unique arrangement of bone and tissue (i.e. the edges of a particular voxel in the x, y or z direction will be different unless the voxel contains one type of tissue only). In theory, if SPENT images can be obtained in all three directions (i.e. x, y, z) and combined together they might produce a global measure of structure contained within a sample. From a spatial domain perspective, if an object contains some regular sized structures these will produce signal in a certain region of k-space. The smaller the size of the structures, the further out in k-space the signal will lie. Therefore, by sampling a higher region of k-space and reconstructing it independently the images are sensitised to the level of structure within the object.

### 6.1.1 Acquisition of SPENT – method 1

An extra gradient can be applied in any standard imaging pulse sequence in all directions individually (i.e. frequency, phase and slice direction – x, y, z, respectively). Figure 6.2 below demonstrates how an extra gradient is applied within a standard 2DFT Spin Echo sequence in the x direction.

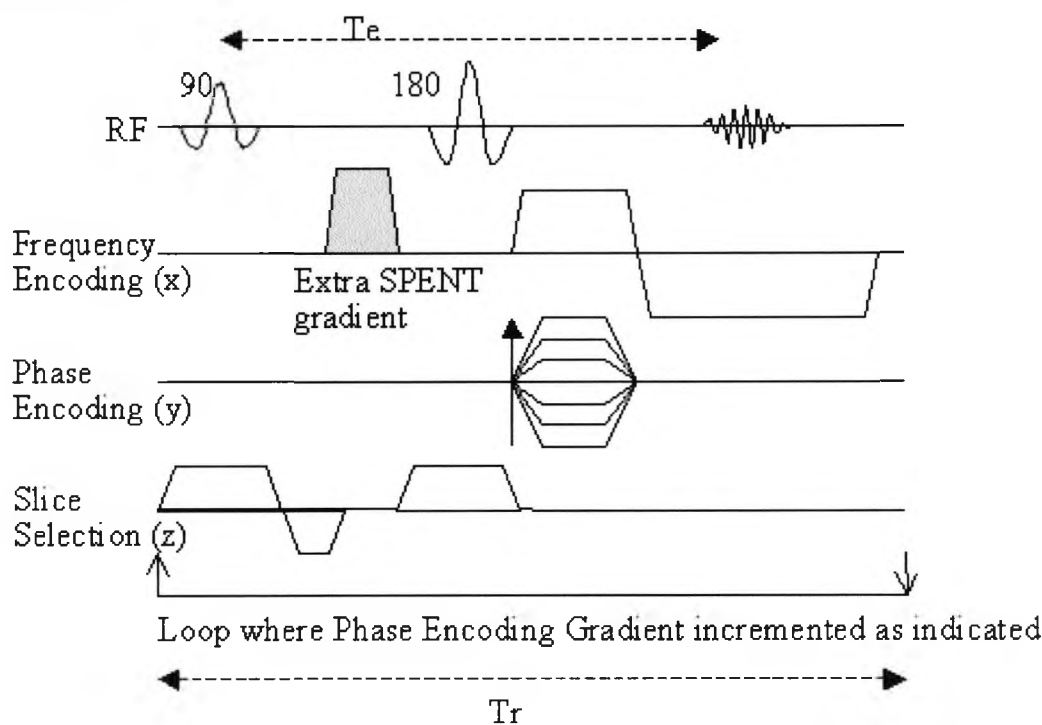


**Figure 6.2.** An extra gradient (shaded) is applied (in this case) within a standard 2DFT Spin Echo sequence and in the x direction only.

The application of an extra gradient in the x direction acquires the next tile along the  $k_x$  axis and the application of an extra gradient in the y direction acquires the next tile along the  $k_y$  axis (as shown in figure 6.1). The SPENT gradient can be applied in the slice direction as well to gain an idea on the level of voxel uniformity found in this direction. Therefore, the data for three SPENT images and a standard image could be obtained in four separate experiments.

### 6.1.2 Acquisition of SPENT – method 2

Another way of obtaining SPENT images is by extraction from a high resolution image data set by sub-dividing the k-space area in 9 separate tiles (see figure 6.3). In this way, 8 possible SPENT images (which will have 1/3 of the resolution of the high resolution image) can be extracted equivalent to the application of a SPENT gradient in the x, -x, y, -y, xy, -xy, x-y, -x-y, directions in addition to a central lower resolution image (central tile).

Provided that SPENT images (if combined) can give a direct measure of structure within a sample then this method can be generalised to include the slice direction from a separate SPENT acquisition in the z direction.

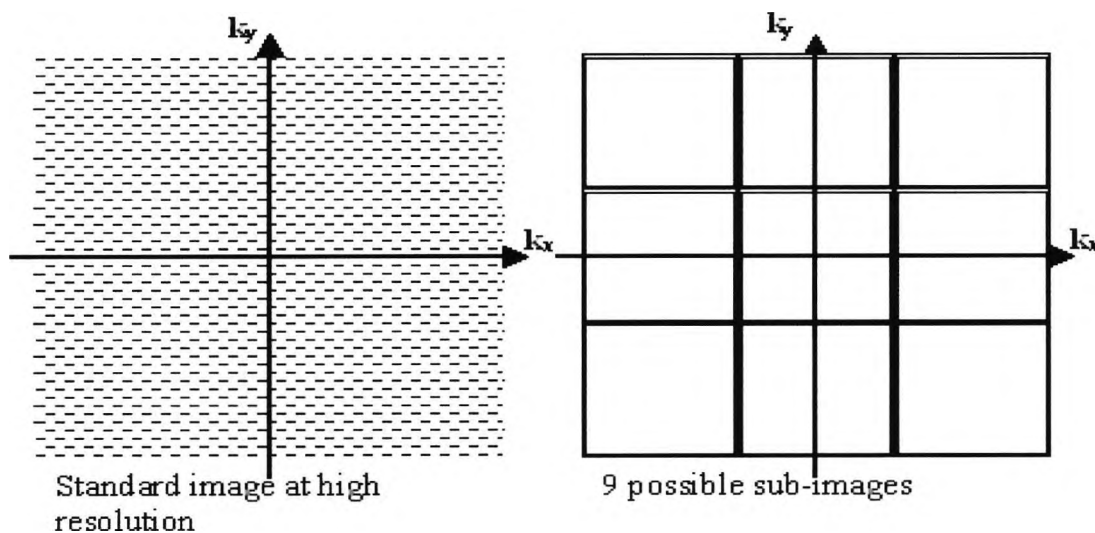


**Figure 6.3.** 8 possible SPENT images can be extracted from a standard high resolution image in addition to a central lower resolution image (central tile).

---

### 6.1.3 Acquisition of SPENT – method 3

Using the same principle as in 2D FT imaging, SPENT images may also be extracted from 3D data-sets that have previously been obtained using 3D acquisition techniques. This can be achieved by utilising certain sections of a full 3D k-space volume in order to investigate different resolutions (see figure 6.4).

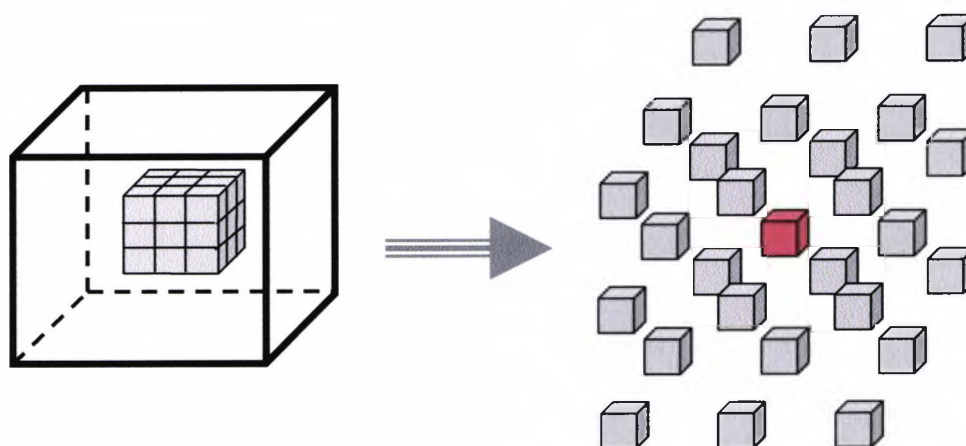


**Figure 6.4.** Extraction of lower resolution SPENT images from a high resolution 3D data-set.

A central portion of the full 3D k-space volume can be extracted which can have the resolution of preference. This sub-cube can be split into 27 further sub-cubes of data with a central sub-cube (shown in red color). The sub-cube in red color can be FT'd to produce a 3D standard image with 1/3 the resolution of the shaded volume shown on the left figure. The other 26 sub-cubes can be FT'd separately to form SPENT images in different directions. Therefore, it may be possible to analyse existing data sets without having to perform additional acquisitions. For example if 3D data sets are available for a set of samples from previous investigations, and SPENT investigations are anticipated to provide complimentary information, then no separate acquisitions are required since these investigations can be carried out by utilising the existing data sets.

The variety of options available for obtaining SPENT images (described above) offers potential time saving strategies since, based on the information that can be extracted from SPENT, the most appropriate and efficient method can be chosen for any given

---

experiment. In addition, potential time savings may also be traded for higher SNR by using more signal averages.

## **6.2 Pilot studies**

Based on the fact that there was no available information regarding the behavior of SPENT in trabecular bone imaging, it was decided that initially, pilot studies should be carried out with the use of a phantom. The same phantom that was used for previous investigations (see chapter 5, figure 5.7) was employed in the investigation of SPENT. The purpose of the phantom studies was to obtain an understanding of the behavior of SPENT with respect to structures of sizes equivalent to trabecular bone and to investigate various possible resolutions that the technique might perform best. As described in chapter 5, the phantom contained cylindrical rods of known volume and, therefore, a comparison of the signal obtained from the SPENT images and the known rod volume fraction could be made to assess their possible relationship. In addition, since the cylindrical rods were distributed in a parallel arrangement, the potential ability of the technique to provide information regarding orientation of structure would also be investigated by observing the signal obtained from the SPENT images with respect to the direction of the cylindrical rods.

The phantom was positioned in the magnet with the cylindrical rods perpendicular to  $B_0$  using the same sample holder and coil arrangement that was used in the previous investigations described. Initially, high resolution sagittal images were obtained in order to establish whether the phantom was uniformly filled with water and that no air-bubbles or other artifacts were present to interfere with the analysis.

With respect to the imaging parameters, sagittal SPENT images were obtained using a standard SE pulse sequence with a long enough  $TR$  (1500ms) and a short enough  $TE$  (23.5ms) to produce proton density weighted images of the water-filled phantom. The FOV used was 3.5cm and 16 slices of 1mm were obtained to cover the whole volume of the phantom. Matrix sizes of 128x128, 96x96, and 64x64 were used with the same parameters described above. Four separate experiments were carried out in order to

obtain the standard proton density images along with SPENT images in the x, y and z direction. Figure 6.5 below shows the images obtained at 3 different resolutions.

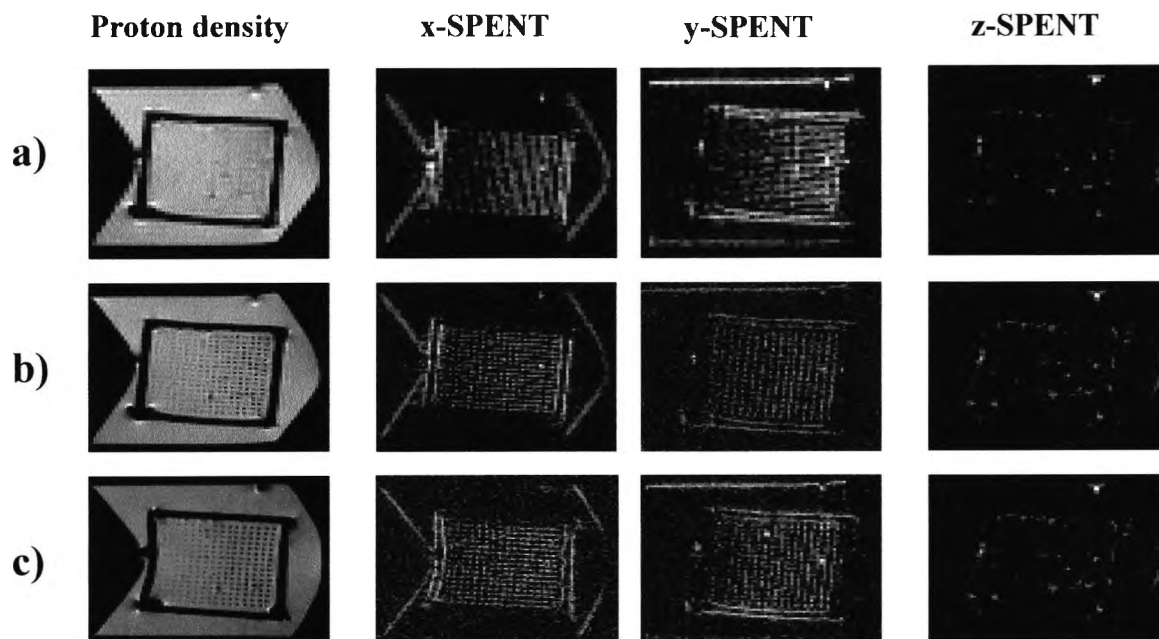


**Figure 6.5.** SPENT images in x, y and z directions at a) 64x64 b) 96x96 and c) 128x128 matrix size.

A visual inspection of the images in figure 6.5 shows that the 128x128 matrix acquisition offered better visual clarification of the structures in the phantom, which appear as bright dots with respect to the black dots seen in the standard proton density images. The SPENT images in the z direction offered no visual information on the images which is in accordance with the theoretical predictions since the extra gradient applied in the z direction is parallel with respect to the structure, providing homogeneity along that direction. On the other hand, the x and y directions contained a large number of edges which are shown on the resultant images.

In order to investigate the possibility of obtaining more information regarding the structure in the phantom (i.e. possible estimation of the rod volume fraction), the x, y and z directions for each resolution of the SPENT acquisitions were added together and

compared with the corresponding proton density images of the same resolution. Figure 6.6 shows this comparison.

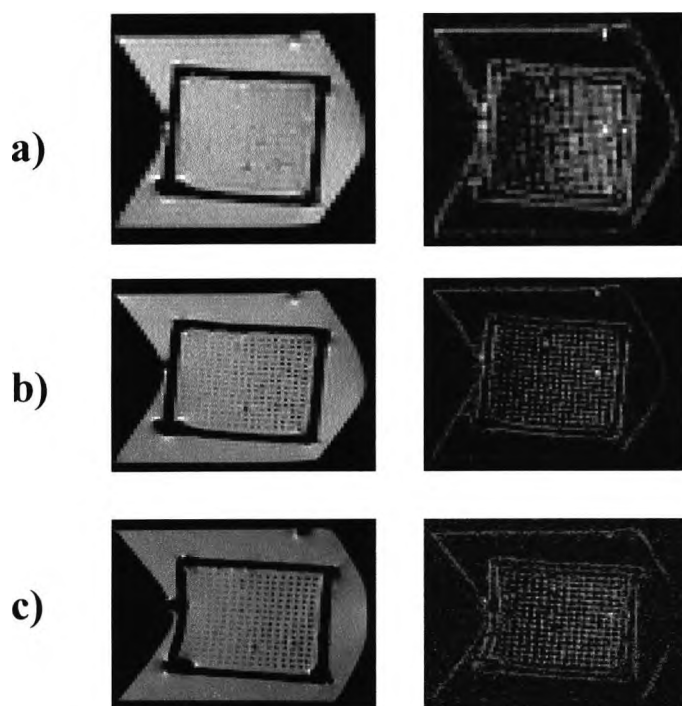


**Figure 6.6.** Proton density and  $x + y + z$  SPENT for a) 64x64 b) 96x96 and c) 128x128 matrix

A region of interest to include only the structure from the combined SPENT images (i.e.  $x+y+z$  SPENT) was cropped and the mean signal intensity was calculated for all 16 slices of each acquisition individually. The mean signal intensity of each slice was found to be the same for all 16 slices. This indicated that the mean SPENT signal was related to the amount of structure in the phantom since all slices contained the same known quantity of structure. In addition, by investigating different regions of interest (with different known quantities of structure), the mean signal intensity from the combined SPENT images was found to be highly correlated with the calculated rod volume fraction (gold standard). However, the level of correlation between the combined mean SPENT signal intensity and the calculated rod volume fraction was found to be slightly different at each resolution. This suggested that the combined mean SPENT signal intensity may provide an accurate quantification of the rod volume fraction but the accuracy of quantification

was related to the resolution used with respect to the structure dimensions. In this particular case, with the use of the phantom, the 128 x 128 matrix offered better results than the 96 x 96 and 64 x 64 matrices.

The results from the pilot studies with the use of the phantom suggested that the mean SPENT signal from the combination of all directions may be related to the quantity and direction of isotropic structure in a volume of interest at low resolutions. However, the behavior of SPENT signal with respect to anisotropic structure (i.e. trabecular bone) would still need to be investigated and is described in subsequent sections.

### 6.3 Method

SPENT images were obtained for 30 bone samples with the use of the 7 T system in different directions (x, y, z) with a low resolution, spin echo (proton density weighted), multislice sequence by applying an extra gradient in the desired direction to produce a  $2\pi$  phase wrap across each image pixel. The imaging parameters used were FOV=3cm, 96x96 matrix, 1mm slice thickness (16 slices acquired to cover the volume of the bone sample),  $TE=20\text{ms}$ ,  $TR=1161.9\text{ms}$ . Four separate experiments were carried out per bone sample; standard proton density image, SPENT in the x direction (x-SPENT), SPENT in the y direction (y-SPENT) and SPENT in the z direction (z-SPENT) with approximately 3 minutes scanning time per acquisition (see figure 6.7). In order to investigate the effects of resolution, separate experiments with the use of 128x128 matrix were also performed.

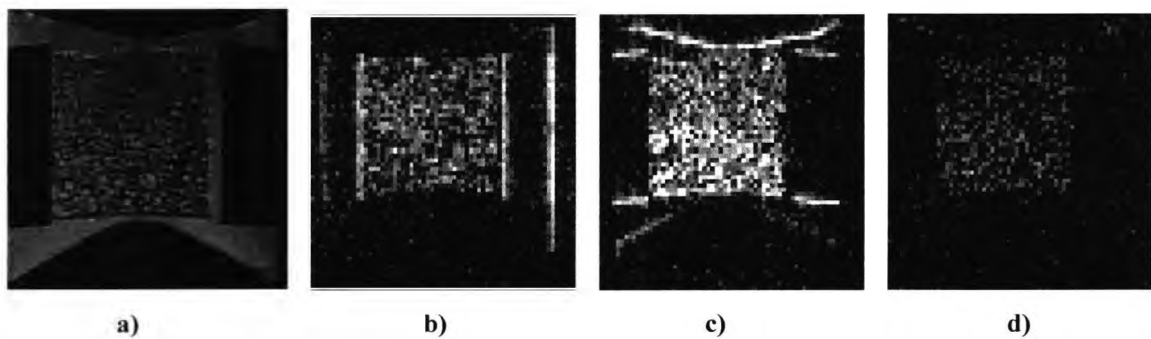


**Figure 6.7.** a) Standard proton density weighted image b) x-SPENT c) y-SPENT and d) z-SPENT. Note the edges of the container which correspond to the direction of the extra gradient.

### 6.3.1 Image analysis

A normalised-SPENT (NSPENT) image can be derived by dividing a SPENT image by the standard proton density image. In this particular study, proton density images are acquired and the division removes the dependence on proton density and coil sensitivity that is present in the SPENT image signal to obtain contrast dependent only on the level of sub-pixel uniformity (i.e. sensitising the images to structures such as edges).

In order to investigate whether the NSPENT images can provide a measure of structure within a volume of interest, a region of the object (or the whole object) was initially selected from the individual SPENT and standard images (see figure 6.8). The same operation was later performed on all slices from each acquisition in order to gather the NSPENT information for the total volume.

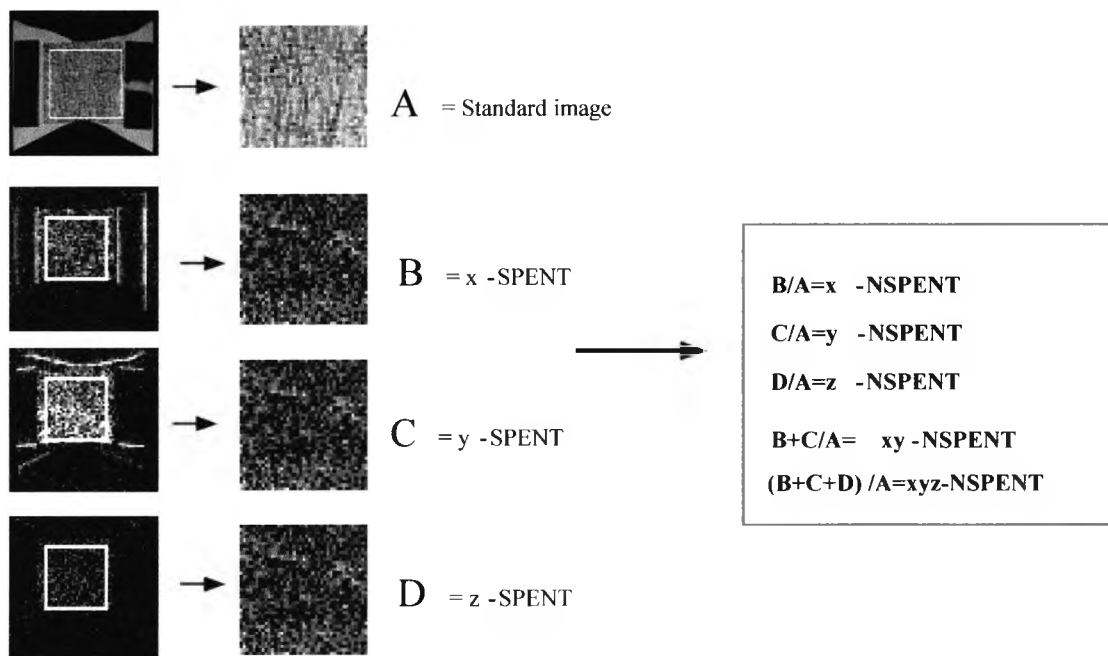


**Figure 6.8.** This figure demonstrates how the SPENT images are processed. Initially, a region of interest (ROI) containing only bone is cropped (from the same location in all images) from the standard proton density images (A), the x-SPENT (B), the y-SPENT (C) and the z-SPENT (D). By dividing each one of the SPENT images with the standard image, a normalized-SPENT (NSPENT) image is derived which can be averaged to measure the signal along that particular direction. In addition, the combination of x,y,z-SPENT images when divided with the standard image may provide a global measure of signal within the pre-specified ROI.

---

Software developed in-house using MATLAB 6.1 (Mathworks, Inc) was used to carry out calculations on the data from all 30 bone samples. The software was designed to perform the same operation on all 16 slices from each sample in order to calculate the average NSPENT signal from a whole volume of interest (VOI). This was performed for each SPENT direction individually ( $x$ ,  $y$ ,  $z$ ) and for all three directions combined ( $xyz$ ). In order to investigate the effect of resolution on the SPENT signal, the same process was carried out on data with the use of  $96 \times 96$  matrix and  $128 \times 128$  matrix for all 30 samples.

In addition, in order to obtain further understanding regarding the effect of resolution on the SPENT signal, the 3D data sets that were available from previous work (see chapter 5) were also processed using MATLAB 6.1 (Mathworks, Inc). The idea was to use different sized volumes of raw 3D k-space data to generate different resolution images (as described in section 6.1). The central portions of the 195 micron,  $256^3$  datasets were taken. This was performed for 4 different resolutions corresponding to the central  $255^3$ ,  $192^3$ ,  $126^3$  and  $66^3$  points in k-space. Each of these data cubes can be split into 27 further sub-cubes of data. The central sub-cube can be FT'd to produce a 3D standard image with 1/3 of the resolution. All the other cubes can be FT'd to obtain 3D SPENT images with a direction specified by the vector joining the centre of k-space to the centre of the 'SPENT' sub-cube. The resolution of the  $255^3$ ,  $192^3$ ,  $126^3$  and  $66^3$  k-space data cubes was 196, 260, 396 and 756 microns respectively (the FOV was 5cm in those particular acquisitions). The process of extracting lower resolution images from the 3D data sets was performed on 10 bone samples.

#### **6.4 Results**

30 samples of bone were imaged with SPENT. BMD was measured by weighing the samples and YM was measured using the stress test outlined in chapter 3. The NSPENT signal was calculated over a volume lying entirely within the bone cube and over the largest volume of purely bone possible. This process was performed for each SPENT direction ( $x$ ,  $y$  and  $z$ ) and for the combined directions ( $xyz$ ). The bone cubes were positioned so that the majority of their trabecular flow was in the  $x$ -direction. The graphs, were generated using Excel (Microsoft) and the error bars represent the results from the

reproducibility studies pertaining to each technique that were presented in previous chapters and are shown here as two standard deviations.

#### 6.4.1 SPENT and BMD

In figure 6.9, the average NSPENT value (for the 96x96 matrix) was plotted against the BMD for each sample. Each NSPENT direction is displayed using a marker of different color and shape.

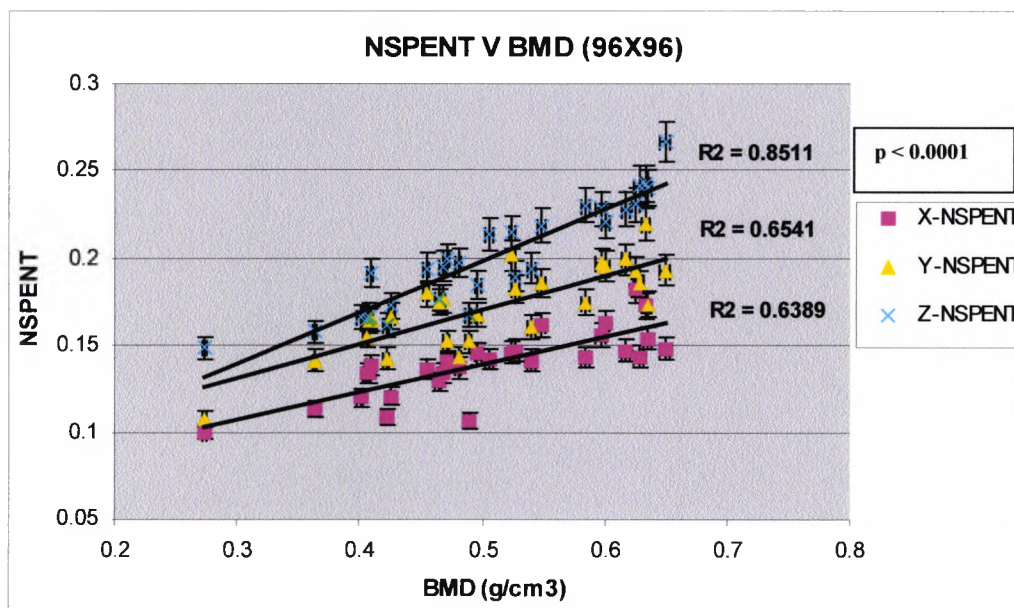


**Figure 6.9.** Graph of the mean NSPENT against BMD for each of the three directions that the NSPENT is applied in.

From the figure above it can be seen that the average NSPENT signal is highly correlated to the BMD in all directions. However, the individual NSPENT seems to behave in a different manner with respect to BMD which can be explained by appreciating the arrangement of the trabecular structure within the VOI. For example, the x-NSPENT seems to offer the lowest correlation with BMD in this particular case since the majority of the trabeculae within the volume were positioned along the x-direction (i.e. less edges) whereas a higher level of NSPENT signal has been observed in directions perpendicular to the trabecular flow (y and z). The z-SPENT gave the highest correlation from all the other directions which can be explained by the difference in the resolution in this direction (1mm slice thickness) from the in-plane resolution (312 microns).

The NSPENT signal from the different directions was also averaged to obtain an overall value (xyz-NSPENT). Figure 6.10 shows the averaged xyz-NSPENT signal plotted against BMD.

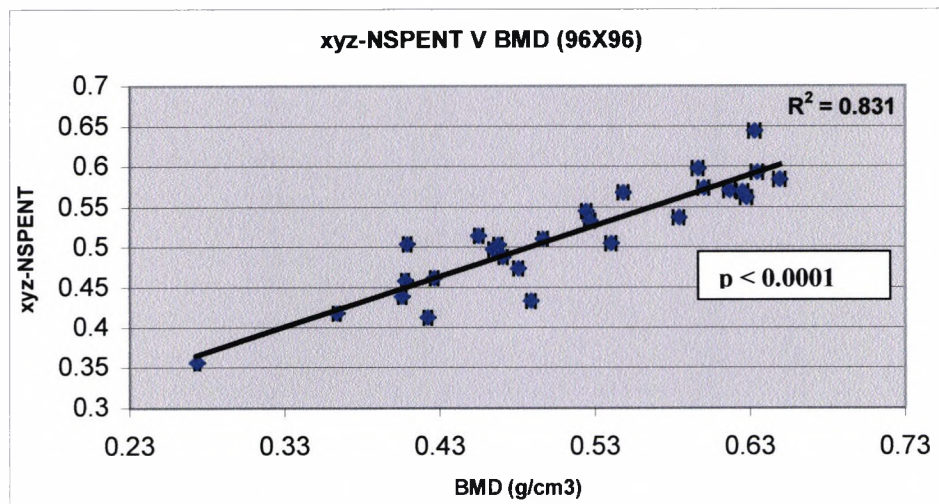


**Figure 6.10.** Graph of the averaged xyz-NSPENT versus BMD. The figure above demonstrates a very high correlation of xyz-NSPENT and BMD.

In order to further explore the potential of the technique, different resolution scanning was also performed. Figure 6.11 below shows the results of a similar analysis carried out on data acquired with the use of a 128x128 matrix.

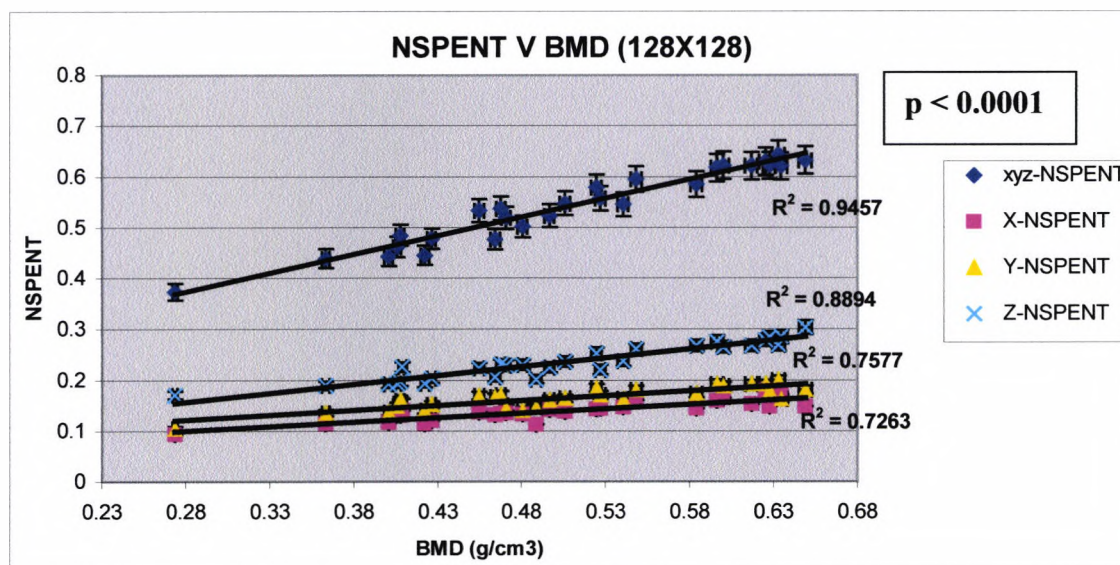


**Figure 6.11.** Graph of the mean NSPENT against BMD for each of the three directions that the NSPENT is applied in along with the xyz-NSPENT.

Figure 6.11 above demonstrates the mean NSPENT against BMD for each of the three directions that the NSPENT is applied along with the xyz-NSPENT with the use of 128x128 matrix. From the figure it can be seen that the individual NSPENT signal shows a similar pattern to the one observed with the use of 96x96 matrix. However, there is a higher correlation of the xyz-NSPENT with BMD in this case.

So far it has been shown that SPENT imaging may provide a simple tool for quantifying BMD in a bone volume of interest, since the xyz-NSPENT value relates highly to the gold standard BMD in certain instances. In addition (and perhaps one of the most important qualities of the technique), it has been shown to provide information pertaining to the architecture of the trabecular structure by investigating each NSPENT direction individually. Furthermore, the investigation of each NSPENT direction individually has been shown to offer not only an indication of the arrangement of structure within a volume but also a possible quantification of structure in each direction. However, the effect of resolution had to be investigated further in order to gain more understanding of its effect.

The resolution dependency of SPENT imaging was further explored by utilising the 3D data sets of 10 bone samples (that were used in previous investigations – see chapter 5) in a way that has been described in section 6.1. The results of all the resolutions obtained for 10 samples are compared with BMD on table 6.1 below.

Resolution (microns)	x-NSPENT	y-NSPENT	z-NSPENT	xyz-NSPENT
756	$R^2=0.2695$	$R^2=0.4757$	$R^2=0.6531$	$R^2=0.6394$
396	$R^2=0.3285$	$R^2=0.1812$	$R^2=0.2606$	$R^2=0.2997$
260	$R^2=0.4533$	$R^2=0.8301$	$R^2=0.5883$	$R^2=0.8402$
196	$R^2=0.3229$	$R^2=0.7543$	$R^2=0.6291$	$R^2=0.739$

**Table 6.1.** NSPENT signal Vs BMD for three different SPENT directions at different resolutions. In addition the xyz-NSPENT Vs BMD is also displayed.

---

Table 6.1 above demonstrates all the resolutions attempted for the investigation of the NSPENT signal Vs BMD from the 3D data sets. It should be noted that the results presented on the table were obtained from voxels of equal dimensions (the x, y, z dimension of each voxel was the same) whereas for the 312 micron (i.e. 96x96 matrix) and 234 micron (i.e. 128x128 matrix) results that were presented previously for the 30 samples, the z direction was different from the in-plane (i.e. 1mm slice thickness). Nevertheless, the results from these investigations on the 3D data sets still show some very interesting trends and are discussed below.

Firstly, the y and z directions displayed a higher correlation to BMD than the x direction (which is compatible to the investigations of the 234 and 312 micron resolutions previously presented), which can be regarded as a result of the positioning of the trabecular flow along the x direction (i.e. less edges). This was not true for the 396 micron resolution, however a low level of correlation has been observed for all directions at this particular resolution.

Secondly, the level of correlation between BMD and xyz-NSPENT was the highest for the 260 micron data. This is in accordance with the 234 micron resolution data previously presented ( $R^2=0.9457$ ) which may indicate that there is an increased level of SNR somewhere close to these particular resolutions. This suggests that further investigations may determine the ultimate balance for SNR Vs resolution, and consequently, performance in the case of trabecular bone.

Another interesting observation that can be made from table 6.1 is that the performance of the lowest resolution data (756 microns) was better than for the second lowest resolution data (396 microns). This suggests that even lower resolution data should be investigated since this trend may yield the technique even more feasible in the clinical setting and at lower magnetic field strengths.

#### 6.4.2 SPENT and YM

The NSPENT signal was also plotted against Young's modulus (YM) in the same way as for NSPENT with BMD. However, only the best resolution data at predicting BMD were employed here (128x128 matrix data) that were derived from the resolution experiments. Figure 6.12 below demonstrates the correlation between the average NSPENT signal in all three directions and the xyz-NSPENT with YM for all 30 samples.

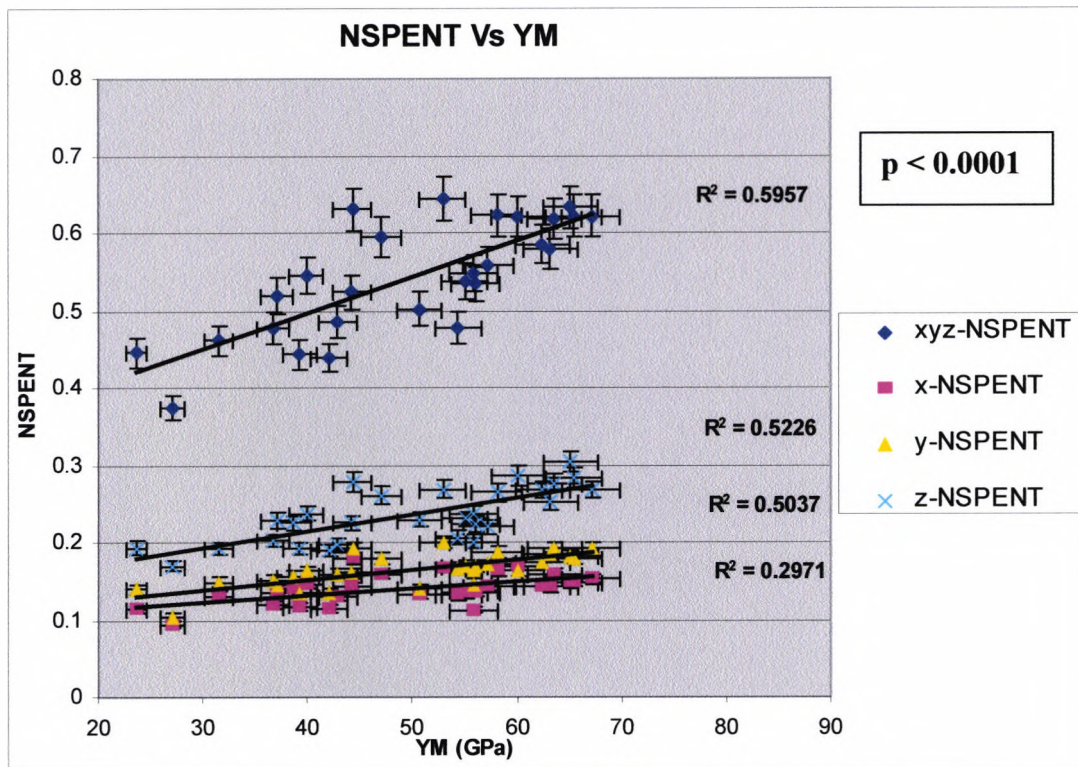


**Figure 6.12.** Graph of the mean NSPENT against YM for each of the three directions along with the xyz-NSPENT.

From the figure 6.12 above it can be seen that a positive relationship exists between the NSPENT signal and YM. However, the relationship is not as strong as in the case of NSPENT Vs BMD, which suggests that SPENT is more sensitive to changes in bone volume (BMD) rather than bone strength (YM). As it has been shown from previous chapters, the strength of bone depends not only on BMD but also on the trabecular architecture. For example, assuming two bone samples with identical BMD, their YM value will differ based on the arrangement of the trabeculae within their volume. This can be further supported by observing figure 6.13 below. The figure shows the relationship of

the gold standard BMD Vs YM as it has been assessed in this study on 30 samples in chapter 3 and is repeated here for demonstration purposes.

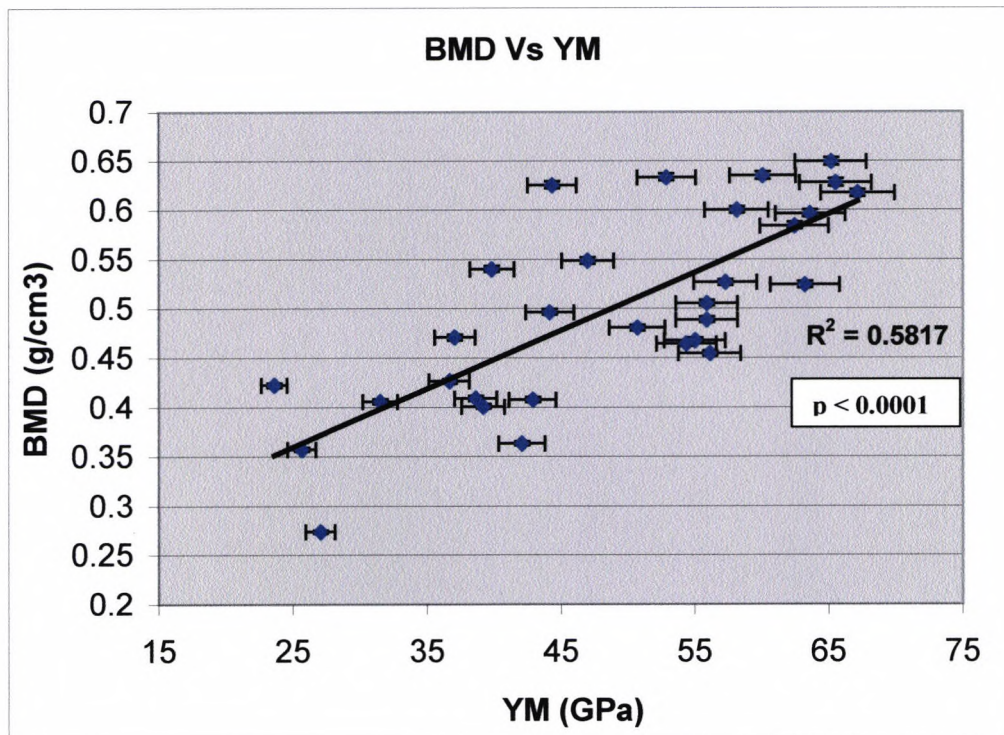


**Figure 6.13.** Relationship between BMD and YM on 30 samples.

From the figure it can be seen that although there is some correlation, BMD cannot be used as a stand-alone method to predict the strength of bone. However, what is of particular importance here is the fact that the xyz-NSPENT when plotted against YM gives a very similar correlation with the gold standard BMD Vs YM ( $R^2=0.5957$  and  $R^2=0.5817$ , respectively).

### 6.5 Discussion

SPENT has been investigated in this chapter with respect to its ability to provide information relating to BMD and bone strength with the use of 30 bone samples. Although additional investigations will be required in the near future to further evaluate the potential of this technique, the preliminary positive findings have been presented and are discussed in this section.

---

### 6.5.1 SPENT and BMD

The NSPENT signal averaged over a volume of interest correlated highly with BMD both in the individual NSPENT directions and in all directions combined together which suggests that SPENT may be a powerful tool for the quantification of BMD. The xyz-NSPENT gave the highest correlation with BMD while being independent of direction. This may be very useful in situations where the trabecular direction may not be known (i.e. the heel, the wrist or the spine). The BMD values in this study were calculated physically (as described in chapter 3) and therefore represent the true value (or gold standard) in these particular samples. The ability of the xyz-NSPENT to provide a correlation of  $R^2=0.9457$  means that there is a possibility for the technique to be employed and assessed in the clinical setting. Unfortunately, there is no technique available (at the present time) that can provide a true BMD value in-vivo and therefore, the calibration (i.e. the determination of the right balance of SNR Vs resolution) and assessment of xyz-NSPENT in-vivo will be challenging.

The investigation of the individual NSPENT directions also revealed high correlations with BMD. The highest correlation, however, was noted in the z direction in this particular case. This has been assigned to the fact that the z direction had a different resolution to the in-plane directions x and y. However, this may also indicate that only one SPENT direction may be necessary to obtain a reasonable estimation of BMD. If so, benefits in SNR and/or scanning time may be found by sampling smaller regions of k-space. In addition, the use of 1mm slice thickness for the z direction (at 7 T) may easily be translated in the clinical field and at lower field strengths.

The x-NSPENT has been shown to offer slightly lower correlations with BMD. This has been explained as a result of the positioning of the sample within the magnet, which allowed the majority of the trabeculae to flow along this direction. This resulted in less edges being present in this direction and consequently a lower correlation with BMD. This low correlation however, can be translated as an invaluable factor when attempts are being made to characterize the architecture of a less defined volume of interest. In addition, based on the fact that the arrangement of the trabeculae within a volume plays a

---

major role in the strength of the bone (i.e. perpendicular interconnecting plates are lost preferentially in osteoporosis and greatly affecting the strength), the individual x-NSPENT direction may provide a useful indication of these changes.

#### 6.5.2 SPENT and YM

Another interesting finding is the high correlation between xyz-NSPENT and YM, which matches the correlation between the gold standard BMD and YM. This indicates that while xyz-NSPENT provides a high correlation with YM, it cannot provide more information regarding the bone strength than BMD does. However, BMD cannot be accurately measured in the clinical setting and therefore, this may become the method of choice, replacing DEXA and its associated limitations (i.e. DEXA imparts a dose of radiation dose and also it cannot avoid contamination in its results from cortical bone and other tissue).

#### 6.5.3 Translation of the results into in-vivo situations

The findings from this study have demonstrated that SPENT imaging may be a simple tool in the characterization and/or estimation of BMD. However, the introduction and assessment of this technique in the clinical setting will require additional work pertaining to in-vivo investigations (at clinical field strength) and may even reveal obstacles that have not been encountered while investigating the bone samples.

The most important issue will be to identify the right balance between SNR and resolution. Not many problems are anticipated in this respect though, since SPENT has a number of advantages when compared to normal image acquisition. SPENT allows for a reduced area of k-space to be targeted with an associated time saving which can be easily traded for higher SNR. In addition, NSPENT images divide out coil sensitivity and receiver sensitivity, which could allow the use of surface coils to be used with a consequent enhancement of SNR. Also, since xyz-NSPENT has been shown to provide accurate quantification of BMD (independent of direction), other sites apart from the femur may be investigated which are equally important.

---

Perhaps the greatest challenge will be the identification of the true BMD values in-vivo that can be used to assess the SPENT technique. In addition, it would be impossible to quantify the strength of bone in-vivo since no method exists to provide a strength indicator like the YM. With respect to BMD in-vivo, pilot studies with the use of phantoms may be required initially. Alternatively, very high resolution 3D acquisitions can be performed on a few volunteers in order to extract the gold standard BVF that can be used to assess the value of SPENT in the clinical setting.

Finally, in the event of a successful application of SPENT imaging in the clinical setting the WHO criteria for the diagnosis of osteoporosis may have to be revised to conform with the information obtainable with SPENT. Since the SPENT signal is unlikely to be a direct measure of BMD, a reference SPENT value may have to be determined so that all examinations can be compared with for the characterization of osteopenic and osteoporotic individuals. However, due to the inherent complexity of MRI technology along with the variability of MRI systems currently available, it is unknown as to whether a standard routine protocol can be developed and used in longitudinal studies. Nevertheless, institution specific protocols may provide a possible answer to this issue.

## ***6.6 Conclusion***

In general, SPENT has been shown to be a simple and powerful tool that relates highly with BMD in-vitro. The resolutions needed for the SPENT technique to provide a reasonable estimation of BMD can be easily translated into in-vivo resolutions. In addition, due to the ability of N-SPENT in one direction to provide a reasonable indication of BMD along that direction, potential time savings can be achieved. More work will be required in the near future to convert the promising results presented here into equivalent in-vivo investigations.

## **Chapter 7: “Thesis Summary and Future Work”**

The main aim of this project was to investigate the value of MRI as a new and safe diagnostic technique in the characterisation of trabecular bone that would indicate whether MRI can be employed for the investigation of bone disorders like osteoporosis. QMR and MRM techniques have been investigated as a continuation of previous investigations. In addition, a novel MRI technique called Sub-Pixel Enhancement of Non-uniform Tissue (SPENT) was also investigated that has not previously been used with respect to bone imaging. All of the MRI techniques in this study were investigated in-vitro with the use of a large number of bone samples which had accurately predetermined physical and biomechanical properties in an effort to obtain a better understanding of the value of these MRI techniques.

In this last chapter a brief summary of the important conclusions from this work are presented. These conclusions are discussed with reference to future work arising from the findings. The three main projects presented in chapters 4, 5 and 6 will be examined individually.

### ***7.1 QMR in the investigation of trabecular bone***

QMR uses the fact that near the boundary of two physical phases of different magnetic susceptibility (in this case, trabecular bone and bone marrow), the magnetic susceptibility of trabecular bone is much smaller than the bone marrow. This causes spatial inhomogeneities in the static magnetic field which result in an alteration of the marrow relaxation times and properties which can be measured (Majumdar & Genant, 1995b).

#### **7.1.1 QMR in the investigation of BMD**

The results from this work have been shown to be in agreement with previous work in the field. Studies have employed similar methods to study bone samples extracted from

---

various locations of the human skeleton ranging from vertebral bodies (Majumdar et al, 1991), the calcaneus (Remy & Guillot, 1998) and the head of femur showing relationships of  $R2'$  Vs BMD of  $R^2=0.33 - 0.79$ . This study has demonstrated this relationship to be in accordance with other studies with a correlation of  $R2'=0.6517$ . Despite the strong correlation identified, however, it has been observed that  $R2'$  contains information other than the BMD since the correlation would have been much higher if  $R2'$  was a true measure of BMD. It can therefore be postulated that QMR cannot be used as a standalone technique for the estimation of BMD. Nevertheless, the strength of these findings warrant further investigations in the future directed at improving this technique while, at the same time, its potential to provide complimentary information should be further investigated.

#### 7.1.2 QMR in the investigation of fracture prevalence

Since trabecular density and architecture ultimately govern the biomechanical properties of bone, the relationship between  $R2'$  and YM was also addressed. The results from this work have also been shown to be in agreement with previous work. Studies have shown a fairly wide range of relationships of  $R2'$  Vs YM with  $R^2=0.27 - 0.88$ . This study has demonstrated this relationship to be of  $R2'=0.4834$ . Although the results indicate that there is a correlation between the  $R2'$  decay rate and YM, this correlation is not high enough to allow for the technique to be used as a stand-alone method to predict bone strength. However, further investigations in the future may allow for a better understanding of the information extracted with the use of QMR with respect to fracture prevalence (see next section).

#### 7.1.3 Future work

Perhaps the most important quality of QMR is the ability to provide information on both BMD and trabecular architecture in reduced examination times (i.e. acceptable in the clinical setting). In addition, its ability to provide useful information at clinical magnetic field strengths (as demonstrated by other investigators) strengthens the need for further investigations in the near future. Although, theoretically, the information extracted with the use of QMR should improve at higher magnetic field strengths, this did not seem to

---

be the case in this particular study with the use of 7 T. Therefore, it can be postulated that it may not be possible to use QMR as a stand-alone technique for the investigation of osteoporosis in the future even if higher magnetic field strengths are allowed to enter the clinical setting. However, future work can and should be directed at utilising the potential information extracted from this technique in association with other imaging techniques and that is only when its true value may be revealed. In addition, it is recommended that future work will involve investigations of QMR with respect to other important properties of trabecular bone (i.e. histomorphometry measures like mean Tb.Th and Tb.S) provided that these have been accurately predetermined. The strongest option would be to carry out serial sectioning on the existing bone samples and compare the findings with the existing QMR data. In this way, a better understanding of the QMR data will be achieved.

### ***7.2 MRM in the investigation of trabecular bone***

MRM has its rationale in the acquisition of high resolution images to depict individual trabeculae. In this way changes in both the concentration and spatial distribution of trabecular bone may be studied more effectively by extracting the information directly from the acquired images. Common histomorphometry measures in trabecular bone that are studied with MRM include BVF, mean Tb.Th and mean Tb.S. BVF is usually measured as an indication of BMD and the mean Tb.Th and Tb.S are usually used in combination with BVF (i.e. statistical models) in order to predict fracture prevalence.

Extensive in-vitro investigations by other investigators over the last decade have shown promising results particularly at high magnetic field strengths. It has been shown that the higher resolution achievable, the higher the diagnostic accuracy of MRM can be, which even matched the gold standard physical properties of trabecular bone samples in some instances. However, in the clinical setting, the resolution required to depict individual trabeculae is currently not possible and investigations focus on improvements of MRM such as to allow for equivalent information to be obtained at currently available clinical magnetic field strengths.

---

In this particular study, although a 7 T magnetic field strength was used, in-vitro experiments were carried out in a controlled environment such as to simulate the resolution achievable/feasible with the use of clinical scanners. In this way, the current true potential of MRM would be investigated and future technique improvements would be suggested based on the experience gained which are presented in this section.

#### 7.2.1 MRM in the investigation of BMD

In this particular study, a positive correlation of BMD and BVF was found with  $R^2=0.801$ . However, this was not strong enough to provide a true representation of BMD. If a deliberate controlled environment had not been imposed, a higher correlation would have been achieved strengthening the overall value of the technique. Studies with the use of high magnetic field strengths and unlimited scanning times revealed much stronger correlations of MRM derived histomorphometry measures and the gold standard measures obtained from serial sectioning. However, these studies did not suffer from the effects of partial volume (PV) found at low resolutions and the information could be easily extracted by a simple thresholding operation.

The results from this study indicate that the utilisation of MRM in the clinical setting at the present time greatly depends on the introduction of more sophisticated image processing techniques that may help to alleviate the effects of PV in the limited resolution regime (i.e. the clinical setting). In this particular study, two simple methods of image processing were tested which provided varying but not optimum results. While a number of image processing methods have recently been suggested by some investigators, the real potential of these methods is yet to be fully evaluated. Due to the limited number of studies carried out in this field so far it is unsure which one of these methods may be the most valuable for use at the present time. Perhaps, further evaluation of image processing techniques in MRM along with the introduction of higher magnetic field strengths in the clinical setting may strengthen the potential of MRM in the estimation of the true BVF and trabecular bone histomorphometry measures.

---

### 7.2.2 MRM in the investigation of fracture prevalence

As it has been seen in chapter 3 and previous investigations, BMD/BVF can only explain bone strength to a certain degree whereas the rest of the strength remains hidden in the architecture of trabecular bone. In this particular study, BVF extracted from MRM images was shown to relate to YM with a correlation of  $R^2=0.6482$ . However, studies have shown that, at optimum resolutions, histomorphometry features like BVF, mean Tb.Th and Tb.S may be capable of predicting up to 85-90% of the variation in mechanical strength of bone if combined in multiple regression analyses (Homminga et al, 2002). In this particular case, the results from such analysis indicated that, although a significant model emerged, this could only explain 65.7% of the variation in YM. Therefore, it can be postulated that, at resolutions currently available in the clinical setting, only similar relationships that have been observed in this study can be expected which are, nevertheless, much higher than the ones obtainable with the use of other imaging techniques.

### 7.2.3 Future work

MRM is an exciting new technique for the investigation of trabecular bone. The greatest advantage of this technique is the potential ability to provide information not only relating to BMD/BVF but also regarding trabecular architecture. The results from this study have shown that, at resolutions achievable in the clinical setting, this technique cannot provide estimation of the absolute histomorphometry measures of trabecular bone since the obtainable images suffer from PV with a concomitant negative effect on the histomorphometry analysis. Therefore, further improvements of MRM currently rely on the development of higher level image processing techniques which will alleviate the negative effects of PV in the lower resolution regime. Provided that the common histomorphometry measures of trabecular bone have been accurately predetermined (i.e. in order to provide the basis for comparisons), complex image processing techniques will have to be developed and tested in the near future. However, the recent introduction of higher magnetic field strength whole body scanners in the clinical setting will condense such efforts alleviating, at the same time, any potential bias arising.

---

### ***7.3 SPENT in the investigation of trabecular bone***

This technique has never been used before with respect to bone imaging and the signal produced by the SPENT images was thought to relate to the structure of an object (i.e. in this case trabecular bone) in some way. Therefore, it was decided that SPENT was to be investigated in this project as a new technique for the characterization of trabecular bone.

#### **7.3.1 SPENT in the investigation of BMD**

The NSPENT signal averaged over a volume of interest correlated highly with BMD both in the individual NSPENT directions and in all directions combined together. The highest correlation was observed for a combination of all the NSPENT directions (i.e. global NSPENT) at a resolution of 234 micron with  $R^2=0.9457$ . The global NSPENT signal is unlikely to be directly measuring BMD so further analysis is required to identify exactly what the global NSPENT signal corresponds to. However, the strong correlation identified here provides strong encouragement that similar observations will also be possible in in-vivo investigations since the resolutions tested in this project are feasible at clinical magnetic field strengths.

#### **7.3.2 SPENT in the investigation of fracture prevalence**

The global NSPENT signal averaged over a volume of interest correlated highly with YM with  $R^2=0.5957$ . However, the relationship is not as strong as in the case of NSPENT Vs BMD, which suggests that SPENT is more sensitive to changes in bone volume (BMD) rather than bone strength (YM). Nevertheless, by using the information extracted with SPENT in association with other imaging techniques, may improve the potential of SPENT in this respect.

#### **7.3.3 Future work**

The NSPENT signal gave a very high correlation to the BMD even when measured in a single direction. However, the NSPENT signal is unlikely to be directly measuring BMD so further analysis is required to identify what exactly has been measured. Further simulations using different structures in the object should provide the answers to this question. Of particular interest would be to use the same amount of structure and

---

changing how well ordered it is. This should simulate an object with the same density but different architecture. In addition, simulating a structure that is a closer correlate to bone should help to bring a greater understanding of what exactly the NSPENT signal corresponds to. In addition, further understanding of the NSPENT signal may allow for more effective time saving strategies to be employed. However, until data from such investigations are forthcoming, SPENT imaging in the characterization of trabecular bone must be considered investigational.

Three and a half years of intensive research have revealed very positive findings which have been presented in this thesis. It can therefore be suggested that the continuation of this work is vital and should be carried out based on the experience gained from these investigations. It is believed that further evaluation of all the techniques presented in this thesis may prove MRI to be an invaluable and safe tool in the early characterisation of osteoporosis which may even change the current practice in the near future.

## References

**Allday, A. W, (2004)** “*Detection Capabilities of Energy Dispersive X-Ray Diffraction with Respect to In-Vitro Trabecular Bone Mineral Loss*”, PhD Thesis, City University, London, UK.

**An, Y. H & Draughn, R. A, (2000)** “Mechanical Testing of Bone and the Bone-Implant Interface”, first edition, CRC press LLC, USA.

**Antich, P. P, Anderson, J. A, Ashman, R. B, Dowdey, J. E, Gonzales, J, Murry, R. C, Zerwekh, J. E & Pak, C. Y, (1991)** “*Measurement of mechanical properties of bone material in vitro by ultrasound reflection: Methodology and comparison with ultrasound transmission*”, Journal of Bone Mineral Research, Vol. 6, p. 417-426.

**Antoniades, T, Scarpelli, J. P, Ruaud, J. P, Gonord, P & Guillot, G, (1999)** “*Bone labelling on micro-magnetic resonance images*”, Medical Image Analysis, Vol. 3, p. 119-128.

**Beral, V, (2003)** “*Breast cancer and hormone-replacement therapy in the Million Women Study*”, The Lancet, Vol. 362, p. 419-27.

**Bloch, F, Hansen, W. W & Packard, M, (1946)** “*Nuclear induction*”, Physical Review, Vol. 69, p. 127.

---

**Borah, B, Dufresne, T. E, Cockman, M. D, Gross, G. J, Sod, E. W, Myers, W. R, Combs, K. S, Higgins, R. E, Pierce, S. A & Stevens, M. L, (2000)** “*Evaluation of changes in trabecular bone architecture and mechanical properties of minipig vertebrae by three-dimensional magnetic resonance microimaging and finite element modeling*”, Journal of Bone and Mineral Research, Vol. 15, p. 1786-1797.

**Brismar, T. B, (2000)** “*MR relaxometry of lumbar spine, hip, and calcaneus in healthy premenopausal women: relationship with dual energy X-ray absorptiometry and quantitative ultrasound*”, European Radiology, Vol. 10, p. 1215-1221.

**Brismar, T. B, Karlsson, M, Li, T. Q & Ringertz, H, (1999)** “*Orientation of trabecular bone in human vertebrae assessed by MRI*”, European Radiology, Vol. 9, p. 643-647.

**Bronskill, J. M & Sprawls, P, (1993)** “THE PHYSICS OF MRI:1992 AAPM Summer Scholl Proceedings”, Medical Physics Monograph No. 21, American Institute of Physics, Inc, USA.

**Brown, M. A, & Semelka, R. C, (1999)** “MRI basic principles and applications”, second edition, Wiley-Liss, United States of America.

**Cady, E. B, (1990)** “Clinical Magnetic Resonance Spectroscopy”, Plenum Press, New York.

---

**Carmichael, D, W, (2003)** "*Speed and Contrast in Magnetic Resonance Imaging*", PhD Thesis, University College London, Department of Medical Physics and Bioengineering, London, UK.

**Carmichael, D. W, Ordidge, R. J & Yiannakas, M. C, (2002)** "*SPENT (Sub-Pixel Enhancement of Non-uniform Tissue): A new Pulse Sequence and its Application to Bone Imaging*", abstract, ISMRM.

**Carmichael, D, Yiannakas, M, Farquharson, M & Ordidge, R. J, (2003)** "*Predicting bone strength with SPENT (Sub Pixel Enhancement of Non-Uniform Tissue) and R2*", Abstract, ISMRM.

**Chung, H, Wehrli, F. W, William, J. L & Kugelmass, S. D, (1993)** "*Relationship between NMR transverse relaxation, trabecular bone architecture, and strength*", Proceedings of the National Academy of Sciences of the United States of America, Vol. 90, p. 10250-10254.

**Chung, H, Wehrli, F, William, J, Kugelmass, S & Wehrli, S, (1995)** "*Quantitative analysis of trabecular microstructure by 400MHz nuclear magnetic resonance imaging*", Journal of Bone and Mineral Research, Vol. 10, p. 803-811.

**Cohn, S. H, Abesamis, C, Yasamura, S, Aloia, J. F, Zanzi, I & Ellis, K. J, (1977)** "*Comparative skeletal mass and radial bone mineral content in black and white women*", Metabolism, Vol. 26, p. 171-8.

---

**Cummings, S. R & Melton, L. J, (2002)** “*Epidemiology and outcomes of osteoporotic fractures*”, Lancet, Vol. 359, no. 9319, p. 1761-7.

**Davis, C. A, Genant, H. K & Dunham, J. S, (1986)** “*The effects of bone on proton NMR relaxation times of surrounding liquids*”, Investigative Radiology, Vol. 21, p. 472.

**Deichmann, R, Adolf, E, Noth, U, Schwarzbauer, C & Haase, A, (1995)** “*Compensation of diffusion effects in T2 measurements*”, Magnetic Resonance in Medicine, Vol. 33, p. 113-115.

**Engelke, K, Majumdar, S & Genant, H. K, (1994)** “*Impact of trabecular structure on marrow relaxation time, T2\*: phantom studies*”, Magnetic Resonance in Medicine, Vol. 31, p. 380-387.

**Fernandez-Seara, M. A, Song, H. K & Wehrli, F. W, (2001)** “*Trabecular Bone volume Fraction Mapping by Low-resolution MRI*”, Magnetic Resonance in Medicine, Vol. 46, p. 103-113.

**Fleisch, H. A, (1997)** “*Bisphosphonates: preclinical aspects and use in osteoporosis*”, Ann Med, Vol. 29, p. 55-62.

**Foster, M. A & Hutchison, J. M. S, (1987)** “Practical NMR imaging”, IRL Press, Oxford, U.K.

---

**Frahm, J, Haase, A & Matthaei, D, (1986)** “*Rapid three-dimensional MR imaging using the FLASH technique*”, *Journal of Computer Assisted Tomography*, vol. 10, no. 2, p. 363-368.

**Francis, R. M, (1990)** “*Osteoporosis: pathogenesis & management*”, first edition, Kluwer Academic Publishers, UK.

**Francis, R. M, (2001)** “*Falls and fractures*”, *Age and Ageing*, Vol. 30-S4, p. 25-28.

**Francis, R. M, Peacock, M, Aaron, J. E, Selby, P. L, Taylor, G. A, Thompson, J, Marshall, D. H & Horsman, A, (1987)** “*Osteoporosis in hypogonadal men: role of decreased plasma 1,25-dihydroxyvitamin D, calcium malabsorption, and low bone formation*”, *Bone*, Vol. 7, p. 261-8.

**Gadian, D. G, (1995)** “*NMR and its applications to living systems*”, 2nd edition, Oxford University Press, Oxford, U.K.

**Genant, H. K, Engelke, K, Fuerst, T, Gluer, C. C, Grampp, S, Harris, S. T, Jergas, M, Lang, T, Lu, Y, Majumdar, S, Mathur, A & Takada, M, (1996)** “*Noninvasive assessment of bone mineral and structure: state of the art*”, *Journal of Bone and Mineral Research*, Vol. 11, p. 707-730.

**Genant, H. K & Majumdar, S, (1997)** “*High-resolution magnetic resonance imaging of trabecular bone structure*”, *Osteoporosis International*, Vol. 7 suppl. 3, p. S135-9.

---

**Genant, H. K & Boyd, D. P, (1977)** “*Quantitative bone mineral analysis using dual-energy computed tomography*”, Investigative Radiology, Vol. 12, p. 545-551.

**Gluer, C. C, Vahlensieck, M, Faulkner, K, G, Engelke, K, Black, D & Genant, H. K, (1992)** “*Site-matched calcaneal measurements of broadband ultrasound attenuation and single x-ray absorptiometry: Do they measure different skeletal properties?*”, Journal of Bone and Mineral Research, Vol. 7, p. 1071-1077.

**Gluer, C. C, Wu, C. Y, Jergas, M, Goldstein, S. A & Genant, H. K, (1994)** “*Three quantitative ultrasound parameters reflect bone structure*”, Calcified Tissue International, Vol. 55, p. 46-52.

**Goodsitt, M. M, Rosenthal, D. I, Reinus, W. R & Coumas, J, (1987)** “*Two postprocessing CT techniques for determining the composition of trabecular bone*”, Investigative Radiology, Vol. 22, p. 209-215.

**Grampp, S, Henk, C. B & Imhof, H, (1999)** “*CT and MR Assessment of Osteoporosis*”, Seminars in Ultrasound, CT, and MRI, Vol. 20, No. 1, p. 2-9.

**Guglielmi, G, Gluer, C. C, Majumdar, S, Blunt, B. A & Genant, H. K, (1995)** “*Current methods and advances in bone densitometry*”, European Journal of Radiology, Vol. 5, p. 129-139.

---

**Haacke, E. M, Brown, R. W, Thompson, M. R & Venkatesan, R, (1999),** “Magnetic Resonance Imaging Physical Principles and Sequence design”, 1st edition, John Wiley and Sons, New York, USA.

**Harris, S. T, Watts, N. B, Genant, H. K et al, (1999)** “*Effects of risendronate treatment on vertebral and non-vertebral fractures in women with postmenopausal osteoporosis: a randomized, controlled trial*”, JAMA, Vol. 282, p. 1344-1352.

**Hashemi, R. H & Bradley, W. G, (1997)** “MRI: the basics”, Williams & Wilkins, United States of America.

**Heaney, R. P, Zizic, T. M, Fogelman, I et al, (2002)** “*Risendronate reduces the risk of first vertebral fracture in osteoporotic women*”, Osteoporosis International, Vol. 13, p. 501-505.

**Hipp, J, Jansujwicz, A, Simmons, C & Snyder, B, (1996)** “*Trabecular bone morphology from micro-magnetic resonance imaging*”, Journal of Bone and Mineral Research, Vol. 11, p. 286-292.

**Homminga, J, McCreadie, B. R, Ciarelli, T. E, Weinans, H, Goldstein, S. A & Huiskes, R, (2002)** “*Cancellous bone mechanical properties from normals and patients with hip fractures differ on the structure level, not on the bone hard tissue level*”, Bone, Vol. 30, No. 5, p. 759-764.

**Horsman, A, Jones, M, Francis, R & Nordin, C, (1983)** “*The effect of oestrogen dose on postmenopausal bone loss*”, New England Journal of Medicine, Vol. 309, p. 1405-7.

---

**Hunt, K, Vessey, M, McPherson, K & Coleman, M, (1987)** “*Long-term surveillance of mortality and cancer incidence in women receiving hormone replacement therapy*”, British Journal of Obstetrics and Gynaecology, Vol. 94, p. 620-35.

**Hwang, S & Wehrli, F, (2002)** “Subvoxel Processing: A Method for Reducing Partial Volume Blurring With Application to In Vivo MR Images of Trabecular bone”, Magnetic Resonance in Medicine, Vol. 47, p. 948-957.

**Jara, H, Wehrli, F. W, Chung, H & Ford, J. C, (1993)** “*High resolution variable flip angle 3D MR imaging of trabecular microstructure in vivo*”, Magnetic Resonance in Medicine, Vol. 29, p. 528-539.

**Jiang, Y, Zhao, J, Augat, P, Ouyang, X, Lu, Y, Majumdar, S & Genant H. K, (1998)** “*Trabecular bone mineral and calculated structure of human bone specimens scanned by peripheral quantitative computed Tomography: relation to biomechanical properties*”, Journal of Bone Mineral Research, Vol. 13, p. 1783-1790.

**Kaisel, W & Ruegsegger, P, (1991)** “*3D-QCT at peripheral measuring sites*”, Osteoporosis International, Vol. 1, p. 193.

**Kang, C, Paley, M, Ordidge, R & Speller, R, (1999)** “*R<sup>2</sup> measured in trabecular bone in-vitro: relationship to trabecular separation*”, Magnetic Resonance Imaging, Vol. 17, No. 7, p. 989-95.

---

**Kanis, J. A, Melton, L. J, Christiansen C, Johnston C. C and Khaltaev, N, (1994)** “*The diagnosis of osteoporosis*”, Journal of Bone and Mineral Research, Vol. 9, p. 1137-41.

**Kelly, T. L, Crane, G & Baran, D. T, (1994)** “*Single x-ray absorptiometry of the forearm: Precision, correlation, and reference data*”, Calcified Tissue International, Vol. 54, p. 212-218.

**Kleerekoper, M, Villanueva, A. R, Stanciu, J, Rao, D. S & Parfitt, A. M, (1985)** “*The role of three-dimensional trabecular microstructure in the pathogenesis of vertebral compression fractures*”, Calcified Tissue International, Vol. 37, p. 594-597.

**Lauterbur, P, (1973)** “*Image formation by induced local interactions: examples employing nuclear magnetic resonance*”, Nature, Vol. 242, p. 190-191.

**Link, T. M, Majumdar, S, Augat, P, Lin, J. C, Newitt, D, Lane, N. E & Genant, H. K, (1998a)** “*Proximal femur: Assessment for osteoporosis with T2\* decay characteristics at MR imaging*”, Radiology, Vol. 209, p. 531-536.

**Link, T. M, Majumdar, S, Augat, P, Lin, J, Newitt, D, Lu, Y, Lane, N & Genant, H, (1998b)** “*In vivo high resolution MRI of the calcaneus: differences in the trabecular structure in osteoporosis patients*”, Journal of Bone and Mineral Research, Vol. 13, p. 1175-1182.

---

**Majumdar, S, (1991)** “*Magnetic field inhomogeneity effects induced by inherent tissue susceptibility differences in gradient-echo magnetic resonance imaging: computer simulations*”, Magnetic Resonance in Medicine, Vol. 22, p. 101-110.

**Majumdar, S, (1998)** “*A review of magnetic resonance (MR) imaging of trabecular bone micro-architecture: contribution to the prediction of biomechanical properties and fracture prevalence*”, Technology in Health Care, Vol. 6, p. 321-7.

**Majumdar, S & Genant, H. K, (1995a)** “*A Review of the Recent Advances in Magnetic Resonance Imaging in the Assessment of Osteoporosis*”, Osteoporosis International, Vol. 5, p. 79-92.

**Majumdar, S & Genant, H. K, (1995b)** “*Magnetic resonance imaging in osteoporosis*”, European Journal of Radiology, Vol. 20, p. 193-197.

**Majumdar, S, Kothari, M, Augat, P, Newitt, D, Link, T, Lin, J, (1998)** “*High resolution magnetic resonance (MR): three-dimensional (3D) trabecular bone architecture and biomechanical properties*”, Bone, Vol. 22, p. 445-54.

**Majumdar, S, Link, T. M, Augat, P, Lin, J. C, Newitt, D, Lane, N. E & Genant, H. K, (1999)** “*Trabecular Bone Architecture in the Distal Radius Using Magnetic Resonance Imaging in Subjects with Fractures of the proximal Femur*”, Osteoporosis International, Vol. 10, p. 231-239.

---

**Majumdar, S, Thomasson, D, Shimakawa, A & Genant, H. K, (1991)** "*Quantitation of the Susceptibility Difference between Trabecular Bone and Bone Marrow: Experimental Studies*", Magnetic Resonance in Medicine, Vol. 22, p. 111-127.

**Mansfield, P & Maudsley, A. A, (1976)** "*Planar and line-scan spin imaging by NMR*", Proc.19th AMPERE congress, Heidelberg, p. 247-252.

**Mazess, R, Chesnut, C. H, McClung, M & Genant, H. K, (1992)** "*Enhanced precision with dual-energy x-ray absorptiometry*". Calcified Tissue International, Vol. 51, p. 14-17.

**McClung, M, Clemmesen, B, Daifotis, A, Gilchrist, N. L, Eisman, J, Weinstein, R. S, Fuleihan, G. el-H, Reda, C, Yates, A. J and Ravn, P, (1998)** "*Alendronate prevents postmenopausal bone loss in women without osteoporosis. A double-blind, randomized, controlled trial. Alendronate osteoporosis prevention study group*", Ann Internal Med, Vol. 128, p. 253-61.

**McRobbie, D. W, Moore, E. L, Graves, M. J & Prince, M. R, (2003)** "MRI: from picture to proton", Cambridge University Press, United kingdom.

**Morgan, D. B, Spiers, F. W, Pulvertaft, C. N & Fourman, P, (1967)** "*The amount of bone in the metacarpal and phalanx according to age and sex*", Clinical Radiology, Vol. 18, p. 101-108.

---

**Neer, R. M, Arnaud, C. D, Zanchetta J. R et al, (2001)** “*Effect of parathyroid hormone (1-34) on fractures and bone mineral density in postmenopausal women with osteoporosis*”, New Engl J Med, Vol. 344, p. 1434-1441.

**Nelson, D, Feingold, M, Mascha, E, Kleerekoper, M, (1992)** “*Comparison of single-photon and dual-energy x-ray absorptiometry of the radius*”, Bone Mineral, Vol. 18, p. 77-83.

**Nuti, R, Martini, G, Righi, G, Frediani, B & Turchetti, V, (1991)** “*Comparison of total body measurements by dual-energy x-ray absorptiometry and dual-photon absorptiometry*”, Journal of Bone Mineral Research, Vol. 6, 681-687.

**Och, J. G, Clarke, G. D, Sobol, T. W, Rosen, W. C & Mun, K. S, (1992)** “*Acceptance testing of magnetic resonance imaging systems: Report of AAPM Nuclear Magnetic Resonance Task Group No. 6a*”, Medical Physics, Vol. 19, No. 1, 217-228.

**Pacifici, R and Avioli, L. V. (1993)** “*Effects of ageing on bone structure and metabolism*”. In: The osteoporotic syndrome, 3<sup>rd</sup> edition, ed. L. V. Avioli. (New York: Wiley-Liss).

**Piney, A, (1922)** “*The anatomy of the bone marrow: with special reference to the distribution of the red marrow*”, BMJ, Vol. 28, p. 792-795.

---

**Prudham, D & Evans, J. G, (1981)** “*Factors associated with falls in the elderly: a community study*”. Age and Ageing, Vol. 10, p. 141-6.

**Purcell, E. M, Torrey, H. C & Pound, R. V, (1946)** “*Resonance absorption by nuclear magnetic moments in a solid*”, Physical Review, Vol. 69, p. 37.

**Remy, F & Guillot, G, (1998)** “*Trabecular bone characterisation with low-field MRI*”, Magnetic Resonance Imaging, Vol. 16, p. 639-642.

**Riis, B, Thomsen, K & Christiansen, C, (1987)** “*Does calcium supplementation prevent postmenopausal bone loss? A double blind controlled study*”, New England Journal of Medicine, Vol. 316, p. 173-7.

**Rinck, P. A, (2001)** “Magnetic Resonance in Medicine”. Blackwell, Germany.

**Rosenthal, H, Thulborn, K. R, Rosenthal, D. I & Rosen, B. R, (1990)** “*Magnetic susceptibility effects of trabecular bone on magnetic resonance bone marrow imaging*”, Investigative Radiology, Vol. 25, p. 173-178.

**Rupich, R. C, Pacifici, R, Griffin, M. G, Vered, I, Susman, N, Avioli, L. V, (1990)** “*Lateral dual energy radiography: a new method for measuring vertebral bone density. A preliminary study*”, Journal of Clinical Endocrinology and Metabolism, Vol. 70, p. 1768-1770.

---

**Schlenker, R. A & Von Seggen, W. W, (1976)** “*The distribution of cortical and trabecular bone mass along the lengths of the radius and ulna and the implications for in-vivo bone mass measurements*”, Calcified Tissue Research, Vol. 20, p. 41-52.

**Selby, K, Majumdar, S, Newitt, D. C & Genant, H. K, (1996)** “*Investigation of decay characteristics of MR relaxation time, T2\*, in microphantom models of trabecular bone*”, Journal of Magnetic Resonance Imaging, Vol. 6, p. 549-559.

**Shellock, F. G, Schaefer, D. J & Gordon, C. J, (1986)** “*Effect of a 1.5 T static magnetic field on body temperature of man*”, Magnetic Resonance In Medicine, Vol. 3, No. 4, p. 644-647.

**Song, H. K, Wehrli, F. W & Ma, J, (1997)** “*Field strength and angle dependence of trabecular bone marrow transverse relaxation in the calcaneus*”, Journal of Magnetic Resonance Imaging, Vol. 7, p. 382-388.

**Stark, D. D & Bradley, G. W, (1992)** “MAGNETIC RESONANCE IMAGING”, second edition, Volume 1, Mosby, USA.

**Swift, C, (2001)** “*Falls in later life and their consequences*”, BMJ, Vol. 322, p. 855-7.

**Thibodeau, G. A & Patton, K. T, (1993)** “Anatomy & Physiology”, second edition, Mosby, United States of America.

---

**Uebelhart, D, Duboef, F, Meunier, P. J & Delmas, P. D, (1990)** “*Lateral dual-photon absorptiometry: a new technique to measure bone mineral density at the lumbar spine*”, Journal of Bone Mineral Research, Vol. 5, p. 525-531.

**Vande Berg, B. C, Malghem, J, Lecouvet, F. E & Maldague, B, (1998)** “*Magnetic resonance imaging of the normal bone marrow*”, Skeletal Radiology, Vol. 27, p. 471-483.

**Watts, N. B, (2001)** “*Treatment of osteoporosis with bisphosphonates*”, Dis Clin North, Vol. 27, p. 197-214.

**Wehrli, F. W, Ford, J. C & Haddad, J. G, (1995)** “*Osteoporosis: Clinical Assessment with Quantitative MR Imaging in Diagnosis*”, Radiology, Vol. 196, p. 631-641.

**Wehrli, F. W, Hopkins, J. A, Hwang, S. N, Song, H. K, Snyder, P. J & Haddad, J. G, (2000)** “*Cross-sectional study of Osteopenia with quantitative MR imaging and bone densitometry*”, Radiology, Vol. 217, p. 527-538.

**Wehrli, F. W, Hwang, S. N & Song, H. K, (1998a)** “*New architectural parameters derived from micro-MRI for the prediction of trabecular bone strength*”, Technology in Health Care, Vol. 6, p. 307-320.

---

**Wehrli, F, Hwang, S, Ma, J, Song, H, Ford, H & Haddad, J, (1998b)** “*Cancellous bone volume and structure in the forearm: non-invasive assessment with MR microimaging and image processing*”, Radiology, Vol. 206, p. 347-357.

**Weinstein, R. S & Hutson, M. S, (1987)** “*Decreased trabecular width and increased trabecular spacing contribute to bone loss with ageing*”, Bone, Vol. 8, p. 137-142.

**Whitehouse, W. J & Dyson, ED (1974)** “*Scanning electron microscope studies of trabecular bone in the proximal end of the human femur*”, Journal of Anatomy, Vol. 118, p. 417-444.

**Whittall, K, Mackay, A & Li, D, (1999)** “*Are mono-exponential fits to a few echoes sufficient to determine T2 relaxation for in vivo human brain?*”, Magnetic Resonance in Medicine, p. 1255-7.

**Williams, P. L, (1989)** “Gray’s Anatomy”, 37<sup>th</sup> edition. Churchill Livingstone, UK.

**Yablonskiy, D. A, Reinus, W. R, Stark, H & Haacke, M, (1996)** “*Quantitation of T-2\* anisotropic effects on magnetic resonance bone mineral density measurement*” Magnetic Resonance in Medicine, Vol. 37, p. 214-221.

---

## **Bibliography**

**Butler, D. S & Lewis, R, (1996)** "HOLE'S HUMAN ANATOMY & PHYSIOLOGY". seventh edition. Wim, C, Brown Publishers, United States of America.

**Capuani, S, Curzi, F, Alessandri, F, Maraviglia, B & Bifone, A, (2001)** "*Characterization of Trabecular Bone by Dipolar Demagnetizing Field MRI*", Magnetic Resonance in Medicine, Vol. 46, p. 683-689.

**Cortet, B, Boutry, N, Dubois, P, Bourel, P, Cotton, A & Merchandise, X, (2000)** "*In Vivo Comparison Between Computed Tomography and Magnetic Resonance Image Analysis of the Distal Radius in the Assessment of Osteoporosis*", Journal of Clinical Densitometry, Vol. 3, No. 1, p. 15-26.

**Cortet, B, Colin, D, Dubois, P, Delcambre, B & Merchandise, X, (1995)** "*Methods for quantitative analysis of trabecular bone structure*", Revue du Rhumatisme, English Edition, Vol. 62, p. 781-93.

**Feldkamp, A. L, Goldstein, A. S, Parfitt, M, Jesion, J & Kleerekoper, M, (1989)** "*The Direct examination of Three-Dimensional Bone Architecture In Vivo by Computed Tomography*", Journal of Bone and Mineral Research, Vol. 4, p. 3-11.

---

**Genant, H. K, (2000)** *“Advanced CT and MR imaging of bone micro structure”*, Osteoporosis International, Suppl 1, Vol. 11, p. S16-S18.

**Genant, H. K, Gordon, C, Jiang, Y, Lang, T. F, Link, T. M & Majumdar, S, (1999)** *“Advanced imaging of bone macro and micro structure”*, Bone, Vol. 25, p. 149-152.

**Gomberg, B. R, Saha, P. K, Song, H. K, Hwang, S. N & Wehrli, F. W, (2000)** *“Topological analysis of trabecular bone MR images”*, IEEE Transactions on Medical Imaging, Vol. 19, p. 166-174.

**Gordon, C. L, Webber, C. E, Christoforou, N & Nahmias, C, (1997)** *“In vivo assessment of trabecular bone structure at the distal radius from high-resolution magnetic resonance images”*, Medical Physics, Vol. 24, p. 585-593.

**Grampp, S, Majumdar, S, Jergas, M, Newitt, D. C, Lang, P & Genant, H. K, (1996)** *“In vivo assessment of the distal radius by quantitative magnetic resonance imaging, peripheral quantitative computed tomography, and dual x-ray absorptiometry”*, Radiology, Vol. 198, p. 213-218.

**Guglielmi, G, Blunt, B. A, Jergas, M, Selby, K, Newitt, D. C, Genant, H. K & Majumdar, S, (1996)** *“Quantitative magnetic resonance of the calcaneus to assess regional variations in trabecular bone”*, Academic Radiology, Vol. 3, p. 336-343.

---

**Hilaire, L, Wehrli, F. W & Song, H. K, (2000)** “*High-speed spectroscopic imaging for cancellous bone marrow R-2\* mapping and lipid quantification*”, Magnetic Resonance Imaging, Vol. 18, p. 777-786.

**Hwang, S & Wehrli, F, (1999)** “*Estimating Voxel Volume Fractions of Trabecular Bone on the Basis of Magnetic Resonance Images acquired in Vivo*”, International Journal of Imaging systems in Technology, Vol. 10, p. 186-198.

**Hwang, S, Wehrli, F & Williams, J, (1997)** “*Probability-based structural parameters from three-dimensional nuclear magnetic resonance images as predictors of trabecular bone strength*”, Medical Physics, Vol. 24, p. 1255-1261.

**Jokisch, D. W, Patton, P. W, Inglis, B. A, Bouchet, L. G, Rajon, D. A, Rifkin, J & Bolch, W. E, (1998)** “*NMR microscopy and its role in skeletal dosimetry*”, Health physics, Vol. 75, p. 584-596.

**Kapadia, R. D, Stroup, G. B, Badger, A. M, Koller, B, Levin, J. M, Coatney, R. W, Dodds, R. A, Liang, X, Lark, M. W & Gowen, M, (1998)** “*Applications of micro-CT and MR microscopy to study pre-clinical models of osteoporosis and osteoarthritis*”, Technology in Health Care, Vol. 6, p. 361-372.

**Kothari, M, Chen, T, Lin, J, Newitt, D, Majumdar, S & Genant, H, (1997)** “*Three-dimensional bone structure determination: effect of image resolution*”, Osteoporosis International, Vol. 7, p. 289.

---

**Kuehn, B, Stampa, B, Heller, M & Glueer, C, (1997)** "*In vivo assessment of trabecular bone structure of the human phalanges using high resolution magnetic resonance imaging*", Osteoporosis International, Vol. 7, p. 291.

**Lin, J. C, Amling, M, Newitt, D. C, Selby, K, Srivastav, S. K, Delling, G, Genant, H & Majumdar, S, (1998)** "*Heterogeneity of trabecular bone structure in the calcaneus using high resolution magnetic resonance imaging (MRI)*", Osteoporosis International, Vol. 8, p. 16-24.

**Link, T. M, Majumdar, S, Grampp, S, Guglielmi, G, van Kuijk, C, Imhof, H, Glueer, C & Adams, J. E, (1999)** "*Imaging of trabecular bone structure in osteoporosis*", European Radiology, Vol. 9, p. 1781-1788.

**Link, T. M, Majumdar, S, Lin, J. C, Newitt, D, Augat, P, Ouang, X, Mathur, A & Genant, H. K, (1998)** "*A comparative study of trabecular bone properties in the spine and femur using high resolution MRI and CT*", Journal of Bone and Mineral Research, Vol. 13, Vol. p. 122-132.

**Machann, J, Schnatterbeck, P, Raible, A, Lutz, O, Claussen, C. D & Schick, F, (2000)** "*Magnetic resonance osteodensitometry in human heel bones: Correlation with quantitative computed tomography using different measuring parameters*", Investigative Radiology, Vol. 35, p. 393-400.

---

**Majumdar, S & Genant, H. K, (1997)** "*Assessment of trabecular structure using high resolution magnetic resonance imaging*", Stud Health Technol Inform, 1997, Vol. 40, p. 81-96.

**Majumdar, S, Genant, H. K, Gies, A & Guglielmi, G, (1993)** "*Regional variations in trabecular structure in the calcaneus assessed using high resolution magnetic resonance images and image analysis*", Journal of Bone and Mineral Research, Vol. 8S, p. 351.

**Majumdar, S, Genant, H. K, Grampp, S, Newitt, D. C, Truong, V. H, Lin, J. C & Mathur, A, (1997)** "*Correlation of trabecular bone structure with age, bone mineral density, and osteoporotic status: in vivo studies in the distal radius using high resolution magnetic resonance imaging*", Journal of Bone and Mineral Research, Vol. 12, p. 111-8.

**Majumdar, S, Newitt, D, Jergas, M, Gies, A, Chiu, E, Osman, D, Keltner, J, Keyak, J & Genant, H, (1995)** "*Evaluation of technical factors affecting the quantification of trabecular bone structure using magnetic resonance imaging*", Bone, Vol. 17, p. 417-430.

**Majumdar, S, Newitt, D, Kothari, M, Link, T, Augat, P, Lin, J, Lang, T & Genant, H, (1997)** "*Measuring 3D trabecular structure and anisotropy using magnetic resonance*", Osteoporosis International, Vol. 7, p. 272.

---

**Mihalopoulou, E, Allein, S, Luypaert, R, Eisendrath, H, & Panayiotakis, G, (1999)** “*Computer simulations for the optimisation of magnetic resonance phase imaging applied in the study of trabecular bone*”, Computer Methods and Programs Biomedicine, Vol. 60, p. 1-10.

**Ouyang, X, Selby, K, Lang, P, Majumdar, S & Genant, H, (1997)** “*High resolution imaging of the calcaneus: age-related changes in the trabecular structure and comparison with DXA measurements*”, Calcified Tissue International, Vol. 60, p. 139-147.

**Tritt-Goc, J, Pislewski, N, Kafak-Hachulska, A, Chmielewski, D, Gorecki, A & Kolodziejki, W, (1999)** “*Proton magnetic resonance microimaging of human trabecular bone*”, Solid State Nuclear Magnetic Resonance, Vol. 15, p. 91-8.

**Wessels, M, Mason, R. P, Antich, P. P, Zerwekh, J. E & Park, C. Y, (1997)** “*Connectivity in human cancellous bone by three-dimensional magnetic resonance imaging*”. Medical Physics, Vol. 24, p. 1409-20.